

# UC Berkeley

## UC Berkeley Electronic Theses and Dissertations

### Title

Digital Fluorescence Microscopy for Tuberculosis Diagnosis

### Permalink

<https://escholarship.org/uc/item/9xf8t4rz>

### Author

Switz, Neil Andrew

### Publication Date

2012

Peer reviewed|Thesis/dissertation

# Digital Fluorescence Microscopy for Tuberculosis Diagnosis

by

Neil Andrew Switz

A dissertation submitted in partial satisfaction of the  
requirements for the degree of  
Doctor of Philosophy

in

Biophysics

in the

Graduate Division

of the

University of California, Berkeley

Committee in charge:

Professor Daniel A. Fletcher, Co-chair  
Professor Richard J. Saykally, Co-chair  
Professor Richard H. Kramer  
Professor Dorian Liepmann

Fall 2012

# Digital Fluorescence Microscopy for Tuberculosis Diagnosis

Copyright 2012  
by  
Neil Andrew Switz

## Abstract

Digital Fluorescence Microscopy for Tuberculosis Diagnosis

by

Neil Andrew Switz

Doctor of Philosophy in Biophysics

University of California, Berkeley

Professor Daniel A. Fletcher, Co-chair

Professor Richard J. Saykally, Co-chair

This thesis describes the conceptualization, design, creation, and testing of a portable digital LED fluorescence microscope for use in diagnosing *M. tuberculosis* in low-resource settings. Over a century after its introduction, sputum microscopy remains an essential technique for *tuberculosis* diagnosis even in wealthy countries: sputum from a patient is smeared on a slide, stained for visibility, and examined for the presence of microscopic *tuberculosis* bacteria, requiring both a high resolution microscope and substantial technician skill in interpreting what is observed. Our device is  $\leq 3\text{kg}$  and  $18 \times 18 \times 8 \text{ cm}$ ; battery-powered, charging off 12V solar or auto power; and controlled via USB 2.0 by a low-cost laptop. It is capable of digital fluorescence imaging in direct sunlight of Auramine O-stained sputum smears over a  $0.64 \times 0.49 \text{ mm}$  field of view with a nominal resolution of  $0.76 \mu\text{m}$  resolution and image display at  $\gtrsim 2500\text{X}$  magnification. Diagnostic sensitivity is 63% and specificity 85% when used by individuals with  $\sim 10$  hours of training in reading sputum smears. Images are uploaded automatically via the local mobile phone network to district hospitals for quality assurance and record-keeping. We have also developed a diagnostic image-processing algorithm with accuracy equivalent to our human readers when applied to images taken with the device; in the future we will integrate diagnostic image processing at the time of imaging in order to reduce technician training requirements, increase repeatability, and potentially increase sensitivity and specificity. The system is currently deployed in Hanoi, Vietnam as part of an effort to extend *tuberculosis* diagnosis to peripheral levels of the healthcare system.

In Memory of Miguel Wooding, 1964 - 2011

A humanitarian in the truest sense,  
without whom I would not be doing physics  
and many more would not have homes.

# Contents

<b>Contents</b>	<b>ii</b>
<b>List of Figures</b>	<b>iv</b>
<b>List of Tables</b>	<b>vi</b>
<b>Acknowledgements</b>	<b>vi</b>
<b>Preface</b>	<b>ix</b>
<b>1 Tuberculosis</b>	<b>1</b>
1.1 Introduction . . . . .	1
1.2 Outline . . . . .	2
1.3 Meet the enemy . . . . .	2
1.4 Diagnosis . . . . .	5
<b>2 Mobile Phone Based Microscopy</b>	<b>12</b>
2.1 Introduction . . . . .	12
2.2 Mobile Phone Based Clinical Microscopy for Global Health Applications . .	13
<b>3 Design</b>	<b>24</b>
3.1 Basic Optical Considerations . . . . .	24
3.2 Camera . . . . .	28
3.3 Illumination Intensity . . . . .	33
3.4 Illumination Uniformity . . . . .	40
3.5 Optical Filters . . . . .	41
3.6 Collection Optics . . . . .	46
3.7 Acceptance testing . . . . .	59
3.8 Software . . . . .	63
3.9 Use model . . . . .	65
<b>4 Device Validation</b>	<b>71</b>
4.1 Introduction . . . . .	71

4.2	Mobile digital fluorescence microscopy for diagnosis of tuberculosis . . . . .	72
<b>5</b>	<b>Automated Bacillus Identification</b>	<b>82</b>
5.1	Introduction . . . . .	82
5.2	Automated Tuberculosis Diagnosis Using Fluorescence Images from a Mobile Microscope . . . . .	84
5.3	Automated Tuberculosis Diagnosis Using Fluorescence Images from a Mobile Microscope . . . . .	84
<b>6</b>	<b>Conclusions</b>	<b>93</b>
	<b>Bibliography</b>	<b>97</b>

# List of Figures

1.1	Liquid culture system. . . . .	6
1.2	Solid culture system. . . . .	6
1.3	GeneXpert system. . . . .	7
1.4	Slide preparation. . . . .	8
1.5	Ziehl-Neelsen stained AFB. . . . .	9
1.6	Auramine-stained AFB. . . . .	9
2.1	Mobile phone microscopy layout schematic, prototype, and sample images. . . . .	16
2.2	Mobile phone microscopy images of diseased blood smears. . . . .	18
2.3	Fluorescence mobile phone microscopy images of tuberculosis in sputum. . . . .	19
3.1	Inscribed and exscribed sensor geometries. . . . .	29
3.2	Optical Train. . . . .	37
3.3	Condenser efficiency. . . . .	39
3.4	Calculated illumination uniformity. . . . .	41
3.5	Optimizing filter transition point. . . . .	44
3.6	Filter spectra. . . . .	45
3.7	LED spectrum. . . . .	46
3.8	COTS objective with doublet lens. . . . .	50
3.9	RMS spot size improvement using field-flattening lens. . . . .	52
3.10	Final optical layout. . . . .	52
3.11	Final optical layout. . . . .	53
3.12	RMS spot size of 15 units, as-built. . . . .	54
3.13	RMS spot size vs. field radius for final design. . . . .	55
3.14	Theoretical and measured MTF curves. . . . .	56
3.15	ZEMAX modeled system MTF. . . . .	57
3.16	Strehl ratio vs. field radius for final design. . . . .	59
3.17	TB imaged with the system. . . . .	63
3.18	Software interface: brightfield imaging. . . . .	64
3.19	Software interface: fluorescence imaging. . . . .	66
3.20	Backpack portable diagnostic. . . . .	67
3.21	Slide reading. . . . .	68

3.22	Image upload to central hospital. . . . .	69
3.23	Auto-ID diagnostic algorithm. . . . .	70
4.1	CellScope for digital light and fluorescence microscopy. . . . .	75
5.1	SVM overview. . . . .	83
5.2	Two versions of CellScope, a novel mobile microscope. . . . .	86
5.3	Sample CellScope images. . . . .	86
5.4	Overview of algorithm. . . . .	87
5.5	Object-level test set AP across different classifiers. . . . .	90
5.6	Slide-Level Performance. . . . .	91
6.1	Deployed systems. . . . .	96

# List of Tables

3.1	Ballpark initial optical requirements. . . . .	28
3.2	CMOS and CCD camera performance data. . . . .	31
3.3	Objective parameters. . . . .	48
3.4	Custom collection optics. . . . .	49
3.5	COTS objective with doublet lens. . . . .	51
3.6	Theoretical and measured MTF. . . . .	58
3.7	MTF ratios compared with theory. . . . .	58
3.8	Final Specifications. . . . .	60
4.1	Diagnostic accuracy of conventional and CellScope-based LED FM. . . . .	77
4.2	Intra-reader comparison. . . . .	78
4.3	Inter-reader comparison. . . . .	79

## Acknowledgments

First, I want to thank my science teachers: my father, Donald M. Switz, my grade school teachers Terry Kwan, Townley Chisolm, and Jim Boyd; and in college and graduate school, Fred Tabbutt, Don Middendorf, Michael A. Wooding, and Doug Osheroff.

Second, I want to thank my advisors: Mac Beasley, who spent time making sure I learned more as an undergraduate in his lab than just how to run equipment; Watt W. Webb, a scientist in the finest tradition who left me with an enduring appreciation for statistical mechanics and the power of fluctuations as a probe of system dynamics; Rich Saykally, whose infectious enthusiasm for science, especially the detailed behavior of that most important biological material, water, is always a pleasure to share; and last but hardly least, Dan Fletcher, whose support through pedagogical and scientific endeavors, and life's vicissitudes, extended far beyond any reasonable expectation and whose lab has been an unmitigated pleasure to be part of.

I would not, however, have continued in science without the compatriots with whom I have shared the excitement of discovering how things work. I apologize in advance for any inadvertent omissions, but special mention goes to my compatriots in Matter & Motion 86/87; the immortal Andronikashvili group of Gajus Worthington, Sabrina Yeh, Robert Liu, and Steve Quake; the denizens of the Stanford physics library during 1989–1992, including the aforementioned and many others; my officemates from Clark Hall, Chris Xu, Jeff Guild, Becky Williams, and Luke Ghislain. I learned much from Tom Hagler, the first industrial physicist I knew, and from Peter Ast and Peter Jansen, who are both friends and quietly (and less quietly) models of the best in engineering practice. Gajus, Todd, Michelle, the inimitable Rev. Dr. Manger, Marc, Bill, Philip, Hou-Pu, Barry and many others at the 'Digm taught me important things about making both companies and products. The Femtolab crew at Berkeley, including Rob Onorato, Dale Otten, and Paul Peng, was a privilege to be part of. Sharon Rozovsky, Martin Forstner, and Edouard Servan-Schreiber have all provided important perspective and camaraderie at crucial junctures. Rich Kramer opened his lab to me when I first arrived, and his steady support and encouragement have been much appreciated. The Fletcher Lab has been replete with friends, but special mention must go to fellow Cellscope team members Lina Nilsson, Robi Maamari, Mike D'Ambrosio, Jeannette Chang, Asa Tapley, Wilbur Lam, and Clay Reber. Particular thanks go to Clay, who took my class, then joined the lab, and with understated competence helped sustain both the class and the project — and hence this thesis — in many ways. Alan Schier and members of The Pilot Group were a pleasure to work with, and Ben Tigner, Sabrina Yeh, and associates added immeasurably to the pleasure of trips to LA. Viviana Risca, Ailey Crow, Dave Richmond, Kevin Webster, and other members of the Biophysics Group (and Fletcher Lab) have helped make my time at Berkeley a pleasure, and Diane Sigman and Kate Chase did much to make the experience successful. I have enjoyed over many years sharing technical interests, pleasurable discussions, and 'problems of the day' with John McGuire, Dave Fernandes, Jerome Mertz, Paul Peng, Ben Tigner, and ... Miguel Wooding.

My parents uncomplainingly bought me batteries, wire, and books, and later paid for me to attend college despite ample evidence suggesting it would be money wasted. My partner Cynthia encouraged me to return to school, put up with the ensuing trials and tribulations, and remains interested in what I do, all of which goes beyond words.

# Preface

Tuberculosis is not as far away, or as far in the past, as one might think. While of course I knew this as I worked on this project, it is nonetheless hard to appreciate from the safe confines of the United States, and remained so for me until one day when I was returning to Berkeley with a new prototype.

I was running late, and my heart sank as I approached airport security since the prototype I was carrying, packed in hastily-applied bubble wrap in an unsealed cardboard box, would not look very legitimate and was sure to set off concerns. In an attempt to forestall problems, I explained to the officers that the box would surely need to be checked further, and implored them to let me do the unpacking, since the prototype was delicate. It may have helped that I was near CalTech, where passengers with strange equipment are not so unusual, or perhaps it was just my good fortune that it was a slow night at a small airport; in any case, not only did the security personnel acquiesce, but they were actually interested, and started asking questions. Not questions designed to elicit whether the device was dangerous, but rather curious questions about what it was for, and how it worked. Prepared for dubious looks and an invasive search, I was caught unprepared — it had not occurred to me anyone would care what I was working on.

The instrument was, I explained, a battery-powered microscope for diagnosing tuberculosis (TB) in rural areas of developing countries, and we planned to test it in Uganda. This led to questions of what TB was, and how the machine detected it. As I politely began to disengage so that I could rush for my plane, a security agent stepped forward. He had been hanging back during the discussion, was probably in his sixties, and his nametag and accent suggested he was a first-generation immigrant. He had no question for me, but simply asked if he could shake my hand. It was unusual — none of the other guards had asked to shake my hand, and in my line of work, people rarely do. Of course, I did so, and ran to catch my flight.

I did not have time to ask, and in any case would not have presumed to do so, but the interaction made it clear that the guard was almost certainly familiar with TB. Unlike the other TSA screeners, all clearly US-born, he had probably not needed to ask what it was, or why it mattered. It was a sobering reminder that the project was not simply academic.

# Chapter 1

## Tuberculosis

### 1.1 Introduction

Tuberculosis remains a major scourge in much of the world, and with increasing rates of drug-resistant disease, again threatens even developed countries. Even where treatment is potentially available, delays in getting (often highly infectious) patients diagnosed results in increased transmission and ultimately also larger maximum size of outbreaks when they occur. Reasons for the delay in diagnosis vary, but frequently center on lack of equipment and trained personnel to do the testing — often an ill person must get to a central medical facility, perhaps more than a day’s travel away, before they have any hope of receiving a test-based diagnosis.

The basic idea which has motivated this thesis work is that advances in technology might enable development of an affordable, portable, semi-automated device that would allow a relatively-untrained healthcare worker to perform tuberculosis diagnostic testing even in a rural areas or away from a central hospital, thus reducing the time to diagnosis and helping to lower the disease burden in the community. The World Health Organization advocates exactly this approach, and modeling has suggested that improved diagnostic tests of this sort could potentially help save hundreds of thousands of lives each year [63].

The test systems we have built have in fact demonstrated that this is possible, though naturally many steps remain between initial field testing and any large-scale deployment. Taking advantage of the low-cost image sensors now used in webcams and cellphones, as well as high-power light-emitting diodes developed for the lighting industry, and leveraging the data processing (and transmitting) capabilities of modern cell phones and inexpensive laptops, we have produced a portable, digital fluorescence microscope that can automatically recognize tuberculosis in the images it takes, and transmit that information to a central facility. An earlier version of this system is now being tested as part of a study in Hanoi to enable tuberculosis diagnosis at peripheral levels of the local healthcare system.

Tuberculosis affects so many people, in so many countries, at so many socioeconomic levels, that standards of care by necessity evolve slowly. Tuberculosis is also, for the time

being, primarily a disease of the poor, with the result that (absent subsidies by charitable organizations) few companies are likely to invest resources in developing and distributing novel products to help treat and prevent it. Beyond having demonstrated what is now possible, my hope, and that of my collaborators, is that individual parts of the work may also be useful to others — research groups or companies — who are working on different aspects of the problem. For example, our choice of optical design has decided advantages for digital fluorescence systems, and our diagnostic image-processing algorithm, which has performance better than any other currently published, could improve current efforts to implement automated slide-reading in central hospitals.

I also hope that this work will be of use to others who are pushing to both create and (much harder) make available in large quantity a portable, low-cost diagnostic system that allows basic tuberculosis care to be extended to the many for whom it is currently hard or impossible to obtain.

## 1.2 Outline

This chapter, Chapter 1, covers tuberculosis, elements of its diagnosis, and particularly sputum microscopy as a main-line tuberculosis diagnostic. Chapter 2 describes our initial proof-of-concept demonstration that a camera-phone based, fluorescence microscope is capable of imaging tuberculosis bacilli in a standard sputum smear using a light-emitting diode for illumination. Technical requirements, optical design, and implementation of a portable digital fluorescence microscope for tuberculosis diagnosis are covered in Chapter 3, and Chapter 4 addresses our validation of the diagnostic efficacy of the device. The images from this validation work allowed us to develop an algorithm for automatic identification of tuberculosis bacilli in the images from the device, with performance rivaling that of the human users; this work is the topic of Chapter 5. Conclusions and suggestions for potentially fruitful subsequent work follow in Chapter 6.

## 1.3 Meet the enemy

In the United States, especially since 1960, it is easy to be unaware of infectious disease. Of course, we get colds, or the flu. Some of us even get pneumonia, which is viewed as quaint: who gets that anymore? A few days of antibiotics, which usually cost less than a take-out dinner, and we're fine again. Few of us know anyone young who's been seriously ill from an infectious disease, let alone anyone who's died of one.

As a result of this great fortune of birth location and timing, it is hard to even imagine the world of our grandparents, when polio still stalked the schools, people really did catch their death of pneumonia, and failing to put iodine on a scraped knee could end in fatal sepsis. In fact, that world does not even date to our grandparents: the parents of one friend met in the late 1950s while waiting to die in a TB sanatorium, and the father of another

is probably alive today because large-scale manufacturing of isoniazid, still a main-line TB antibiotic, had begun just in time for him to be treated with it. Of the few of us working on this project, one's grandfather had died of TB and another discovered that not one, but *both* parents had been diagnosed with it... though it seemed so uninteresting that they had never mentioned it to their children.

If you, like me, were born after 1960 and grew up in the developed world, you are unlikely to have any idea what tuberculosis is like, despite the fact that it has been a scourge since our prehistory. Chillingly, the terms for it in English, French, Latin, Hebrew, Urdu, among other languages, all mean the same thing: to be eaten alive — consumed — by the disease.

In his book *The Forgotten Plague*, a particularly readable overview of the medical and social history of tuberculosis, Dr. Frank Ryan describes eloquently how the disease progresses:

Where tuberculosis is common, most of the population will encounter germs when they are children... [and] the majority wall it off when it is still just a spot in the lungs and they never know they were infected. But if the body fails to contain it, which is the case in about ten per cent of people, then the disease continues to invade the lung tissue about it.

...

What happens is basically simple if dreadful: The bacteria inhaled in water droplets settle in the periphery of the lung and grow very slowly until they form a small local collection, like a cheesy boil. From this boil, the continuing infection spills over into nearby small airways and forms more of these tiny boils. It was the appearance of these small cheesy collections (like little tubers) which, in the early nineteenth century, gave rise to the modern name, the disease in which you find tubercles in the lung, or tuberculosis... From this first or primary infection in the lungs, several things may happen. In many, the first infection is fought off by the body. The white cells mop up the bacteria and the abscess is walled off from the rest of the lung by a fibrous shell. But our white cells have difficulty disposing of these ingested bacteria. That waxy shell can be as impervious to the digesting chemicals of our white cells as it is to acid, and tuberculosis has the horrifying ability to eat our white cells themselves from the inside and to grow and multiply while actually within the cells. In order to contain the disease, our body decides to accept stalemate and just wall it off. If we succeed, we lull ourselves into a false sense of security: we tell ourselves that we are cured. But tuberculosis remains alive within that fibrous shell and can burst out into life-threatening virulence at any time in the infected person's subsequent life.

...

If the infected person is undernourished, if their immunity is depressed (as in the modern example of AIDS), then the disease erupts with an explosive virulence. For the less lucky amongst us, the disease cannot be controlled by the body's defenses. They discover a cough which refuses to go away; perhaps there is a sudden agonizing pain on breathing that marks the beginning of pleurisy; sooner

or later will come the gathering exhaustion, the unrelievable breathlessness, the appearance of bright red arterial blood in the persistent foul sputum. In others, death arrives in one fell moment, for example when an abscess in the lung or intestine erodes into a major artery. When this happens the bleeding may be so torrential that the victim dies from exsanguination or from drowning in his own blood.

...

Over the long years in which tuberculosis causes the typical slow decline in health, evoked by its ancient name [consumption], the disease has a tendency to spread from the lungs or bowel and cause great pain and suffering elsewhere in the body. In the skin and soft tissues it causes disfiguring sores and abscesses; in the internal organs such as the bladder and kidneys it causes an agonizing inflammation. The pain associated with bladder tuberculosis was so severe that earlier in this century surgeons would transplant the ureters into the skin to bypass the bladder in a desperate attempt both to relieve the suffering and delay the development of the kidney failure that would eventually kill the patient. In bones it settles into a protracted and gnawing destructive cavitation, called osteomyelitis, its pus eventually finding its way through the surrounding soft tissues until it erupts onto the skin, where it continues to discharge until the sufferer eventually dies from it [100].

In the 1800's, roughly a *quarter* of all deaths in Europe were due to TB [28], and it is not an underestimate that over 1 billion lives have been lost to TB in just the past two centuries [100]. As late as 1949, nearly 1% of the U.S. non-white population died of it every year [28].

Given this, it is not surprising that when the British Nationalized Health Service first extended health care to all, in 1948, its first priority was tuberculosis. It was not until the early 1960s that it was believed, even in the relatively well-off U.S. and Britain, that TB could be eliminated in the national population, rather than simply controlled [100].

In fact, it has only been since then, with the advent of mass-produced antibiotics, that infectious disease has ceased to be an object of common awareness in this country. That is a situation unlikely to last, for TB due to the emergence of extensively-drug-resistant strains [100, 80, 98, 120, 86], and for infectious disease more generally because of the misuse of the precious resources that are antibiotics [40, 130, 61, 85]. From the standpoint of infectious disease, the last 50 years has been a medical golden age in the United States.

But not elsewhere. The developed world is familiar with AIDs and HIV, but malaria, TB, cholera, and a slew of other even more historical-sounding diseases kill millions of people a year in the developing world, often simply because they cannot afford the often  $\leq$  \$2.40 medications [67] that would cure them. Frequently even diagnosis is too expensive: it is hardly uncommon in endemic areas for diseases to be (often mis-) diagnosed based on symptoms alone due to lack of diagnostic testing infrastructure [90].

Tuberculosis has co-evolved with humans since ancient times. It is unlikely to go away anytime soon, since fully one third of the global population carries it [99], and some 10% of those carrying it will develop active disease, and be able to infect others, at some point during their life. TB is also extremely hard to treat: once diagnosed, an ill person must take antibiotics for 6–9 months [20], antibiotics which are expensive for many, and which in rare cases can be toxic and unpleasant [128]; furthermore, it is often extremely contagious [125]. Naturally, people tend to stop taking the drugs as soon as they feel better, leading to the evolution of drug-resistant TB strains that are hard or impossible to treat. This — along with the expense and limited number of “second-line” drugs for TB strains resistant to the standard antibiotics — is one of the largest issues in providing TB care. To overcome it standard treatment involves “directly observed therapy”, or DOT, where a healthcare worker monitors the patient to make sure they take their medications for the required time period [129]. Despite these difficulties, the standard 4-drug, 6-month treatment regimen has very high cure rates, and for the patient this treatment is often available free-of-charge through national TB programs

## 1.4 Diagnosis

There are several main ways to diagnose a person for TB. In the developed world even asymptomatic patients are often treated for latent infection if they show a positive tine- (or Mantoux) test for TB-antigen. However, in much of the world there are simply not resources to treat everyone who has latent TB, and only those who have progressed to active disease are treated. Because symptoms of TB are non-specific and can mimic other illnesses, and because treatment of TB consumes precious public health resources, establishing a definitive diagnosis before treatment is ideal. Unfortunately that is often quite difficult to do in resource-limited settings due to lack of even the simplest diagnostic tools [90].

### Chest x-ray and sputum analysis

The standard clinical diagnostics for tuberculosis are the chest x-ray (CXR) and sputum analysis, both dating to the late 1800s. X-rays require a sophisticated machine, exposing the patient to ionizing radiation, and skilled interpretation of the resulting image; as a result this method is generally restricted to centralized clinics and hospitals. Sputum-based techniques have the advantage of being simpler: they consist of taking a sample of sputum coughed up by a symptomatic patient and either using a microscope to look for tuberculosis bacilli in it, or culturing the same sputum in liquid broth or on a gelatin-like medium to see if tuberculosis grows (c.f. Figures 1.1 and 1.2). Culture is considered the “gold-standard” for diagnosis [38, 25], but takes 2–6 weeks to get results and, since it requires extensive biosafety infrastructure, is often available only at the one (or few) national reference laboratories. Consequently it is rarely used for TB diagnosis. Microscopy has the advantage of being both fast and cheap — if personnel and equipment are available, it can be done in under an hour.



Figure 1.1: **Becton-Dickinson liquid-culture system in use in Hanoi.** System requires steady wall power and proprietary reagents; tubes in rack have liquid-culture media where tuberculosis can grow, if present. Approximate time-to-diagnosis is 14 days [3]; cost is  $\sim$ \\$7.



Figure 1.2: **Solid culture being used in Hanoi.** Tubes in rack have culture media where tuberculosis can grow, if present. Time-to-diagnosis is 28+ days [113]; cost is  $\sim$ \\$5. White material inside the third test-tube from the left is tuberculosis.

## DNA-based diagnostics

Recently DNA-based sputum tests have also become available for use in developing countries [29]. Systems to automate polymerase-chain-reaction (PCR)-based tests are especially useful in that they can provide, with the press of a button, not only diagnosis but information on whether the tuberculosis strain is antibiotic-resistant. Unfortunately, these systems are expensive (e.g. Cepheid’s GeneXpert, Figure 1.3, is  $\sim$ USD\\$17,500 [32]) and require disposable cartridges which must be both available in the country and affordable (cost in Hanoi is  $\sim$ USD\\$20; currently negotiated prices through FIND are  $\sim$ USD\\$17 [15]). Such systems also require a reliable power source, often unavailable, nor are they truly portable. As a result of all this, it is considered “unlikely, in the short term, that Xpert can be scaled up and decentralized sufficiently to replace smear microscopy as the initial diagnostic test worldwide, even in areas with high rates of multi-drug-resistant TB or HIV-associated TB, where Xpert is recommended as the initial screening test.” [23] Furthermore, other than the speed of the assay, nucleic-acid amplification tests have not been found to offer substantial benefits over culture, especially in the case of sputum-smear-negative samples [54], although as the required equipment and reagents become more affordable, and if the power requirements are lowered, such systems will offer the opportunity for more widely decentralized testing than is possible with culture.

A word is merited on the subject of required reagents and disposables for novel diagnostics: it has been periodically suggested to me that since Coca-Cola (for instance) is widely available, then mere commercialization will result in essentially any good becoming widely distributed and cheap. This is rarely the case for diagnostics, which are simply not used in



Figure 1.3: **GeneXpert system in use in Hanoi.** System requires a dedicated computer and steady wall power; cartridges cost  $\sim$  \$20 per patient.

remotely the volumes that such commercial products are, resulting in smaller economies of scale in manufacturing and worse ones in distribution. Delivery of disposables and nonstandard reagents can be, as we have found in Hanoi, a significant hurdle even in a major city, let alone in the countryside. Furthermore, many emerging technologies, e.g. microfluidics, while extraordinarily powerful, require sophisticated readers, significant prior sample preparation, and/or disposable chips which are expensive to produce even if the raw materials may be cheap. Despite substantial early enthusiasm for the use of microfluidics in developing-world diagnostics [132] they have had poor outcomes and been essentially abandoned for the time being [60].

Because I have prior experience in industry, and in developing new technology for the commercial market, we took a very cautious approach to introducing new elements. Early inquiries with physicians who had experience in the developing world only served to reinforce our understanding that any diagnostic that was actually going to get used in low-resource locations would have to build on already-obtainable reagents and disposables.

For this reason, we focused early on use of sputum microscopy, which requires only (potentially reusable) glass slides and inexpensive bulk-chemical reagents which require no refrigeration and (in the case of the dyes for the brightfield stains) have been available in TB-endemic areas for many decades. Even the new, 2-minute fluorescent Auramine O stain (on which more later) we decided to use is both already available from distributors in

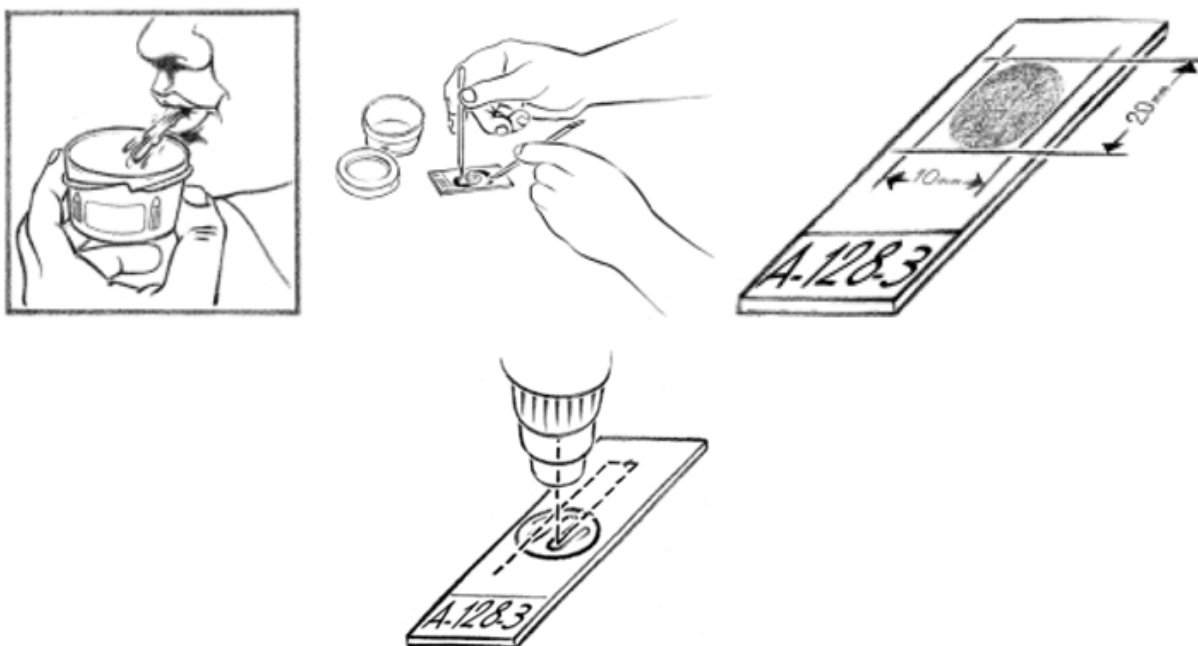


Figure 1.4: **Slide preparation.** Sputum is collected from patient, smeared on a slide, stained, and examined using a microscope [1].

many countries (e.g. Vietnam, where we are part of a study) and costs  $\lesssim$  \$0.04 per test when bought in bulk as part of QBC Corporation’s F.A.S.T. Auramine O Stain Kit (2012 pricing).

## Sputum microscopy

Sputum microscopy dates to the 1880’s, when Robert Koch first isolated tuberculosis in part by developing the first stain that allowed it to be visualized [69]. In slightly modified form it has been used for over a hundred years to diagnose tuberculosis. The basic procedure is straightforward: the patient coughs up some sputum, and a small bit of that ( $\leq 10 \mu\text{l}$ ) is smeared across a roughly 1 x 2 cm area on a glass slide. The slide is dried, soaked in a stain, and then rinsed to “destain” everything that is not tuberculosis. After rinsing, the slide is dried, and then examined under a microscope, as in Figure 1.4.

The destain is slightly acidic, and so objects which retain their color are termed “acid-fast”; hence bacilli that are seen on the slide are called “acid-fast bacilli”, or AFB. The primary staining procedure, named Ziehl-Neelsen after its developers, uses a carbolfuchsin stain, and the destain involves acid alcohol and methylene blue as a “counterstain”. The result is that the sputum smear, when viewed through a microscope, looks like Figure 1.5.

In 1962 researchers at the Ford Foundation found that one could stain the tuberculosis bacilli using a fluorescent stain [117], Auramine O. For comparison with the Ziehl-Neelsen

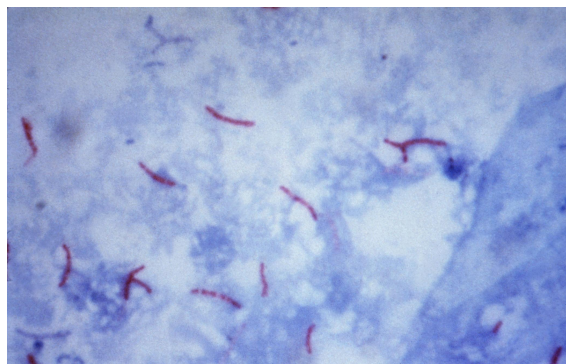


Figure 1.5: **Ziehl-Neelsen stained *Mycobacterium tuberculosis***. Original image magnified 1000X [70]. Red objects are tuberculosis bacilli.

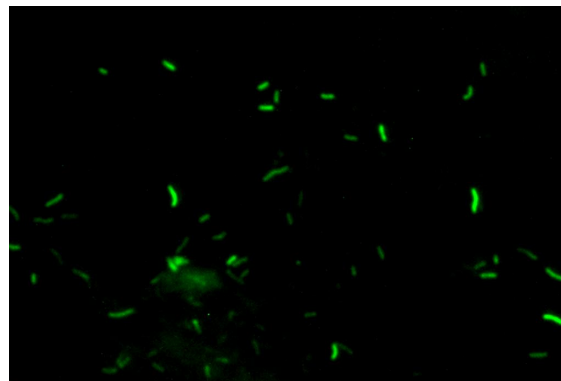


Figure 1.6: **Auramine-O-stained AFB**. Auramine-O stained *Mycobacterium tuberculosis*. Image taken at 0.4NA on our system; background subtracted and contrast stretched.

stain, Figure 1.6 shows how tuberculosis bacilli in a sputum smear look in fluorescence; it is readily apparent that the image is easier to quickly scan and interpret. Although it has long been known that this method of staining produces better diagnostic sensitivity (if somewhat lower specificity [23]) while decreasing the time required to read and grade the slides [68], until recently fluorescence microscopy was used relatively little outside the developed world. The reason for this is simple: in order to illuminate the slides brightly enough to see any bacilli fluoresce, expensive arc-lamps, whose \$100 bulbs need to be replaced every 200 hours of use, and which require ample and steady power, were required. To put this in perspective, in many countries \$100 is a significant fraction of an average person's annual income.

In low-resource countries, cost matters enormously. For instance, in Hanoi, where we are currently part of a World Health Organization study, culture is often used when drug-resistance is suspected (either because the patient is not responding to treatment or because they have other risk factors for resistance). However, solid culture is often used instead of liquid culture, even though liquid culture machines are available, due simply to the USD\$2 cost difference between the two (USD\$5 for solid vs. USD\$7 for liquid culture). This seemingly minor cost differential is sufficient to add a potential two-week delay in diagnosis time despite the fact that it is known that reducing time to diagnosis provides a dramatic — in some cases, exponential — decrease in the tuberculosis case burden in the community and the maximum size of disease outbreaks [122].

Sputum microscopy's low cost, modest equipment requirements (nonetheless often unmet [90]), and relative speed of diagnosis result in its continued nearly universal use in tuberculosis control. Despite this, access to diagnosis and treatment remain difficult for many:

Sputum smear microscopy services are the most decentralized of the TB diagnostic services, allowing patients to be screened for tuberculosis at relatively basic health care facilities. In most LMICs (low- and middle-income countries),

however, these centers are less numerous than treatment centers, and many patients still need to travel to submit sputum specimens for diagnosis, incurring considerable personal costs, and this often leads patients to abandon the process. The diagnosis of TB therefore is particularly difficult for poor and marginalized patients, who face multiple challenges to accessing a TB diagnosis, and the improvement of smear microscopy services remains necessary to increase patients' access to treatment [23].

## WHO standards for diagnosis

As a result of its low cost and speed of results, sputum microscopy is the mainstay of tuberculosis diagnosis worldwide. Although high-resource areas may use additional methods, and in low-resource areas no care may be available at all, the international standards set by the Tuberculosis Coalition for Technical Assistance [54], of which the World Health Organization is a part, set a diagnostic path for pulmonary (lung-involved) tuberculosis including the following steps:

1. A patient presenting to a medical staff member with a cough of more than 2 weeks' duration in an area of high tuberculosis prevalence is evaluated further for possible TB infection.
2. If the patient can produce sputum, at least two samples should be evaluated by sputum microscopy.
3. In areas where chest x-rays (CXR) are available, an x-ray is usually taken first. If the CXR suggests TB, then sputum microscopy is nonetheless called for as well, since a CXR alone is considered insufficient for positive tuberculosis diagnosis.
4. Culture of sputum samples should be performed for any patients for whom sputum microscopy results are negative but who have positive CXR indications and / or do not respond to broad-spectrum antibiotics.<sup>1</sup>
5. Response to antibiotic therapy needs to be monitored using sputum microscopy, with additional samples being evaluated at 2 months and potentially again at 3 months after the start of treatment.

Sputum microscopy thus plays a central role not only in the initial diagnosis, but in evaluating the efficacy of subsequent care as well.

---

<sup>1</sup>Despite this WHO recommendation, this is rarely done due to lack of resources and difficulties in implementation.

## New technological opportunities

Starting in 2006, the advent of cell-phone cameras led us to consider the possibilities they might hold for mobile and remote diagnosis. We were not alone in this [36], nor were we alone in considering the use of the newly-available high-power light-emitting diodes (LEDs) for fluorescence microscopy [2, 43, 44], since their long life (often  $\geq 10,000$  hours), lack of cooling needs, and low power consumption enhances the tractability of doing fluorescence microscopy in low-resource settings.

Concurrently with these improvements in available hardware, a new version of the Auramine stain became commercially available [101, 47] at low cost. This stain was quickly evaluated and adopted at research hospitals such as Johns Hopkins because it reduced the time required to do the staining procedure by more than a factor of ten, from 22 minutes to 2 minutes. Since what matters is the full time-to-diagnosis, reduction in the sample-preparation time is an important factor — it matters little if one can read a slide in 4 minutes if preparing the slide takes 30 minutes or more. The advent of the 2-minute stain thus seemed to us to offer the opportunity for a significant advance in diagnostic approach.

While others had considered use of LEDs and camera-phones in conjunction with standard light microscopes, we thought that it might be possible to combine them into a portable microscope, which, in combination with the new fast staining procedure and the ability to upload the images for remote evaluation, might provide a path to increased access to diagnostic sputum microscopy for patients in low-resource settings. Chapter 2 addresses our effort to realize such a device.

## Chapter 2

# Mobile Phone Based Microscopy

### 2.1 Introduction

Our initial foray into mobile-network connected portable digital microscopy naturally involved a cellphone. Cellphones are ubiquitous in the developing as well as the developed world, and often connectivity is better in countries where there is no wired network to compete for resources — many countries have effectively leapfrogged to set up their first widespread telecommunications infrastructure with mobile technology.

Phones offer the tantalizing promise of low-cost and easy access, and many in the group were eager to pursue the possibilities. At the time (2007), pixel-counts were low (2 Mpixels was considered very good) limiting fields of view that could be acquired without aliasing, and the control over the cameras that the phones offered was poor. Nonetheless, it turned out to be reasonable to take microscope-quality images with a cellphone.

My own interest was piqued by the possibilities for mating such a system with the newly emerging high-power LEDs, providing the possibility for portable fluorescence imaging. In addition, once a digital image was acquired, the phones offered the possibility not just to transmit images to remote physicians (physicians who might be in short supply), but to do rapid on-phone image processing — counting bacilli, for a start, but perhaps also the ability to do automated image-processing-based diagnosis.

We were successful in demonstrating proof-of-concept for such a system, imaging malaria parasites within blood cells and the sickled cells of the eponymous anemia in blood smears. Moreover, the fluorescence approach worked, and we were able to image Auramine O-stained TB bacilli and to use automated processing to isolate and count them. The details of that effort are recounted in this chapter.

## 2.2 Mobile Phone Based Clinical Microscopy for Global Health Applications

David N. Breslauer<sup>1,2,#</sup>, Robi N. Maamari<sup>2,#</sup>, Neil A. Switz<sup>3</sup>, Wilbur A. Lam<sup>2,4</sup>, Daniel A. Fletcher<sup>1,2,3</sup>

<sup>1</sup>UCSF/UC Berkeley Bioengineering Graduate Group; <sup>2</sup>Department of Bioengineering, University of California Berkeley; <sup>3</sup>Biophysics Graduate Group, University of California Berkeley; <sup>4</sup> Department of Pediatrics, University of California San Francisco.

# These authors contributed equally to this work.

As published in: PLoS ONE 4(7): e6320. doi:10.1371/journal.pone.0006320, 2009.

PLoS Journals are open-access, and this material is reproduced here under the Creative Commons Attribution License.

### Abstract

Light microscopy provides a simple, cost-effective, and vital method for the diagnosis and screening of hematologic and infectious diseases. In many regions of the world, however, the required equipment is either unavailable or insufficiently portable, and operators may not possess adequate training to make full use of the images obtained. Counterintuitively, these same regions are often well served by mobile phone networks, suggesting the possibility of leveraging portable, camera-enabled mobile phones for diagnostic imaging and telemedicine. Toward this end [26] we have built a mobile phone-mounted light microscope and demonstrated its potential for clinical use by imaging *P. falciparum*-infected and sickle red blood cells in brightfield and *M. tuberculosis*-infected sputum samples in fluorescence with LED excitation. In all cases resolution exceeded that necessary to detect blood cell and microorganism morphology, and with the tuberculosis samples we took further advantage of the digitized images to demonstrate automated bacillus counting via image analysis software. We expect such a telemedicine system for global healthcare via mobile phone - offering inexpensive brightfield and fluorescence microscopy integrated with automated image analysis - to provide an important tool for disease diagnosis and screening, particularly in the developing world and rural areas where laboratory facilities are scarce but mobile phone infrastructure is extensive.

### Funding

This work was supported by grants from the Center for Information Technology Research in the Interest of Society, the Blum Center for Developing Economies, Microsoft Research, Intel, and the Vodafone Americas Foundation to DAF. DNB acknowledges an NDSEG Grad-

uate Fellowship for funding. NAS has been funded through an NSF IGERT grant to the UC Berkeley Biophysics Group. The funders had no role in study design, data collection and analysis, decision to publish, or preparation of the manuscript.

## Competing Interests

The authors are co-inventors on a patent application filed by the University of California, Berkeley on the technology described in this manuscript.

## Introduction

Light microscopy is an essential tool in modern healthcare. The advent of digital imaging has only enhanced this diagnostic role, as sample images are now frequently transferred among technologically-advanced hospitals for further consultation and evaluation, a role important enough that a medical communication standard (DICOM [26]) has been widely adopted for the handling of digital images. Unfortunately, much of the power of light microscopy, especially fluorescence imaging and the opportunity for remote consultation and electronic record keeping, remains inaccessible in rural and developing areas due to prohibitive equipment and training costs. This is especially problematic since the diagnosis, screening, and monitoring of treatment for many diseases and infections endemic to such areas - e.g. tuberculosis (TB), malaria, and sickle cell disease - depend on light microscopy as a screening tool or a definitive diagnostic test [109, 52, 94, 19, 108]. A recent convergence of technologies is making it possible to change the way microscopy is performed in developing countries. Given the ubiquity of mobile phone networks, the fact that many mobile phones are now equipped with digital cameras, the increase in computational power of mobile phones, and the advent of inexpensive high-power light emitting diodes (LEDs), we believe that these technologies can be combined to create an inexpensive and powerful tool for light (and especially fluorescence) microscopy in developing regions. While the concept and practice of telemedicine has existed for decades, it has only recently begun a shift to wireless platforms [131, 8, 111], and new avenues are now opening for developing mobile phone enabled medical technology [111, 42, 35]. An additional advantage to using a phone-based microscope is that mobile phones are essentially computers that can be used for digital image processing as well as electronic medical record keeping and communication. Our initial device development efforts have been aimed at using the digital imaging capabilities, mobile connectivity, and computational power of a camera-enabled mobile phone to capture high-resolution microscopy images and perform subsequent image transmission or analysis. It has been previously demonstrated that a camera-enabled mobile phone can be used to capture images from the eyepiece of a standard microscope [35] and that microscopy images can be wirelessly transmitted for subsequent analysis [134]. However, our goal was to demonstrate the feasibility of creating an entirely integrated and portable mobile phone microscopy system. With the growing use of fluorescent stains in sample preparation to increase diagnostic sensitivity and specificity, we furthermore sought to incorporate fluorescent

imaging capabilities into our mobile microscopy system and test the use of digital image processing for image analysis. Here we report the development of a high-resolution microscope attachment for camera-enabled mobile phones that is capable of both brightfield and fluorescence imaging. We demonstrate the ability to use this system to capture brightfield digital color images of malaria parasites in thin and thick blood smears, sickled red blood cells in peripheral blood smears, and, using fluorescence, tuberculosis bacilli in Auramine O-stained sputum smears. Furthermore, we demonstrate the potential for improving diagnostic efficiency by using simple image processing software to label and count tuberculosis bacteria in a captured image, relieving healthcare workers of the time-consuming and error-prone task of counting by eye. We believe that by integrating these technologies, healthcare workers in remote regions equipped with microscopy-enabled mobile phones could take diagnostic images of patient samples (blood, sputum, etc.), perform on-board image analysis and/or wirelessly transmit those images off-site for medical record keeping, epidemic tracking, or further analysis by clinical experts.

## Results

Both the brightfield and fluorescence instruments are designed to work with a typical camera-enabled mobile phone (Figure 2.1a, b). The system uses standard, inexpensive microscope eyepieces and objectives; magnification and resolution can be adjusted by using different objectives. For this study, we used a 0.85 NA 60X Achromat objective and a 20X wide field microscope eyepiece, resulting in a system field-of-view of  $\sim 180 \mu\text{m}$  diameter, an effective magnification onto the camera face of  $\sim 28X$ , and a measured spatial resolution of  $\sim 1.2 \mu\text{m}$ . The effective magnification figure requires care in interpretation as the image can take on greater magnification via digital enlargement. Resolution is a more fundamental parameter, and we estimated it to be  $\sim 1.2 \mu\text{m}$ , based on the full width at half maximum (FWHM) of the system point-spread function (PSF, see Materials and Methods). This is a factor of three larger than the nominal Rayleigh resolution limit of  $0.4 \mu\text{m}$  for the system, to be expected since the (purposefully inexpensive) objectives used are uncorrected for field curvature and other aberrations, reducing resolution away from the field radius of best focus. Imperfections and aberrations in the mobile phone lens will also contribute to the non-diffraction limited performance. Despite these limitations, the mobile phone camera was able to capture high-resolution images of blood and sputum samples useful for diagnosis.

Ambient light (without a condenser) was typically sufficient for brightfield imaging, but we also used a white LED for illumination in darker conditions. For fluorescence microscopy we utilized a simple and inexpensive trans-illumination geometry incorporating an LED excitation source and filters in the optical train (Figure 2.1a). High-power LEDs are now available in a wide range of emission bands, allowing for the matching of excitation wavelength with a variety of potential fluorophores. As others have also noted, the low cost, high robustness to mechanical shock and environmental conditions, low power requirements, ambient operating temperatures, and  $\sim 50,000$  hour lifetimes of LEDs make them particularly suitable for use in portable systems and systems designed for use in developing areas

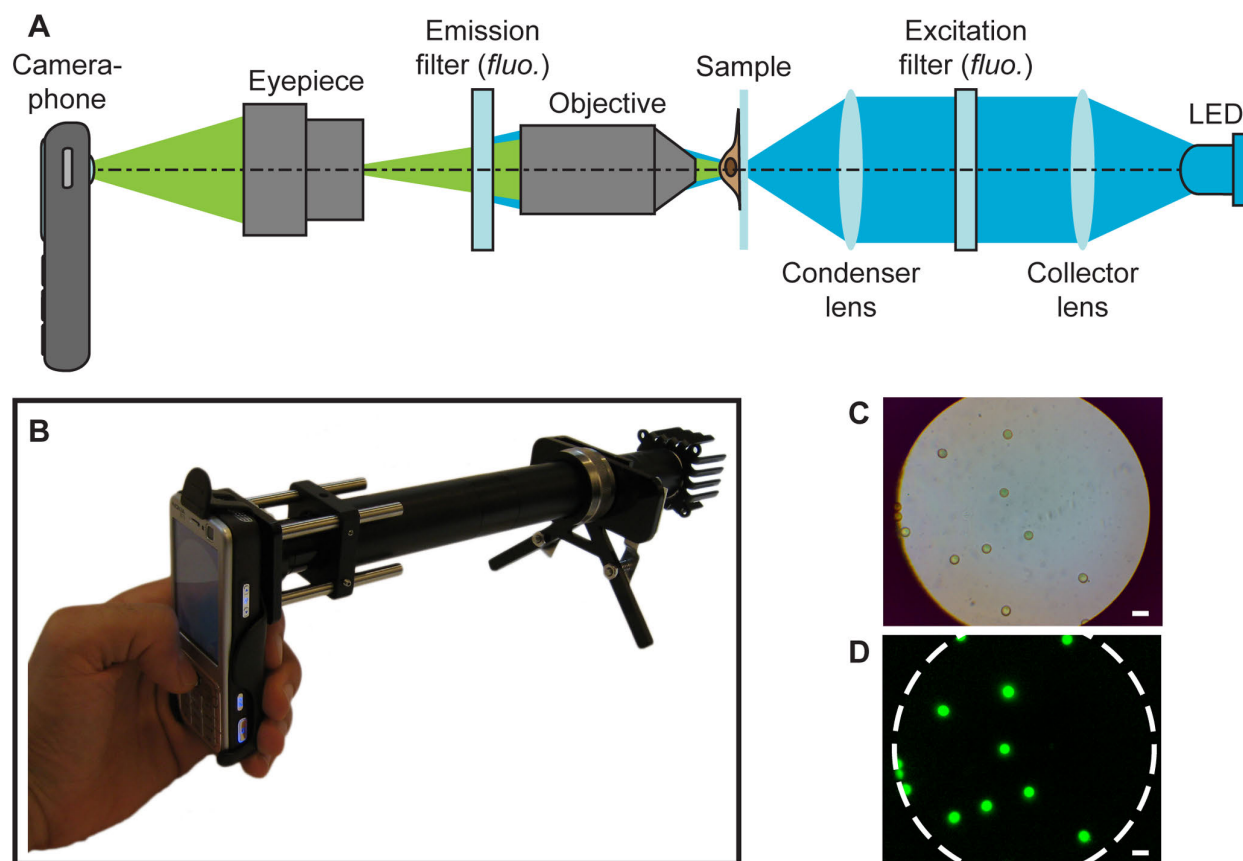


Figure 2.1: **Mobile phone microscopy layout schematic, prototype, and sample images.** (a) Mobile phone microscopy optical layout for fluorescence imaging. The same apparatus was used for brightfield imaging, with the filters and LED removed. Components only required for fluorescence imaging are indicated by "fluo." Not to scale. (b) A current prototype, with filters and LED installed, capable of fluorescence imaging. The objective is not visible because it is contained within the optical tubing, and the sample is mounted adjacent to the metallic focusing knob. (c) Brightfield image of 6  $\mu\text{m}$  fluorescent beads. (d) Fluorescent images of beads shown in (c). The field-of-view projected onto the camera phone CMOS is outlined. Scale bars are 10  $\mu\text{m}$ .

where replacement parts may be unavailable or unaffordable [109, 51, 59]. In our fluorescence system, illumination was provided by a high-power blue LED, emitting within the excitation range of the fluorescent Auramine O stain commonly used for detection of TB bacilli in sputum samples. Sensor integration time for the phone was unavailable, so the limiting system sensitivity could not be determined. Whereas an epi-illumination geometry is generally used to minimize background from the illumination source in fluorescence microscopy, we found that the Auramine O-stained TB fluorescence was more than sufficiently bright for bacillus identification using our trans-illumination geometry, which in turn reduces the complexity and cost of our system- an important consideration given the resource-poor settings where it could be of use.

### **Brightfield Imaging of Malaria and Sickle Cell Anemia**

To characterize the mobile phone microscope for clinically relevant applications, we used brightfield illumination to capture high-resolution images of both thin and thick smears of *P. falciparum* malaria-infected blood samples, as well as of sickle cell anemia blood samples (Figure 2.2).

Malaria is a parasitic disease endemic to many parts of the developing world and is a major global health concern. Diagnosis of malaria is usually performed via observation of parasites in a Giemsa-stained "thick" peripheral blood smear; subsequent speciation is obtained (if desired) from a follow-up examination of a similarly stained thin blood smear at higher magnification and resolution for parasite morphology and species identification [52, 76]. Additionally, it has previously been demonstrated that malaria can be effectively diagnosed from e-mailed smear images [84]. Figures 2.2a and 2.2b show color, brightfield images of thick and thin Giemsa-stained smears of malaria-infected red blood cells, respectively, captured on the mobile phone microscope. The quality of the malaria images could be improved by use of a higher NA objective; however, especially for the thick smear (more widely used for screening) the current images are already suggestive of the potential for diagnostic utility.

Sickle cell anemia, another disease that disproportionately affects the developing world, can be diagnosed via blood smears displaying abnormally (sickle) shaped red blood cells (RBCs). Diagnosing and identifying sickle cell patients early in life would enable the implementation of preventive measures to decrease the complication rate and overall disease burden of this life-threatening illness. Our system provides enough image resolution and contrast for the direct observation of sickled cells in blood smears taken from patients with hemoglobin SS disease (Figure 2.2c), with no additional contrast-enhancing techniques (e.g. staining or phase contrast). If needed, however, significant additional contrast can be achieved by the simple expedient of applying an illumination source at an oblique angle to the sample (data not shown). This mobile phone microscopy system could prove to be particularly useful for point-of-care screening of newborns for sickle cell disorders, to identify and treat patients before the onset of symptoms in resource-poor nations, a process already mandatory in the United States and other developed countries [121, 110, 118].

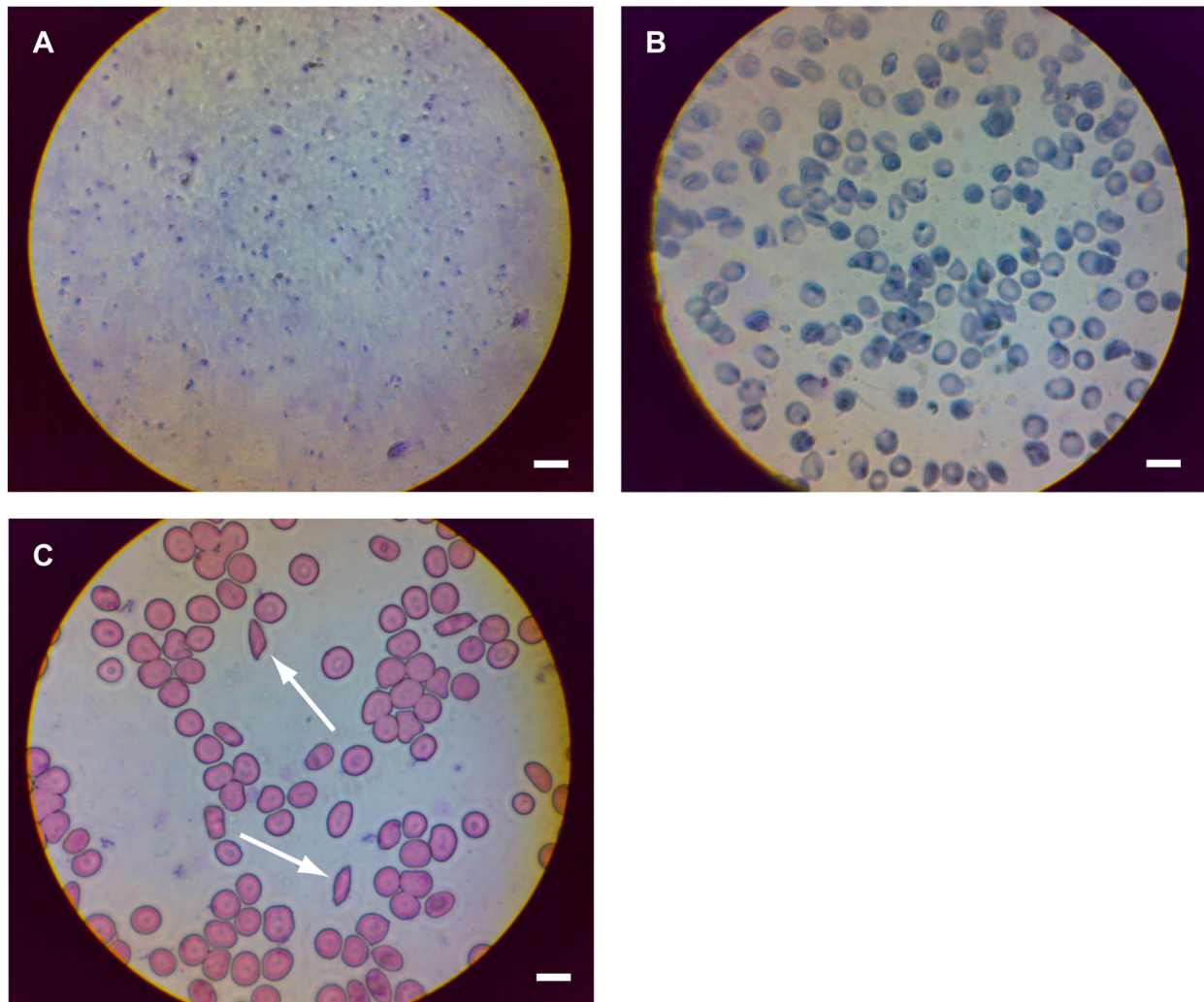


Figure 2.2: **Mobile phone microscopy images of diseased blood smears.** (a) Thick smear of Giemsa-stained malaria-infected blood. (b) Thin smear of Giemsa-stained malaria-infected blood. (c) Sickle-cell anaemia blood smear. White arrows point to two sickled red blood cells. Scale bars are 10  $\mu\text{m}$ .

### Fluorescence Imaging of Tuberculosis and Automated Image Analysis

TB is a major world health concern, and treatment entails monitoring of patients over long (6-9 month) periods. While the standard for initial diagnosis is the use of brightfield imaging of a Ziehl-Neelsen stained sputum smear, fluorescent stains are increasing in popularity due to reduced toxicity in preparation, improved ease of reading, and possibly increased accuracy of the resulting diagnosis [109, 43]. Their adoption in the developing world for both diagnosis and monitoring of TB is, however, hindered by a lack of fluorescence microscopy equipment [109, 108, 59] generally due to the cost of the equipment and cost of maintenance.

Using fluorescence illumination, we were able to capture images of Auramine O-stained *M. tuberculosis*-positive sputum smears (Figure 2.3a). The resolution of the system was high enough to allow easy identification of individual TB bacteria in the sample, as well as to observe the standard rod-shaped morphology. While we subtracted the background intensity from all images as a matter of course, bacilli were bright enough that background subtraction was not in fact required for reliable identification.

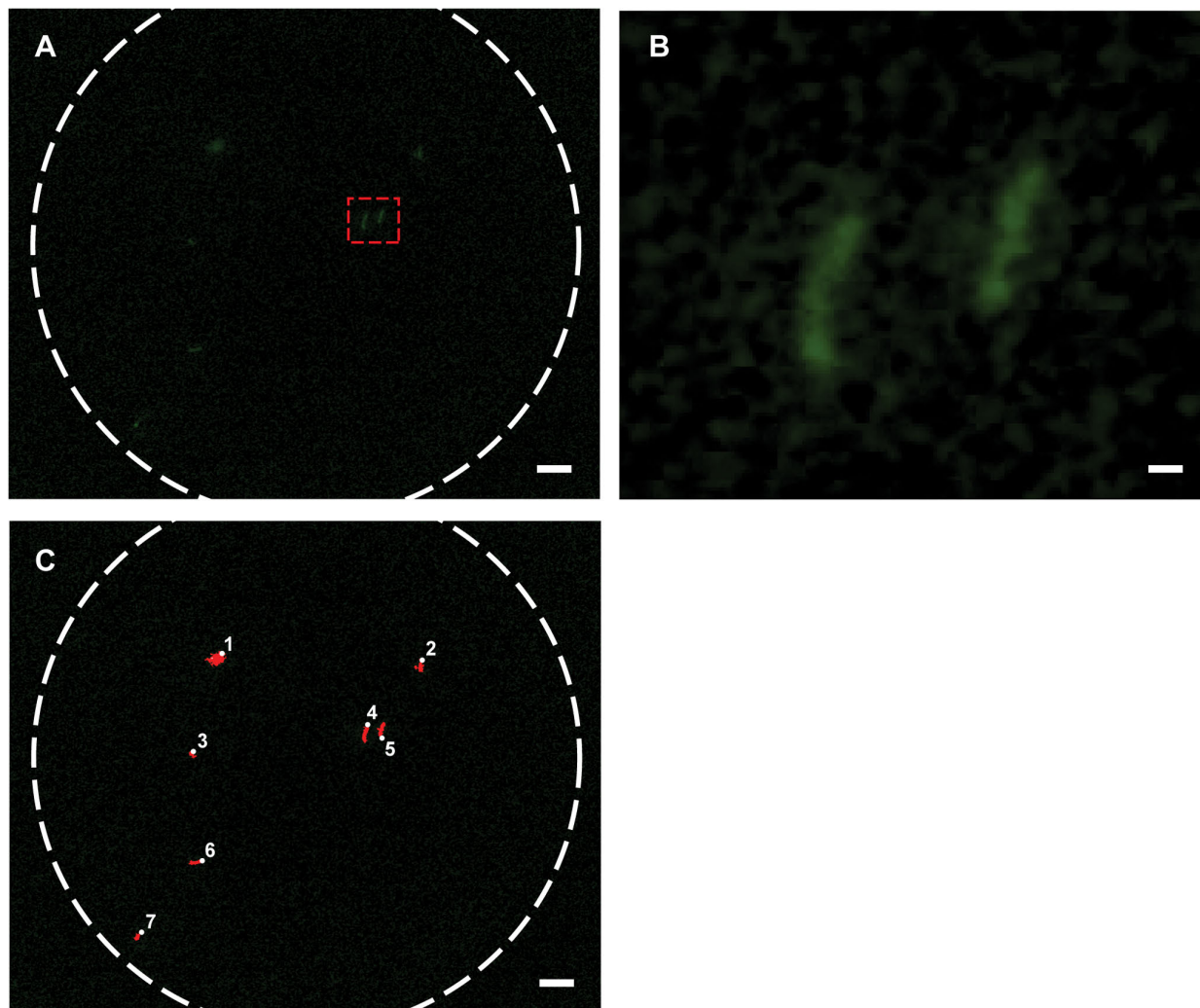


Figure 2.3: **Fluorescence mobile phone microscopy images of tuberculosis in sputum.** (a) Fluorescence image of Auramine O-stained TB sputum sample. (b) Enlarged view of two tuberculosis bacilli from red-outlined area in (a). (c) Automated counting of fluorescently-labeled tuberculosis bacilli; counted bacilli are numbered and set to red in the image. Scale bars in (a) and (c) are  $10\ \mu\text{m}$ , scale bar in (b) is  $1\ \mu\text{m}$ .

Current standards for the diagnosis of TB using the non-fluorescent Ziehl-Neelsen stain

require the screening of upward 100 fields-of-view of  $\sim 180 \mu\text{m}$  in diameter [106], cumbersome with our system and similarly tedious by eye on a conventional microscope. One of the principal advantages of using the fluorescent Auramine O stain rather than the absorptive Ziehl-Neelsen stain for TB screening is that a lower power (20X) objective may be used [109], with resultantly larger fields of view and thus a reduction in the number of fields (by a factor of 25) which must be examined to cover the same slide area. Such objectives have the added advantage of being less expensive; however, they also have lower light-gathering power making them more challenging to use for fluorescence applications. In our testing we found that a 20X 0.4 NA objective (with a theoretically 5.7X lower light collection efficiency than the 0.85 NA objective) was more than adequate for acquiring images of Auramine O-stained TB bacilli (data not shown). In order to take full advantage of the objective field of view, a sufficient number of detector pixels are required. While our phone had  $\sim 3.2$  Megapixels (Mp), camera-phones are well on the way to the  $\sim 4$ -8 Mp required to image the entire field at maximum resolution.

In addition to the capture and transmission of data, the fact that mobile phones are essentially embedded computer systems offers the opportunity for significant post-processing of images. To demonstrate the diagnostic potential of image processing in this application, we carried out automated bacillus counting of the fluorescent TB images (Figure 2.3b). For reasons of simplicity we implemented the automated particle count on a laptop computer onto which we had transferred the images, but phone computational resources are sufficient for such tasks to be performed on-phone, providing both an immediate efficiency gain in slide analysis as well as the longer-term potential for automated microbe and pathogen identification.

## Discussion

We have developed a microscope attachment for a camera-enabled mobile phone such that it can be used as a platform for high-resolution clinical light microscopy. The system can reliably capture images of malaria-infected red blood cells from both thin and thick blood smears, as well as images of sickled red blood cells. Additionally, we have demonstrated that mobile phone cameras can be adapted for high-resolution LED-based fluorescent microscopy, using fluorescence imaging of Auramine O-stained sputum smears as a test case.

Microscope-enabled mobile phones have the potential to significantly contribute to the technology available for global healthcare, particularly in the developing world and rural areas where mobile phone infrastructure is already ubiquitous but trained medical personnel, clinical laboratory facilities, and clinical expertise are scarce. By using existing communication infrastructure and expanding the capability of existing mobile phone technology, mobile phone microscopy systems could enable greater access to high-quality health care by allowing rapid, on- or off-site microscopic evaluation of patient samples. As an example, mobile phone microscopy as demonstrated here could provide a rapid, point-of-care method for monitoring TB patients. Such a system would support the World Health Organization's DOTS program, which was established to guide TB eradication efforts by emphasizing, among other factors,

the role of quality-assured technology, standardized treatment, and enhanced recording and reporting [94]. With the advent of new 2-minute rapid-staining protocols [89, 46], sample evaluation could potentially be performed in real time while a patient is still in the presence of a healthcare worker, rather than requiring days or weeks. Since we are developing a technology that makes the current and long-standing internationally accepted standards for disease screening in developing countries more portable - rather than creating an entirely new diagnostic assay - we anticipate that a relatively fast time to adoption by clinicians and health workers may be possible.

Not only could such a mobile phone microscopy system help alleviate the problems of inadequate access to clinical microscopy in developing and rural areas, but it would provide those areas remote access to digital record keeping, automated sample analysis, expert diagnosticians, and epidemiological monitoring - the latter enhanced by the ease of location-tagging patient data by cellular triangulation or GPS location data. Combining the mobile phone microscopy system with automated sample preparation systems could address challenges associated with use by minimally-trained health workers and the time involved in imaging multiple fields of view [132]. While future field studies are planned to evaluate the reliability and ease of use of mobile phone microscopy, our present system serves as a proof of principle that clinical imaging of hematologic and infectious diseases is possible with conventional mobile phone camera technology combined with a custom microscopy attachment.

## Materials and Methods

All mobile phones were Nokia N73 camera phones, equipped with a 3.2 megapixel (2048 x 1536 pixel) CMOS camera with a 5.6 x 4.2 mm sensor, yielding an  $\sim 2.7 \mu\text{m}$  pixel spacing. The phone and optical components were mounted using an optical rail system, and laid out as in Figure 2.1a. A functional, handheld prototype is shown in Figure 2.1b.

The imaging system consisted of a 20X wide field microscope eyepiece (Model NT39-696, Edmunds Optics) separated by 160 mm from a microscope objective (60X 0.85NA DIN Achromat objective, 160 mm tube length, Model NT38-340, Edmunds Optics). The eyepiece was separated from the camera phone by approximately the focal length of the camera (5.6 mm). For fluorescence imaging, the illumination source was a Luxeon III 455 nm LED (Model LXHL-LR3C, Philips Lumileds) attached to a 3 x 3 inch microprocessor heat sink with silver conductive epoxy and driven at 700 mA to provide  $\sim 275$  mW nominal optical output power. Directly mounted to the LED was a 5deg spot lens (OP005, Dialight), followed by a 25.4 mm focal length biconvex lens placed approximately 11 cm from the spot lens and acting as a condenser. Resultant excitation intensity at the sample was  $2.0 \text{ mW}/\text{mm}^2$ . An excitation filter (D460/50x, Chroma) was placed between the spot and condenser lenses, and an emission interference filter (Chroma D550/50m) was placed as close as practical to the objective back focal plane. Focus was adjusted by moving the sample position.

Brightfield images were captured using the phone's default camera settings, with the flash disabled. Fluorescent images were captured in the camera's "Night" mode, with the flash disabled. Night mode slightly increases exposure time of the camera to a maximum

of 0.2 s, but likely performs software-based contrast adjustments on the image as well. We were not able to manually set the exposure time; however, single images provided adequate signal-to-noise for easy viewing and analysis. For all fluorescent images, we subtracted a background image (captured from a sample area with no fluorescent signal) from the sample image; such subtraction is of low computational overhead and, though we did not do so in these experiments, would be simple to implement in a user-transparent manner as part of the overall image acquisition algorithm. After background subtraction, the JPEG sample image was split into its red-green-blue layers and only the green channel retained. No significant signal was observed in the other channels, despite the demosaicing and JPEG compression implemented on the phone. Images filled a  $\sim 4.8$  mm diameter area of the sensor; surrounding blank image areas have been cropped from Figures 2.1c, 2.1d, 2.2, 2.3a, and 2.3c for display purposes.

To characterize the resolution of the system, 100 nm fluorescent beads (Fluoresbrite Plain YG Microspheres, Polysciences, Inc.) were diluted 10,000-fold in deionized water and allowed to dry on a 200 line-pair/mm Ronchi ruling. After acquiring a best-focus image of the beads, the emission filter was removed to capture a brightfield image of the Ronchi ruling without refocusing, which we used for calibrating scale (data not shown). We defined resolution as the FWHM of the measured PSF, which in this case was  $1.2 \mu\text{m}$ . This value for resolution should be a slightly conservative estimate since the bead diameter was not deconvolved from the result. The resolution was obtained by averaging the FWHM of seven different beads spread randomly in the field of view. Unfortunately due to lack of information on the phone algorithms for both demosaicing of the color pixel array and JPEG compression, determining the theoretical system resolution is not possible. The optical magnification of 28X is the product of the  $2.7 \mu\text{m}$  pixel size and 95 nm/pixel scale obtained using the Ronchi ruling. The system field-of-view was measured directly from an image of the Ronchi ruling.

Automated counting of samples performed on a computer using ImageJ [95]. Image threshold was set at three standard deviations above the pixel mean value; bacilli were required to have an area of at least one PSF,  $1.57 \mu\text{m}^2$ , or 125 pixels, with no upper size limit. While more sophisticated algorithms can be envisioned, the count derived in this manner matched that we performed by eye.

Malaria and sickle cell samples were obtained from patients confirmed to have each disease. TB samples were culture confirmed.

## Ethics Statement

Use of these patient samples was approved by the institutional review board of the University of California, San Francisco. Written informed consent was obtained for all patient samples.

## Acknowledgments

The authors would like to thank Thomas Hunt, Chris Rivest, Wendy Hansen, Jesse Dill, Andrew Fandrianto, and Erik Douglas for helpful discussions. All disease samples were obtained from University of California, San Francisco. Malaria infected blood smears were provided by Jiri Gut and Philip Rosenthal, MD. Sickle cell anemia blood smears were provided by Wilbur Lam, MD. Tuberculosis infected sputum smears were provided by Gail Cunningham and Geoff Brooks, MD. This work was supported by grants from the Center for Information Technology Research in the Interest of Society, the Blum Center for Developing Economies, Microsoft Research, Intel, and the Vodafone Americas Foundation to DAF. DNB acknowledges an NDSEG Graduate Fellowship for funding. NAS has been funded through an NSF IGERT grant to the UC Berkeley Biophysics Group.

## Author Contributions

Conceived and designed the experiments: DNB RNM NS WL DAF. Performed the experiments: DNB RNM NS. Analyzed the data: DNB RNM NS WL DAF. Contributed reagents/materials/analysis tools: WL. Wrote the paper: DNB RNM NS WL DAF. Designed the devices and experiments in this study: DNB RNM NAS DAF. Built the devices and conducted the experiments: DNB RNM NAS. Guided experiments and obtained samples: WAL.

# Chapter 3

## Design

Having succeeded with a proof-of-concept, I and others in the lab began to think more deeply about where the benefits of the newly emerging technologies could be best applied. One early lesson was that the rapid product turnover in the cellphone market, coupled with the unwillingness by at least one top-tier manufacturer to provide even basic information and software access for camera control, made it extremely difficult to both prototype and support developed devices over periods of longer than a few months. Furthermore, while it was possible to build a prototype around a cellphone, the final performance, cost and robustness of such a prototype was not sufficiently beyond what could be envisioned for a dedicated embedded system using a board computer, touchscreen, and 3G mobile wireless module, and the latter approach would be vastly easier to both develop and support. Lastly, field-of-view and (not unrelated) ease-of-use is critical to successful diagnostics microscopy, and both were limited using the cellphones of the era.

As a result, I shifted my design efforts to an embedded approach, first with the intent of building the touchscreen and computer in, and later taking advantage of the inexpensive laptops, hardened and designed for use in the developing world, made possible by the one-laptop-per-child (OLPC) program. As it evolved, the device became a 20 x 20 x 10 cm and 3 kg in weight, connecting to an OLPC-style laptop. To avoid draining the laptop battery too quickly, I included a battery in the device which allows several days of fairly continuous use before requiring recharging using a USB cable or 12V “wall-wart” power supply.

The major design considerations and engineering developments involved in building the prototype and then moving to quantity-15 manufacture with an outside firm (The Pilot Group, in Monrovia, CA) are discussed in this chapter, and technical validation of the diagnostic concept in the next.

### 3.1 Basic Optical Considerations

In the case of sputum microscopy, deciding on certain specifications is simplified because the technique is already in use. As a result, it was already known that a typical 20X 0.4NA

microscope objective provides sufficient resolution (in conjunction with the human eye and a 10X eyepiece) to allow for successful diagnosis using fluorescence imaging. Similarly, it was known that the San Francisco Department of Public Health (SFDPH) Mycobacterial Division labs used epifluorescence microscopes using a mercury-arc lamp provided ample illumination for diagnostic use. In the case of SSFDPH, the standard objectives are Leica 20X 0.4NA and 63X 0.9NA, both designed for use with 0.17 mm coverslips, though these are not actually used there for sputum smears, and also used widefield 10X "PeriPlan" eyepieces with Field Number (FN) 18.

## Required resolution

There are several useful specifications which can be obtained from this information. The first is resolution; the Rayleigh resolution for an point object is given by

$$\delta = 0.61 \frac{\lambda}{\text{NA}}, \quad (3.1)$$

where NA is defined by

$$\text{NA} = n \sin(\theta) \quad (3.2)$$

with  $n$  = index of refraction of the immersion medium for the sample; unless otherwise specified,  $n = 1$  (air) throughout this thesis.

Equations 3.1 and 3.2 yield  $\delta = 0.76 \mu\text{m}$  for an object emitting green ( $\lambda \sim 500 \text{ nm}$ ) light and interrogated using a 0.4NA objective. Beyond this, as I will discuss later, low cost objectives such as typical 20X 0.4NA ones typically do not work at the diffraction limit across much of their field of view. In fact, usually the effective "as-built" resolution of such objectives is  $\sim 2\text{X}$  the Rayleigh resolution, implying that a working resolution of  $\delta \sim 1.5 \mu\text{m}$  across the field of view is likely to be sufficient.

## Required field of view

Since the intermediate image is 18 mm in diameter (as specified by the FN 18 eyepieces and objective; these numbers are typical of most low-cost microscopes), the sample-references area viewed is  $\text{FN} / \text{M} = 18 \text{ mm} / 20\text{X} = 0.9 \text{ mm dia.}$

Although SFDPH examines the entire smear surface, standard sputum microscopy technique is to read a single "length" along the long axis of the approximately 1 cm x 2 cm oval smear area. Hence, to achieve equivalent sensitivity the interrogated area of the smear should be  $\sim 18 \text{ mm}^2$ .

## Required excitation power

The intensity of imaged fluorescence emission scales with, among other variables, the excitation intensity (power per unit area) at the sample [79], the collection efficiency (CE),

the square of the optical magnification  $M$ , the quantum efficiency (QE) of the detector, and  $\tau$ , the integration (exposure) time used:

$$\text{Pixel value}_{\text{Image}} \propto \frac{1}{M^2} \cdot I_{\text{sample}} \cdot \text{CE} \cdot \text{QE} \cdot \tau \quad (3.3)$$

where  $I_{\text{sample}}$  is the excitation intensity at the sample.<sup>1</sup> Rough calculations of these parameters allow estimation of the required excitation for a portable device, and help set the design difficulty.

At the time I began this work, typical QE values for low-cost CCD and CMOS sensors were in the  $\sim 25\%$  range, significantly higher than rough estimates of  $\sim 7\%$  for the human eye. Estimates of CE and integration time will be similar for the camera and the eye, the former because both systems would use the same NA objective, and the latter because use of video-rate imaging to allow for smooth focus adjustment by the user will require integration and new-image display times shorter than that of the eye (video rate is effectively *defined* as a bit faster than the integration time of the human eye, and is  $\sim 25$  Hz, so an appropriate integration time estimate is  $\sim 40$  ms). This leaves only magnification and incident power to be estimated.

The true optical magnification of a microscope is not the number usually specified. Doctors, and most others, specify the (apparent) magnification of a microscope as  $M_{\text{objective}} \cdot M_{\text{eyepiece}}$ , or 200X for a 20X objective in conjunction with a 10X eyepieces. The actual magnification onto the sensor, in the case the human retina, is quite different.

The effective focal length of the typical human eye is  $\sim 17.1$  mm [103], and the focal length of an eyepiece is given by  $250$  mm /  $M_{\text{eyepiece}}$  [105] (essentially the magnification of an eyepiece is defined as the apparent angle subtended by the object when using the eyepiece to the angle subtended by the actual object when held 250 mm from the eye [103]). Following the optics of the microscope, a 20X objective will form an intermediate image (magnified 20X) of the sample magnified for the eyepieces; the combination of 10X eyepieces and an average human eye will then relay this image to the retina with additional (de)magnification  $M = 17$  mm /  $25$  mm = 0.68X. As a result, the actual optical magnification from the sample to the retina is  $20 \cdot 0.68 \sim 14$ X.

As I will discuss later, the optical magnification used in precision digital imaging should at a minimum exceed the Nyquist sampling criterion for the image. Since the highest spatial frequency present at the image plane in an incoherent optical system is

$$k_{\text{max}} = \frac{2 \text{NA}_{\text{Obj}}}{M \lambda} \quad (3.4)$$

where  $M$  is the magnification of the optical system, from the sample to the detector, the required magnification  $M$  will be determined by the Nyquist requirement to sample at least twice (i.e., have two pixels) per cycle of the highest spatial frequency:

---

<sup>1</sup>The QE is actually a function of wavelength,  $\text{QE}(\lambda)$ , and must be integrated as a product with the emission spectrum incident on it; c.f. Equations 3.16 and 3.17 for additional detail.

$$M_{\text{Nyquist}} \geq \frac{4 \text{NA}_{\text{Obj}} d_{\text{pixel}}}{\lambda}. \quad (3.5)$$

Using  $\lambda \sim 0.5 \mu\text{m}$ , 0.4 NA, and a typical pixel value for the time (2007) of  $\sim 5 \mu\text{m}$ , Equation 3.5 yields an estimated required value of  $M$  for a digital system of  $M \geq 16X$ , quite close to the value estimated above for the human eye.

Since the magnification, collection efficiency, and integration time between the typical microscope and a digital system will be roughly similar, the relative expected visibility of the fluorescent bacilli will depend primarily on the QE difference ( $\sim 3.5X$  higher for a camera) and the power available from a mercury (Hg) or Xenon (Xe) arc lamp. The latter falls in the ballpark of 346 mW, for a 60 nm band in the neighborhood of the Auramine O fluorescent excitation from 150 W Xe arc lamp (Oriel model 6255) with an  $\sim 1 \text{mm}^2$  arc [12]. However, if used in epifluorescence with a 0.4NA objective, the arc will be magnified by

$$M = \frac{\text{NA}_{\text{Collector}}}{\text{NA}_{\text{Objective}}}. \quad (3.6)$$

The collector used in Oriel's calculation is  $f\#/1.4$ , which is identical to 0.7 NA ( $f\#$  is defined as  $(2 \text{NA})^{-1}$ ). Consequently the magnification of the arc image will be  $M = 0.7 / 0.4 = 1.8X$ , and the intensity of the arc image at the sample will decrease by the inverse square of that linear magnification,  $M^2 = 0.31$ . As a result, a rough estimate of the excitation power at the sample is  $\sim 110 \text{mW}$ , or (assuming 1:1 imaging of the  $\sim 1 \text{mm}^2$  arc), an excitation intensity of  $\sim 110 \text{mW} / \text{mm}^2$ .

Coupled with  $\sim 3.5X$  higher QE using a camera vs. a human eye, this suggests that an intensity of  $\sim 30 \text{mW} / \text{mm}^2$  at the sample would be ballpark-sufficient for adequate imaging. Practically, this value is likely to be somewhat low, since Hg arc lamps have a strong line at 436 nm that matches well with the Auramine O excitation maximum at 431 nm, while blue LEDs, as discussed later, tend to have emission centered near 455 nm [74], where Auramine absorption is 60% of its peak value and dropping fairly quickly [92]. As a result a figure of closer to 50-75  $\text{mW} / \text{mm}^2$  required at the sample is a safer assumption.

## Initial Optical Specifications

As will be seen, each of these specification presents challenges. Read-out rates for high-pixel-count cameras are typically well below 25 frames per second (fps), limited primarily by the USB 2.0 connection. Limitations on pixel-count also limit available field of view, driving up the number of images required to match the examined smear area. And, perhaps most critically, LED illumination, necessary for a portable, battery-powered device, was insufficient for good imaging when we started the project, requiring especially careful engineering.

Resolution:	0.76 $\mu\text{m}$
Excitation intensity at sample:	50-75 mW / $\text{mm}^2$
Examined smear area:	18 $\text{mm}^2$
Frame rate	$\geq 25$ Hz
Integration time	$\leq 40$ ms

Table 3.1: **Ballpark initial optical requirements.** Based on assumptions of 25% camera QE, excitation light centered at 455 nm,  $M \sim 14$ -16 from sample to detector.

## 3.2 Camera

The digital camera is in many ways the center of our portable system, enabling acquisition of images which can easily be processed, displayed, and transmitted. It is critical also to image quality, both in terms of spatial imaging and, by way of its quantum efficiency, to detection of the sample light in the first place. I placed stringent requirements on the camera: it needed to be low-cost, high-pixel-count, sensitive (high QE), supportable (i.e., a sensor that was known, widely used, available on board-level implementations), and must be used in a cellphone from a major manufacturer, assuring that low-cost supplies would be available if we reached a point to scale production of the diagnostic devices and drive down per-unit costs.

At the time I began this project, the transition from CCD (charge-coupled device) image sensors to CMOS (complementary metal-oxide-semiconductor) sensors was incomplete, and though it seemed inevitable that CMOS would triumph in low-cost applications due to its compatibility with standard chip-manufacturing processes, and is in principle capable of very good performance [49, 58, 55, 56], it was unclear how quickly this shift would occur. Furthermore, CMOS sensors had a terrible reputation for noise and poor specifications when it came to high-quality imaging; virtually all high-end scientific cameras for fluorescence imaging were still CCDs.

As a result, I did my initial prototyping around a CCD sensor, the Lumenera lw230, a 4.4  $\mu\text{m}$  pixel-pitch, 2 Mpixel sensor: the largest affordable ( $< \$1\text{k}$  for a board camera with driver software, in quantity 1; however, costs drop rapidly as one moves to volume production) format at the time.

Since camera chips are digital sampling devices, it is worth pausing to recap requirements the Nyquist criterion places on the sampling of the image. As noted in the discussion surrounding Equations 3.4 and 3.5, an optical system is essentially a low-pass filter [41], and the sample-plane-referenced (i.e., adjusted for magnification) requirement on the spacing of digital samples is:

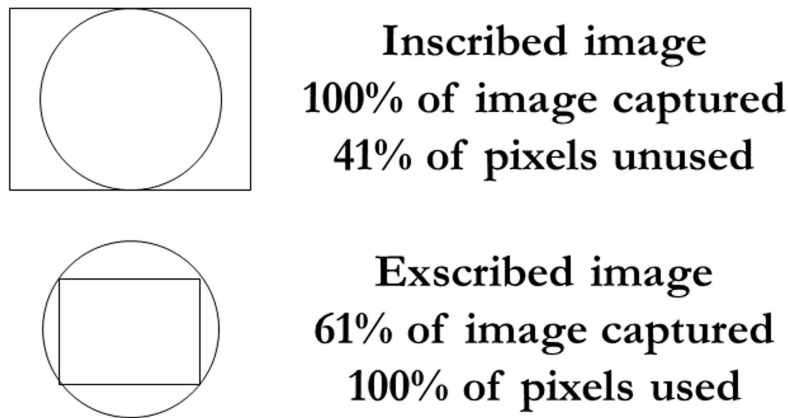


Figure 3.1: **Inscribed and exscribed sensor geometries.** Assumption is that sensor is a standard 4:3 aspect ratio; circular area is extent of optical image at the detector. Advent of widescreen (16:9) and other aspect ratios complicates the situation and is less efficient for imaging circular fields of view.

$$d_{\min} = \text{Minimum sample-referenced pixel spacing} = \frac{\lambda}{4 \text{ NA}_{\text{Obj}}}. \quad (3.7)$$

In practical terms it is often useful to sample at a slightly higher frequency (closer spacing), since the finite width of pixels serves to further average the samples, as does leakage of charge between pixels, etc [6]. Of course, exceeding the sampling requirements by too much unnecessarily reduces the size of the field that can be imaged. The situation is further complicated for color sensors, where the Bayer array [49] results in the pixel spacing being effectively doubled for the red and blue pixels, and increased by  $\sqrt{2}$  for the green.

Sampling at or above Nyquist is critical for this diagnostic application, since I intended (and we now do) interpolate and zoom the images to magnifications of  $\sim 3500X$  for evaluation by human users<sup>2</sup>, and because we need to do robust feature extraction from the images in order to implement an accurate *tuberculosis* ID algorithm (c.f. Chapter 5). Aliasing and pixelation artifacts would not be acceptable.

It is useful to get an idea of how many pixels are required to image in green light ( $\lambda = 500$  nm) with a 0.4NA objective that has a 0.9 mm diameter (18 mm FN / 20X objective) field of view. There are two clean ways to fit the image onto the sensor: inscribed and exscribed, as shown in Figure 3.1:

<sup>2</sup>Since the laptop screen is typically  $\sim 25$  cm from the user, the effective magnification becomes the size of the interpolated bacillus on the screen divided by its actual size of  $\sim 2 \mu\text{m}$  long. It is not uncommon for us to blow the images up, with interpolation, such that bacilli are  $> 5$  mm long, for an effective  $M > 2500X$ .

With pixel spacing given by Equation 3.7, one can calculate the number of pixels a 4:3 aspect ratio sensor must have for both cases; it turns out to be 11 Mpixels for the inscribed case and 4 Mpixels for the exscribed case. Although 16 Mpixel sensors are now becoming available [104], at the time I began this project, 2 Mpixels was considered a lot. After I built my initial prototype but before the subsequent design was frozen for manufacture with our outside firm, the 5 Mpixel CMOS sensor [114] used in the Nokia N95 cellphone [72] became available in a board-level module. Since sampling requirements dictate that it is pixel count, not physical sensor size that determines the area one can image without aliasing, the larger pixel count allowed us to increase our field of view by 2.5X over the original 2 Mpixel CCD sensor, though at some cost in optical complexity as described earlier.

This sensor has a  $2.2 \mu\text{m}$  pixel spacing, yielding a required Nyquist magnification of 7.49 for 470 nm light, the shortest wavelength that passes the emission filter. As noted, it makes sense to oversample at least slightly, so we settled on a magnification of 8.845 as convenient in terms of commercially available parts and allowing for a reasonable 18% oversampling. While the oversampling results in some loss of imaged field it does result in us placing an image on the entire sensor, and the lack of blank areas has advantages in terms of simplicity during later presentation to the user. We capture 49% of an FN 18 objective FoV.

Because CMOS sensors were relatively new for scientific purposes, and since the use of low-cost sensors meant many specifications were not available in the data sheets, I did a full analysis of both the original CCD sensor and the newer Aptina / Micron CMOS sensor (implemented in the Lumenera lw575m camera module). The proper way to evaluate digital sensors is via use of photon-transfer techniques. A full description of these is beyond the scope of this thesis, but covered very nicely in Janesick's excellent book [57]. In short, one exposes the sensor to sufficiently uniform light (more uniform than the bit depth, so in my case  $< 0.1\%$  variation over the interrogated area of  $100 \times 100$  pixels, or  $0.44 \times 0.44$  mm for the lw230; less for the lw575m camera), and then takes pairs of images at increasing exposure levels<sup>3</sup>. The differenced image pairs contain only noise terms, and from the raw exposure data and the noise terms, as well as the known behavior of photon shot noise one can extract various camera parameters of interest using, e.g., MATLAB. This data is shown in Table 3.2 along with some other useful information on the camera modules.

It is worth pointing out that there are different definitions of dynamic range. The industry appears to use  $\text{dynamic range} = 20 \log_{10}(\text{FWC} / \text{read noise})$ , which I conform to in the table despite the fact that the measurement is arguably a power measurement and so should not use the factor of two. Furthermore, many camera specification sheets cite a different number based on the fact that when the pixel well contains many electrons, the dominant noise source is photon statistical ("shot") noise, which scales as the square root of the number of photons (or photoelectrons). This is a useful way of assessing likely performance, and by that measure the lw230 has only 38.6 dB dynamic range and the lw575m 37.5dB, lower because it has a smaller full well capacity (FWC). This last points to a problem with the

---

<sup>3</sup>I actually used a pulsed LED source instead for additional precision and to keep other camera parameters constant.

	MT9P031 sens.		
Lumenera cameras:	lw1570m (CMOS)	lw230m (CCD)	Units
Dark signal	34	29	e- / s
Dark current, 20 degC	111	24	pA / cm <sup>2</sup>
Read noise	6.3	5.3	e-
Fixed Pattern Noise, Pn	0.39%	0.18%	%
Dynamic range	9.8	9.4	bits
Dynamic range	59.1	56.5 - 60	dB
Full Well Capacity	5600	7300	e-
Dark signal, 20 degC	0.6%	0.4%	%FWC / s
ADC quantization noise limited?	at < 10 bit	at < 11 - 12 bit	
Dark Fixed Pattern Noise, Dn	0.6	0.1	
Quantum Efficiency	46%	41%	QE
Power use, USB off	0.15	0.15	mW
Power use, USB on, no imaging	1.40	1.55	mW
Power use, max full frame rate	1.55	1.90	mW
Noise floor, 500 ms exposure	18	16	photons
e- / DN (ADC rate)	0.089	0.17	e- / DN

Table 3.2: **CMOS and CCD camera performance data.** Measurements match available specifications well. Note relatively high QE values; CMOS camera has lower power consumption despite higher pixel count, but significantly worse noise and dark current figures. Dynamic range is calculated using camera noise figures, not photon noise (see text); ADC rate calculated for 16-bit readout mode.

steady pursuit of higher pixel counts on small pieces of silicon: as the pixel spacing goes down, so does the pixel area, which is somewhat proportional to the FWC. Smaller pixels thus tend to have lower effective dynamic range.

Some other aspects of the CMOS vs. CCD sensor comparison are worth mention, particularly the differences in dark signal, fixed pattern noise (FPN), and dark signal fixed pattern noise. The CMOS sensor has 50% higher dark signal, which leads to higher background in long exposures, though this is not a significant issue for us in practice. Since the absolute magnitude of the Dark FPN is proportional to the dark signal itself, it is not a major issue either despite being 6X larger for the CMOS sensor. The FPN, however, is slightly over 2X higher for the CMOS sensor (notably all of these issues serve to confirm the poor reputation CMOS has for accuracy), and since one seeks to significantly fill pixels in an image in order to fully use the dynamic range of the camera, the FPN will matter more. For example, a filled lw575m pixel will have 5600 e-, 6 e- of read noise,  $0.4\% \cdot 5600 = 22$  e- of FPN (as measured over many pixels), and an RMS variation of 75 e- ( $= \sqrt{5600}$ ) due to photon shot noise. Consequently the FPN is much larger than the read noise and closing in on the photon noise in terms of magnitude. Conveniently FPN, since it stems from pixel photo-response nonuniformities (and is sometimes called PRN for that reason), it can be normalized out by dividing by a “flat frame” during postprocessing. We have not implemented this, but being computationally simple and fast, it is a logical thing to do if pursuing the project toward larger deployment. A final note on the sensors: both have surprisingly good quantum efficiency (QE) — 41-46%, which per published specifications [114] remains quite high over the entire Auramine O emission range. These fairly high QEs have recently been further eclipsed by the advent of low-cost commercial back-thinned CMOS sensors (with color arrays, no less) [104], which should have QE figures above 70%. That will translate directly into faster fluorescence imaging, or, in the case of color sensors, allow use of a color sensor (in which only 50% of the pixels will be green, the wavelength of the Auramine O emission) without major loss of imaging sensitivity compared to the current device.

The primary factors in my decision to move to CMOS sensors were the higher available pixel count in low-cost cameras, enabling larger field of view and thus ease of use or diagnostic sensitivity, and the fact that we wanted to design a system where developments in consumer technology would result in additional cost reductions. Since the industry is decisively moving to CMOS, and performance is already close to that of CCDs in the same price range (as shown by Table 3.2), there was no reason to hold back. An additional, though lesser based on similarity of my power measurements in the table, consideration is that CMOS sensors tend to be vastly more power efficient, due to their lower-voltage operation and more efficient pixel readout scheme [49]. In practice, the board camera modules I obtained seemed to have power dissipation matched to what was available over the connection; most likely this is not out of necessity, and in a high-volume application where it makes sense to design one’s own boards, CMOS is likely to result in power savings leading to increased battery life, lower charging requirements, or reduction in size as less battery is required for a given performance level.

Before choosing a camera for a redesign, it makes sense to measure the parameters in

Table 3.2; almost all derive from the same photon transfer measurements, so effort does not scale with number of parameters derived). If any specifications are vastly worse than in our system, care should be exercised. Special attention should be paid if FWC drops significantly, as that will adversely affect image bit depth and signal-to-noise. As part of the same procedure, FPN and dark current also make sense to measure for every pixel, so that average dark signal and photoresponse nonuniformities can be corrected for prior to subsequent processing; if this is not done, then a low intrinsic FPN is especially important.

The last major camera specification of design import for a portable device like ours is the maximum frame rate. This is uniformly dominated by the bandwidth of the connection to the laptop or external device; higher frame rates are typically possible when fully implementing one's own board-level solution. Unfortunately, that requires substantial expertise and resources. Using commercial board-level cameras for prototyping has the advantage of a supported hardware system so that multiyear projects can be pursued without critical parts becoming unavailable, and of drivers and control software being available from the vendors. However, the camera must then be connected to the controlling device, and the current standard, USB 2.0, has a nominal bandwidth of only 480 Mbits / s. To put this in context, a 5 Mpixel sensor with a bit depth of 8 bits requires  $\sim 40$  Mbits *per frame*...for a theoretical maximum of 16 frames per second (fps). In practice, USB 2.0 bandwidth rarely matches the peak specification, and there is communication protocol overhead as well. The 5 Mpixel lw575m reaches 6.0 fps reading out full-frame on a laptop with a dedicated (not split) USB 2.0 port, barely adequate for focusing when in full-frame mode (not zoomed in to a sub-region of interest, which since it has fewer pixels, allows faster frame rates). The advent of USB 3.0 with its much higher data rates promises to reduce this problem in the next couple of years.

### 3.3 Illumination Intensity

I had been aware from the start that LED power would be a limiting factor, which was one reason we pursued the early proof-of-concept test described in Chapter 2. Etendue limits (deriving from Liouville's theorem for phase-space conservation [48]) are the bane of high-intensity illumination of small areas using incoherent sources, a fact well known in the spectrometry community. Since Etendue considerations can place upper limits on the coupling achievable between, e.g., an LED and a sample, they are a good place to start an illumination design process.

## Illumination intensity

### Etendue considerations

The most general formulation of the Etendue is purely geometric, derives from Liouville's Theorem, and states that [126]

$$n^2 dx dy \cos(\theta) \cos(\phi) = \text{constant}, \quad (3.8)$$

where  $n$  is the refractive index and  $\theta$  and  $\phi$  are the angles with respect to the normal to the  $x, y$  coordinate system.

In an axially symmetric system, this can be rewritten as

$$\text{Etendue} = \xi = \iint n^2 \cos(\theta) dA d\Omega \quad (3.9)$$

where  $\theta$  is the angle with respect to the optic axis,  $A$  is the area of the object, defined normal to the optic axis, and  $\Omega$  is the solid angle. Many texts further assume the small angle approximation, with  $\cos(\theta) \sim 1$ , reducing this further to

$$\xi = n^2 \cdot A_{\text{Sample}} \cdot \Omega_{\text{Sample}}. \quad (3.10)$$

In addition, the assumption is also often made [48] that  $n = 1$ , resulting in the Etendue being referred to as the “ $A\Omega$ ” product.

The difficulty with this is that the true definition, Equation 3.8, assumes that the original surface in question was a perfectly diffuse (“Lambertian”) emitter, which has uniform brightness at any angle, or, since the apparent surface size scales with the cosine of the angle, also has radiant intensity proportional to the cosine of the angle. One case where this must be treated with care is fluorescence emission from a dilute solution, where emission power (not brightness) is isotropic.

As a result, at larger angles when one cannot assume  $\cos(\theta) \sim 1$ , the “ $A\Omega$ ” product is erroneous if one simply takes the solid angle  $\Omega$ . Rather, one must use the integrated solid angle incorporating the  $\cos(\theta)$  term. For our purposes, it suffices to note that an LED emitting into a half-space will *not* have a product  $A\Omega = A 2\pi$  as might be expected, but rather will have

$$\begin{aligned} A\Omega_{\text{Lambertian}} &= A \iint_{\text{Half Space}} \cos(\theta) d\Omega \\ &= A \pi. \end{aligned} \quad (3.11)$$

LEDs surfaces also do not emit into air, as might be expected; rather, an acrylic cap is typically used on top of the LED die to increase the total internal reflection (TIR) angle for the photons exiting the silicon, thus decreasing reflection losses in output coupling and

increasing power output. This acrylic has an index of  $n \approx 1.49$ , which also appears in the full Etendue expression.

It is also worth noting that LED angular emission profiles can vary, usually in so-called Lambertian and Batwing profiles. Batwing profiles load power preferentially into high emission angles, which has advantages for some applications but potentially complicates efforts to achieve uniform illumination in a microscope system. Lambertian emission is defined as emission where the radiated power is proportional to the cosine of the angle from the surface normal; this is the condition of uniform brightness, where the ratio of the power to the projected size of the emitting surface is constant with angle, and is typical of perfectly diffusely emitting objects. LED emission is not inherently exactly Lambertian, and engineering effort is expended making them roughly so for optical use, as is also the case with the Batwing emission profile. For purposes of rough calculation, it makes sense to start with the Lambertian emission pattern that matches the simple calculation in Equation 3.11; it also turns that the Lambertian LED pattern provides the best CAD-modeled illumination uniformity.

For cases where angles are smaller, and one can assume  $\cos(\theta) \sim 1$ , the integral as in Equation 3.11 can be simplified to calculation of the solid angle subtended by the emitted light, which, in the case of emission into a cone of half-angle  $\theta$  (the same  $\theta$  as used to calculate the NA, or conversely derivable from a known NA) is simply

$$\begin{aligned}\Omega &= 4 \pi \sin^2 \left[ \arcsin \left[ \frac{\theta}{2} \right] \right] \\ &\approx \pi \text{NA}^2\end{aligned}\tag{3.12}$$

All of this can be combined to calculate the Etendue (sometimes called Throughput) of an optical system; Etendue can be reduced but never increased [73], so the ratio of the initial to final Etendue of a system (set equal to unity if the ratio  $> 1$ ) gives a theoretical maximum achievable efficiency:

$$\text{Etendue Efficiency} \approx \frac{n_{\text{air}}^2 \cdot A_{\text{Sample}} \cdot \Omega_{\text{Sample}}}{n_{\text{acrylic}}^2 \cdot A_{\text{LED}} \cdot \Omega_{\text{LED}}}\tag{3.13}$$

Using the values of  $1 \text{ mm}^2$  for the LED die size (emitting area),  $1 \text{ mm}$  dia. for the sample area illuminated (i.e., an area of  $\pi / 4 \text{ mm}^2$ ),  $n = 1$  (air) for the sample medium, using the results of Equation 3.11 in place of the short-hand  $\Omega_{\text{LED}}$  and replacing  $\Omega_{\text{Sample}}$  with the NA-based estimate in Equation 3.12, this results in

$$\begin{aligned}\text{MaximumEfficiency} &\approx \frac{\Omega_{\text{Sample}}}{9} \\ &\approx \frac{\text{NA}^2}{3}.\end{aligned}\tag{3.14}$$

A good rough estimate for the maximum NA of a single, and thus low-cost, lens is given by using the lensmaker's equation

$$\frac{1}{f} = (n - 1) \left[ \frac{1}{R_1} - \frac{1}{R_2} \right]. \quad (3.15)$$

Since for most glass  $n \sim 1.5$ , and the lens becomes a sphere, and  $f = R$ , when the radii of curvature  $R_1 = -R_2 =$  the lens radius. In that limiting case,  $f =$  lens radius, or NA 0.7. Using this value in Equation 3.14, the maximum possible efficiency becomes  $\sim 16\%$ .

Since a good high-power LED (e.g. the royal blue Philips LumiLEDs Luxeon III) at the time produced about 340 mW [75] from a 1.2 mm x 1.2 mm die (the larger die area reducing Etendue efficiency by a factor of 1.4X), this efficiency estimate suggests that the maximum achievable intensity would be in the neighborhood of 50 mW / mm<sup>2</sup> for a 1 mm dia. illuminated area just at the low end of acceptable given my earlier estimate in Table 3.1.

## Optical Layout

The efficiency calculation in Equation 3.13 has import for the optical layout as well as straight intensity estimation. Traditional conventional wisdom is that epi-illumination (i.e., illumination of the sample through the same objective which collects the light from the sample for the image) is always best for fluorescence microscopy. The rationale for this is that in an epi-illumination geometry, the bulk of the excitation power is directed away from the imaging system, with only reflections incident on the fluorescence excitation-blocking (aka emission) filters, thus reducing leakage and background of the powerful excitation light into the weak fluorescence image. Especially in the past, when the performance of optical filters could be quite poor compared to what is now possible, this was a critical consideration. For instance, one can now buy COTS filters (e.g. from Chroma Corp.) which block to OD8, i.e., to a part in 10<sup>8</sup>, and have transitions from blocking to transmission over only a few nm; conversely, Schott glass filters, as used before the advent of modern interference filters, have lower peak transmissions and vastly wider transitions which are much wider than the Stokes shift (distance between excitation and emission maxima) of most dyes. As a result, even OD5 blocking using absorbing-glass-type filters is unusual. An epi-illumination geometry results in something on the order of  $> 4\%$  of the excitation light being reflected from the objective lens surfaces and coverslip, and the (expensive  $\sim$ \$150) dichroic interference filter used to couple the light into the optical path is typically OD1-1.5, it being much harder to achieve good blocking at non-normal incidence, with the final result that illumination power incident on the subsequent so-called "emission" filter is reduced by  $\sim$  OD2-3 compared to a transillumination geometry where all excitation light is incident on the collection-side optics (as shown in Figure 3.2). As a result, an OD5 absorbing glass filter arrangement used in an epi-geometry can provide  $\sim$  OD7-8 blocking. Notably, however, this is the same as is now possible simply using a good modern interference filter.

The incident excitation light intensity and fluorophores properties determine the rate at which photons are emitted from a given dye molecule, and image background depends on

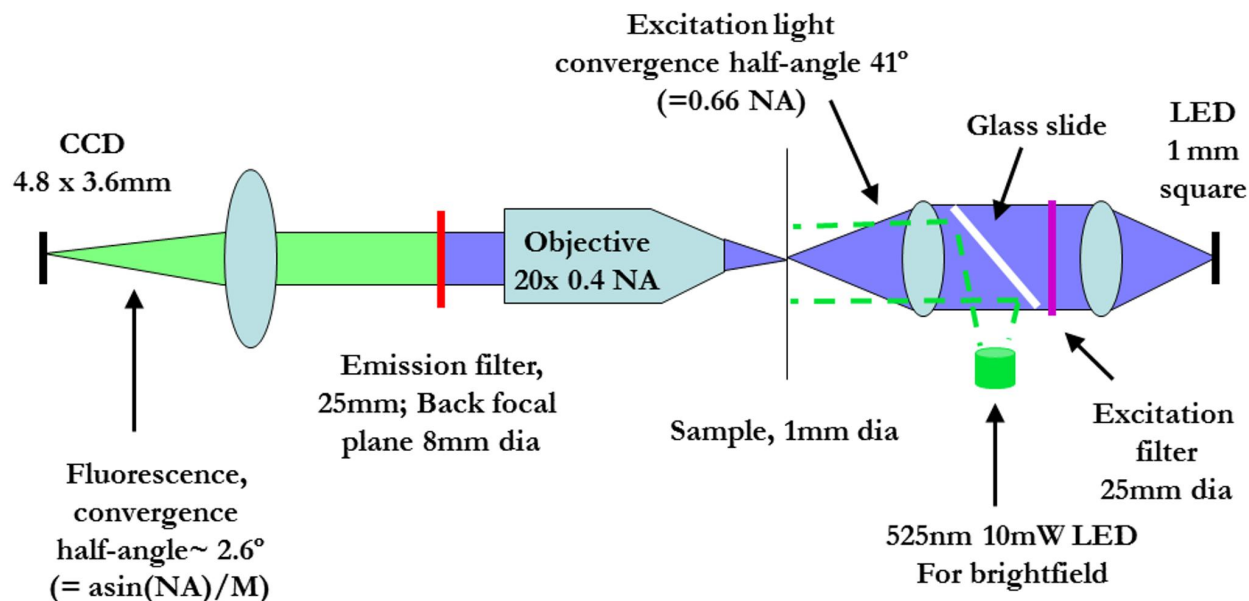


Figure 3.2: **Optical Train.** Device optical train; note transillumination geometry, used to increase excitation intensity and reduce cost; this geometry is possible because of the inherently good signal-to-background ratio provided by the highly-labeled bacilli. Kohler illumination is not necessary due to source uniformity and careful design, as discussed in the text.

that same incident intensity and the filter leakage. In cases where one is imaging single fluorophores, maximum blocking is thus necessary, and an epi- geometry is used to enhance this. Tuberculosis AFB, however, label with a great many fluorophores, and so the signal-to-background (S/B) ratio is significantly enhanced. In the case of *M. Tuberculosis*, Auramine O has been suggested to bind to the nucleic acids in a nonspecific way [45], and DNA has about 4 million basepairs. If dye binding to the DNA is in even a weak stoichiometric ratio (say, 1 part in  $10^5$ ), and neglecting potential RNA contributions which would increase the concentration of bound dye, this presents a vastly different S/B situation than single-fluorophore imaging, and weakens the requirement in our case for maximum excitation blocking from the collection optics, especially since modern filters provide performance equivalent to older epi- geometry systems.

Returning to Equation 3.13, the system efficiency is limited in the end by  $\Omega_{\text{Sample}}$ , or, equivalently, the sample-side NA of the condenser lens. This limitation will be true as long as the limiting  $\Omega$  is on the condenser (sample) side; if one is using a high-NA microscope objective (e.g. a 1.4NA oil-immersion type), then the limiting NA will be on the collector (LED) side<sup>4</sup>. Since low-cost 0.67NA collector (LED-side) lenses can be obtained for \$16 each,

<sup>4</sup>Beware: naively inserting a lower  $\Omega_{\text{LED}}$  in Equation 3.13 will result in an incorrect estimate; while the calculated efficiency will go up, that efficiency will be based on the already much smaller amount of

the transition from being limited by the objective occurs at NA 0.67. Since I wished to design the system around a low-NA (and thus low-cost) objective, and since low-NA objectives typically have much larger fields of view (increasing the smear area examined per image, and thus diagnostic sensitivity and/or number of images required), it is useful to examine the tradeoff that using, e.g., the 0.4NA (20X) objective typically used for fluorescence smear microscopy in epi- and trans-illumination geometries would present.

An estimate of the difference can be had by using Equation 3.14. Since the maximum efficiency scales with  $NA^2$ , the relative loss of delivered power will be  $(0.67 / 0.4)^2 = 2.8X$  using the 0.4NA objective to deliver light to the sample. This result turns out to be exact, not approximate, once one takes into account the obliquity factor.

Consequently there is a powerful argument — 3X higher excitation intensity at the sample — to be made for using a transillumination geometry when using a low-NA objective and power is potentially an issue. This argument is enhanced if signal-to-background is expected to be fairly good, and provides the added advantage of allowing elimination of a \$150 dichroic filter, not insignificant when trying to design for a total system cost of  $\leq$  \$1,500. As a result, I decided on the transillumination geometry shown in Figure 3.2.

Illumination engineering is, due to its complexity, nearly a field unto itself in optics, especially when a small area needs to be illuminated at good uniformity. Because we knew that we would be illumination-intensity limited, based both on the estimate above and the weakness of our signal in the proof-of-concept experiment (Chapter 2, and also because good uniformity would be critical to avoid apparent vignetting of the fluorescence image at the edges of the field, I arranged to work with Optical Research Associates (ORA, now SynopSys) to provide advice and to do a trade study (i.e., a study of the trade-offs involved in different design decisions) using tools and knowledge unavailable to us, namely the optical CAD programs Code V and LightTools incorporating industry-typical tolerancing. ORA's expertise and work, as done by John Rogers and Tobias Schmid, were extremely helpful, and the working relationship excellent.

Results of their modeling of a low-cost condenser system for the LED is shown in Figure 3.3. In short, with a pair of custom aspheric lenses (which would be extremely expensive) it would be possible to achieve 91% of the (Etendue-limited) theoretical maximum; shifting to \$32 worth of commercial off-the-shelf (COTS) 0.67NA lenses from CVI / Melles-Griot results in only 67% of the theoretical maximum, or 10.4% absolute efficiency, while better matching the low-cost intent of the device. ORA also investigated use of plastic non-imaging concentrators (e.g. fiber couplers) for us, which have the advantage of extremely low cost ( $\sim$  \$8.50 per unit), but maximum efficiencies and uniformities were no better (8.1% efficiency and  $\sim$  6% uniformity in one model) and there were questions about autofluorescence of the plastic which would be seriously problematic in a fluorescence application.

Based partly on these results, I designed the system using the Melles-Griot lenses. During the course of the project, newer LEDs became available — as of the last device build date,

---

light collected from the LED by the lower NA optics. True power collection from the LED will actually be reduced.

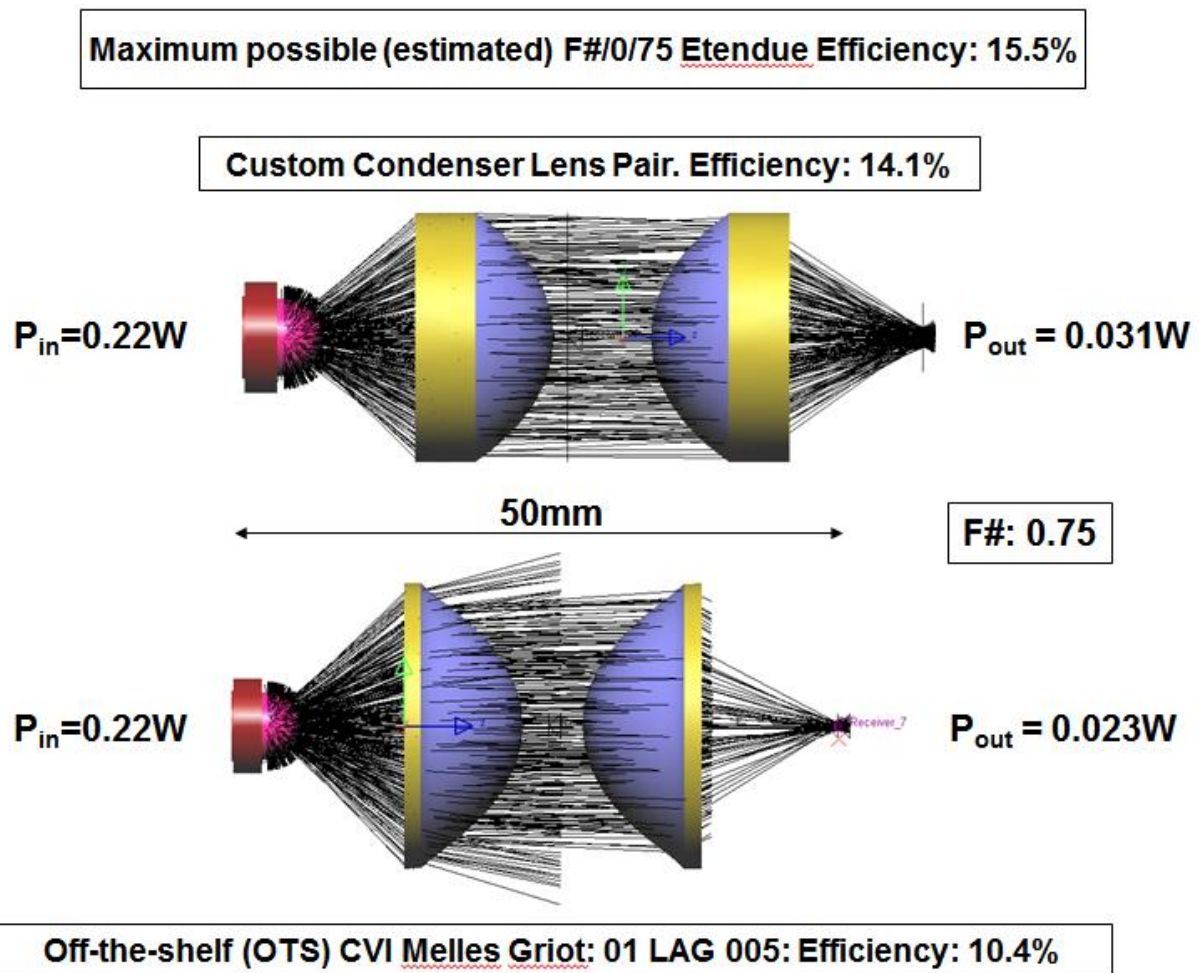


Figure 3.3: **Condenser efficiency.** Comparison of different collector / condenser systems. Maximum efficiency shown is 15.5% based on the more commercially achievable 0.67 NA ( $f/0.75$ ) of the CVI lenses rather than the 0.7 NA used in the text. LED is on the left; rays which terminate before the sample do not reach the defined sample area. Courtesy ORA / John Rogers and Tobias Schmid.

Philips royal blue Rebel LEDs had 1 mm<sup>2</sup> area and could produce outputs of 900 mW centered at 440-445 nm if bought in sufficient quantity to be able to specify production binning (values are for bins K,3) [74]. This power allows for coupling efficiency of 90 mW to the sample, well above what I calculated as necessary in Table 3.1, though notably not so high that the loss of 2.8X intensity due to use of an epi-illumination geometry would be acceptable. Furthermore, the lower center wavelength bin would guarantee a better match to the Auramine O dye absorption, additionally enhancing fluorescence output from the sample. In our (small-quantity) case, we used unbinned LEDs, whose wavelengths nonetheless proved acceptable (c.f. Figure 3.7).

### 3.4 Illumination Uniformity

Since fluorescence emission is proportional to illumination intensity, variations in illumination will translate directly to the image. This presents special problems in low-cost digital imaging because low-cost cameras also have low bit depth — typically 8 bits, or 256 grey levels. As a result, a variation in 50% of illumination across the field of view implies that, assuming no bacilli are saturating the detector, some AFB will be imaged with only 64 grey levels. In fact, there is also substantial natural variation in the apparent brightness of AFB, presumably due to variations in staining efficiency, as well as variations in collection efficiency by the objective at different points in the field; illumination variations multiply with these to determine the final image. Much like a stereo system, where one cannot get great sound solely by getting a better CD player, amplifier, or speakers, but must optimize all three, good fluorescence imaging uniformity requires uniform illumination, collection, and staining. The latter, of course, is out of the control of the hardware designer, but both illumination and collection uniformity must be separately optimized.

The usual way to achieve good illumination uniformity in microscopy is to use Kohler illumination [79], which images the (often nonuniform) illumination source into a Fourier-plane to the sample, resulting in homogenization of the illumination at the sample. This is in contrast to so-called Critical illumination, in which the illumination source is imaged directly onto the sample, and any nonuniformities in the source are thus directly present in the image. The two approaches are otherwise equivalent, e.g. in terms of optical power throughput and illumination coherence [79, 7]. It is however easier to implement Critical illumination in a short track length, and so I preferred it for my design, where I was striving for a very compact device to enhance portability.

Achieving better than 10% uniformity via any technique (including Kohler) is considered to be an extremely difficult optical engineering problem, especially if it is necessary to maintain high power-coupling efficiency (diffusers by definition disperse power over large angles, effectively creating Etendue limitations; it is precisely this that the Kohler approach to assuring illumination uniformity is designed to circumvent). In our case, the LED die is a far more uniform emitter than the tungsten filaments in the lamps Kohler was first used with, and is larger than the field of view of the objective we use, making it reasonable that

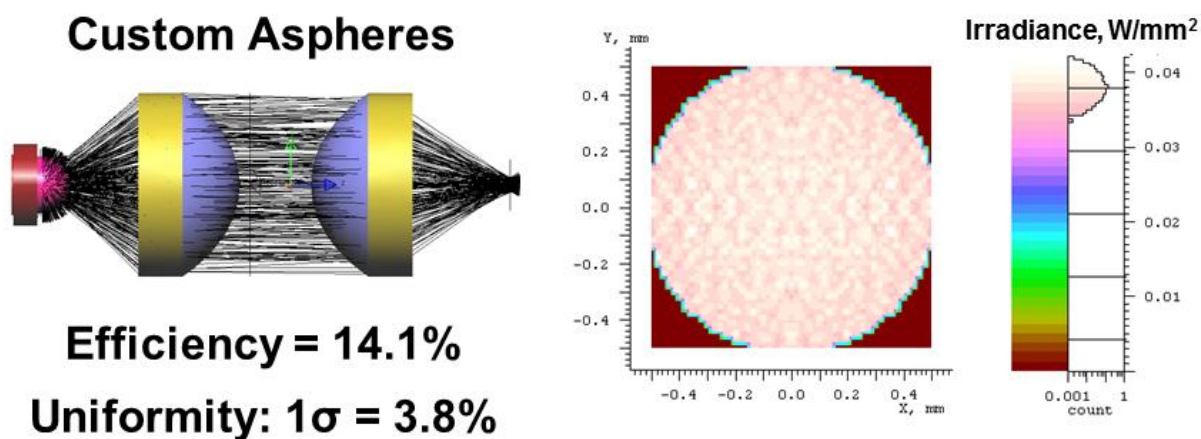


Figure 3.4: **Calculated illumination uniformity.** Nonuniformity is expected to be  $\sim 4\%$  without tolerancing errors or collection optics effects. This correlates well with our measured  $6\%$  value over 15 units. Both figures are quite good; use of Kohler illumination is demonstrably unnecessary.

it might be acceptable. Because uniformity is so important in our application, I nonetheless addressed the question of using Critical illumination in conjunction with an LED source with ORA. Their calculations showed that expected uniformity (not including design tolerancing) would be in the neighborhood of  $4\%$ , as shown in Figure 3.4, adequate for our application and thus allowing use of a Critical illumination geometry.

Given tolerancing issues not present in the calculation, this corresponds well with measurements I did on 15 manufactured units, which showed uniformity of  $6.9\% \pm 2.4\%$ , determined as  $[(\max - \min)/\text{average}] \pm \sigma$ , from measurements of illumination leakage in the field of view center and corners.<sup>5</sup>

### 3.5 Optical Filters

Frame rate intersects with image brightness in that ideally one wants to adequately expose the camera so that one can make best use of the camera dynamic range to get a low-noise image with maximum use of the available grey levels (bit depth). If an exposure longer than  $40$  ms is required to get such an exposure then one must trade-off between imaging rate (video rate of  $25$  fps corresponding to  $40$  ms exposures) and image quality. The current device design allows brightly stained smears to be imaged in  $\sim 60+$  ms, and requires up to  $500$  ms exposures for imaging dim / faded smears. As a result, almost all of our focusing is done at lower exposures using on-chip electronic gain, which introduces noise and has

<sup>5</sup>Since there is no reason to expect leakage through a filter placed in the objective back focal plane to be nonuniform in the image plane, that leakage is a good measurement of the illumination uniformity at the sample.

demonstrably lower image quality. Final images for diagnosis and analysis are taken at zero gain and longer exposure, of regions which are already in focus. Even an increase in camera QE by a factor of  $2X$ , to its theoretical maximum, will not resolve this issue fully; the only path is to acquire more light.

The total emission detected by the sensor from a sub-resolution fluorescent portion of the sample is given by the following relation:

$$\text{Emission} = \int \text{Excitation} \cdot \text{Dye}_{\text{emission}}(\lambda) \cdot T_{\text{Em filter}}(\lambda) \cdot \text{QE}_{\text{camera}}(\lambda) d\lambda \quad (3.16)$$

where I am omitting the number of dye molecules, since we have no way within the scope of this project of improving dye uptake beyond the current commercial protocol. The Excitation term here is constant within this integral, but is itself given by a separate integral:

$$\text{Excitation} = \int P_{\text{LED}}(\lambda) \cdot T_{\text{Ex filter}}(\lambda) \cdot \text{Dye}_{\text{absorption}}(\lambda) d\lambda \quad (3.17)$$

where I am omitting the dye absorption cross-section and quantum yield, which are constants out of our control if the dye is already specified (as in this case).

Without even identifying all the terms in the two equations, one can see that the Excitation and Emission terms will only be large if the various wavelength-dependent terms within them are large at the same time — if any term is small at a given wavelength, the entire integrand will be small for that wavelength. So the job becomes finding the best set of overlaps one can in order to maximize the detected sample brightness.

The terms in these two equations can be separated neatly into ones we can affect and ones we cannot: the dye emission and absorption  $\text{Dye}_{\text{emission}}(\lambda)$  and  $\text{Dye}_{\text{absorption}}(\lambda)$  are a given in our case, since we want to leverage existing supply chains, experience, and validation research. Furthermore, the  $\text{QE}(\lambda)$  curves for most low-cost commercial cameras are reasonably flat and fairly similar in the middle of the visible where Auramine O emission occurs. Lastly, in terms of  $P_{\text{LED}}(\lambda)$  there is a limited set of high-power LEDs to choose from; the Philips LumiLEDs Royal Blue Rebel centered at 445 nm is the best match by far to the 431 nm Auramine O absorption peak [92]<sup>6</sup>. This leaves the terms we can affect: the transmissions of the emission and excitation filters,  $T_{\text{Em filter}}(\lambda)$  and  $T_{\text{Ex filter}}(\lambda)$ .

Although it might at first seem that the filters can be chosen separately, since they appear separately in Equations 3.17 and 3.16, there is a major constraint: the transmission bands of the filters cannot overlap anywhere there is LED power and the camera is sensitive, or light from the LED will overwhelm the camera. Before covering details of the filter blocking, however, it makes sense to discuss the choice of transmission bands.

In order to achieve optimal blocking of the excitation, modern interference filters typical of fluorescence microscopy need to have  $\sim 10$  nm between the 50% transmission point (half max) of the falling edge to the excitation transmission band and the rising edge of the

---

<sup>6</sup>Very high-power and reasonably low-cost blue diode lasers have also become available at 445 nm recently, and bear investigation in the course of any redesign.

emission filter transmission band. Ideally one would like to keep this gap small since the Stokes shift of many fluorophores is on the same order, 10-20 nm, and so larger gaps require forgoing optimal match of the excitation filter to the illumination or the emission filter to the fluorescence. A natural way to find the optimum is to calculate the effective excitation and emission, since they contain parameters not easy to change; these are given by:

$$\text{Effective Excitation} = P_{\text{LED}}(\lambda) \cdot \text{Dye}_{\text{absorption}}(\lambda) \quad (3.18)$$

and

$$\text{Effective Emission} = \text{Dye}_{\text{emission}}(\lambda) \cdot \text{QE}_{\text{camera}}(\lambda) \quad (3.19)$$

One can then take a hypothetical set of filters, one short-pass and one long-pass, and while keeping the distance between the 50% points fixed, sweeping the wavelength location of the transitions and calculating for each value the total excitation, emission, and the product of the two (which is proportional to the brightness of the sample using those filter parameters). The results of this calculation using the Philips LED, Auramine O dye, and MT9P031 Aptina / Micron sensor are shown in Figure 3.5; the optimal transition is at 469 nm, at which point 93% of the obtainable emitted light is captured.

I chose the new filter set to match this as closely as COTS parts would allow; the new filters have excitation band 420–460 nm, and the emission filters have a 470 – 620 nm transmission band; the spectra are shown in Figure 3.6. The shift to new filters theoretically increased brightness by 196% and background by 38%; the decreased required exposure times justified the shift. However, because the new filters were implemented at the same time as other changes, it was not possible to verify the performance gain other than anecdotally.

A sense for the magnitude of blocking required is an important design consideration. Assuming that the excitation power at the sample is  $\sim 75$  mW at 450 nm, spread over a 1 mm<sup>2</sup> diameter area, the photon flux will be  $\sim 10^{23}$  photons / m<sup>2</sup> /s. The extinction coefficient of Auramine O is  $\epsilon \sim 25,000$  cm<sup>-1</sup> M<sup>-1</sup>, and the relation between cross-section and extinction coefficient is given by [102]

$$\sigma_{\text{cross section}} = 3.82 \cdot 10^{-25} \epsilon \quad (3.20)$$

where  $\sigma$  is in m<sup>2</sup>.

Assuming, as discussed earlier in the chapter, that on the order of 10<sup>5</sup> dye molecules bind to the bacillus DNA, one would expect

$$10^5 \text{ dye molecules} \cdot 10^{23} \text{ photons/m}^2/\text{s} \cdot 3.82 \cdot 10^{-25} \text{ m}^2/\text{cm}^{-1}/\text{M}^{-1} \cdot 25,000 \text{ cm}^{-1}\text{M}^{-1} = 10^8 \text{ photons/s} \quad (3.21)$$

from the bacillus. Of these, using Equation 3.22 for the collection efficiency, about 4% or  $4 \cdot 10^6$  photons / s will be collected by the objective and directed to the camera.<sup>7</sup>

<sup>7</sup>N.b.: this is in the right ballpark: given the calibration (magnification) in Table 3.8, the bacillus will get spread out over  $\sim 40$  pixels, each of which has a FWC of 5600 e-, for a total of 10<sup>5</sup> photoelectrons. QE of 45%, filter transmission of 90% and other reflection losses, and 200 ms typical exposure times easily bring the detected photon number into order-of-magnitude agreement with the emission number.

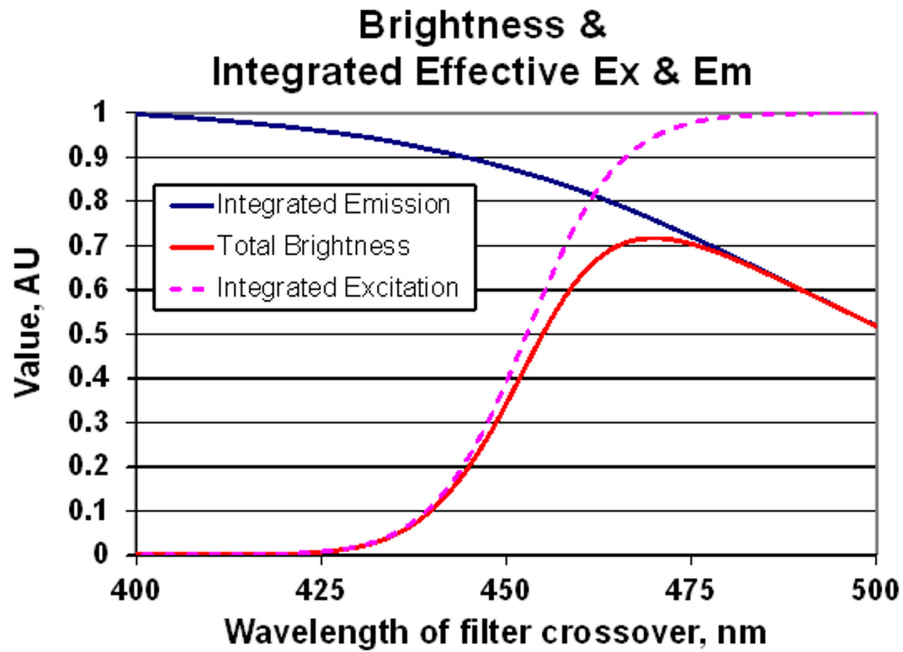


Figure 3.5: **Optimizing filter transition point.** As the transition moves from very short to very long wavelengths, effective excitation rises from 0 to 100%, while effective emission drops from 100 to 0%. Brightness is maximized when the product of the two, the effective excitation  $\cdot$  effective emission (red curve) is at a maximum; this occurs at 469 nm.

If a TB bacillus occupies about  $2 \mu\text{m}^2$  of effective area (blurred to  $\sim 1 \mu\text{m}$  in the transverse direction by the resolution of the optics, and  $\sim 2 \mu\text{m}$  long), then the number of excitation photons traversing that area, per second, will be  $\sim 2 \mu\text{m}^2 \cdot 10^{23} \text{ photons} / \text{m}^2 / \text{s} = 2 \cdot 10^{11} \text{ photons} / \text{s}$ .

In other words, in the area of the bacillus there will be about  $2 \cdot 10^{11} / 4 \cdot 10^6 \sim 10^5$  excitation photons for every emitted fluorescent photon. Given that the camera is 8-bit, I would like to have my background leakage from the excitation be *less* 1%, requiring that my filters block excitation by a factor of  $\sim 10^7$ , or using optical density terminology, OD7. Conveniently, this is exactly the standard blocking one can expect from modern interference filters such as the ET-series filters (Chroma Corp.) I use in the device, which block at  $\sim$  OD6, which is in keeping with the  $5.2\% \pm 1\%$  background figure we see over a 200 ms exposure. Unrinsed dye in the sputum smear is usually a larger effect than filter leakage, reinforcing my decision to use a transillumination geometry in order to increase illumination brightness and decrease exposure times.

An additional advantage of trans-illumination is that no dichroic mirror is required, saving  $\sim$  \$150, or  $\sim 10\%$  of the target high-quantity build price of the device. This begs the

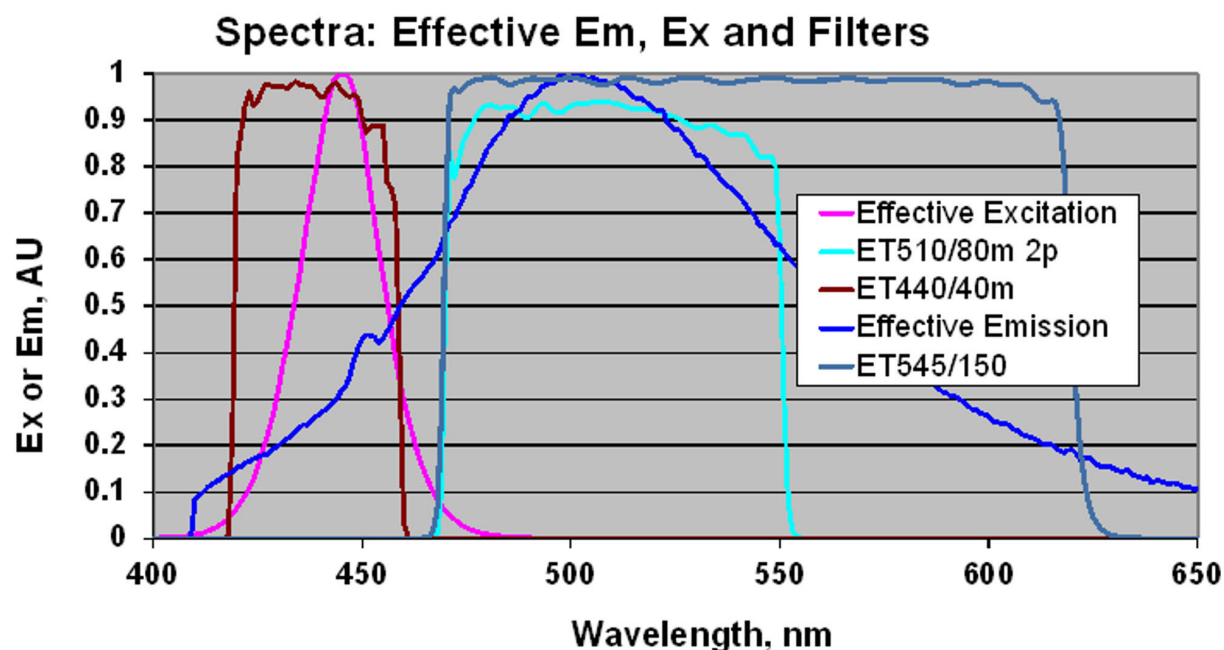


Figure 3.6: **Filter spectra.** Current fluorescence filter set transmission curves plotted against the effective excitation (LED spectrum  $\cdot$  Auramine absorption) and the effective emission (Auramine emission  $\cdot$  Camera QE).

question of whether the excitation filter itself is truly necessary, or whether it too could be dispensed with. This is particularly tempting since LEDs emit in a much narrower spectrum than arc lamps or halogen lights, suggesting that the natural drop-off may be sufficient to obviate the need for the excitation filter. Sadly this is not the case, as Figure 3.7 shows: the LED output has fallen only by a factor of  $10^2$  by 500 nm, already well into the emission filter transmission band and overlapping the fluorescence emission. As just shown, the LED would need to drop off by OD6, not OD2, to remove the need for an excitation filter, at least in the case of a sample with a dye labeling density characteristic of TB bacilli.

Although two filters are required, in quantity they need not be as expensive as it first appears: the emission filter can be placed in the 8 mm diameter objective back focal plane, giving it an area  $\sim 1/3$  that of a standard 25 mm filter. In volume price roughly scales with area (neglecting dicing costs), so this suggests the filter would cost in the neighborhood of \$10 to \$30 dollars. The excitation filter could similarly be placed near the sample, in a highly-converging ray space. This would require care, but the blue-shift in the transmission at higher incident angles would work in favor of continued good blocking performance, and the area that would need to be covered would be on the order of 2 mm diameter, or a 150X decrease in area and potential price, potentially bringing the filter down to the few dollar range.

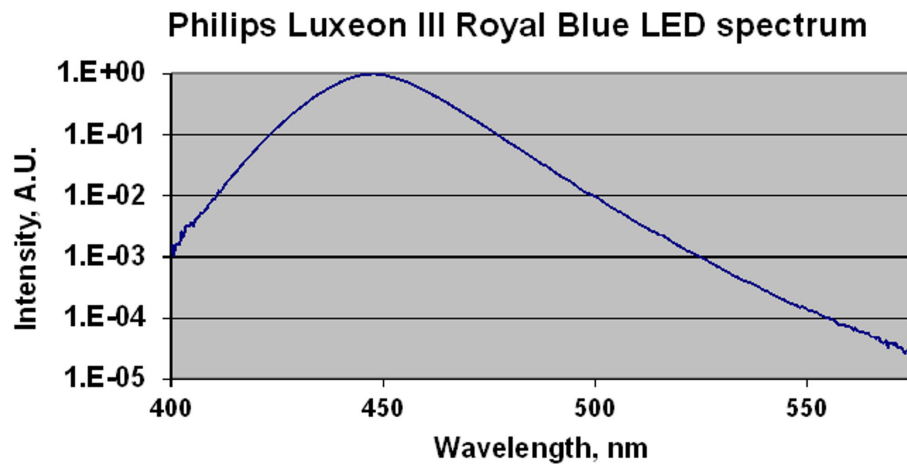


Figure 3.7: **LED spectrum.** Note substantial power in the red wing of the spectrum,  $> 10^{-2}$  of peak even at 500 nm. Consequently an emission filter is required.

## 3.6 Collection Optics

Naturally in an imaging application, the quality of the imaging (collection) optics is critical. In a fluorescence application there is, added to any resolution requirements, the issue of collecting adequate light. Several issues fall near the top of the list of considerations in a low-cost application:

- Collection efficiency
- Resolution (nominal and as-built)
- Depth of focus / field
- Field of view
- Working distance (an important consideration for the mechanical design)
- Aberrations (especially field curvature and astigmatism)
- Cost

Resolution, collection efficiency, and depth of focus depend theoretically on the collection angle and thus numerical aperture (NA) of the system, as given in Equation 3.1 and where

NA is defined as in Equation 3.2. The collection efficiency (CE) of an lens is given by

$$\begin{aligned} \text{Collection Efficiency} = \text{CE} &= \sin^2\left(\frac{\theta}{2}\right) \\ &\approx \frac{\text{NA}^2}{4} \end{aligned} \quad (3.22)$$

where  $\theta$  is the half angle of the collected light cone,  $n$  is assumed equal to 1, and the low-NA approximation for the CE is also given. For a 0.4 NA objective,  $\text{CE} = 4.2\%$ .

Lastly,

$$\begin{aligned} \text{Depth of Focus} = \text{DoF} &= \frac{\lambda}{4 n \sin^2\left[\frac{\theta}{2}\right]} \\ &= \frac{\lambda}{4 n \text{CE}} \\ &\approx \frac{n \lambda}{\text{NA}^2} \end{aligned} \quad (3.23)$$

where  $n$  is the index of refraction of the sample immersion medium and the DoF is defined as the full distance from just out of focus on one side of the sample to just out of focus on the other side; “just out of focus” is further defined as the point at which the Strehl ratio<sup>8</sup> is 0.8 [53, 7].

Clearly there is a direct tradeoff between the collection efficiency and depth of focus. The way this plays out for standard microscope objectives can be seen in the following table, created using the above equations:

The first thing to note from Table 3.3 is that while the collection efficiency (CE) of an objective rises rapidly with NA, the actual brightness changes little...since brightness is power per unit area, as the magnification  $M$  goes up, the image grows dimmer (like  $M^2$ , since  $M$  is a linear, not area, magnification), while as the collection efficiency rises the image grows brighter. For a camera sampling at Nyquist,  $M$  will be inversely proportional to the resolution and thus directly proportional to NA; from Equation 3.22 the CE is proportional to  $\text{NA}^2$ . The ratio is thus essentially constant until the NA grows high enough (e.g. by  $\text{NA} = 0.9$ ) that the low-NA approximation for the CE ceases to hold and CE grows faster than  $\text{NA}^2$ . Human users will perceive more variation, since the magnification chosen for the objective tends to follow standard round numbers, rather than changing in exact ratio the NA (or to the square root of the collection efficiency).

As a result, the rationale for choosing an objective of a given NA lies not in increasing brightness of the objects imaged, but rather primarily on required resolution, depth of field, and field of view, as well as specifications such as cost and working distance. There are

---

<sup>8</sup>The Strehl ratio is defined as the ratio of the peak measured or theoretical intensity from a point source to the theoretical maximum it could be for a perfectly focused, aberration-free system. It is thus always  $\leq 1$ .

Objective	Resolution	CE	DoF	FoV dia.	FoV area	Br.(H)	Br. (C)
10X 0.25 NA	1.22 $\mu\text{m}$	1.6%	7.9 $\mu\text{m}$	1.8 mm	2.5 mm <sup>2</sup>	1.5	0.97
20X 0.4 NA	0.76 $\mu\text{m}$	4.2%	3.0 $\mu\text{m}$	0.9 mm	0.64 mm <sup>2</sup>	1	1
40X 0.6 NA	0.51 $\mu\text{m}$	10%	1.3 $\mu\text{m}$	0.45 mm	0.16 mm <sup>2</sup>	0.60	1.1
63X 0.9 NA	0.34 $\mu\text{m}$	28%	0.44 $\mu\text{m}$	0.29 mm	0.064 mm <sup>2</sup>	0.68	1.33

Table 3.3: **Objective parameters.** Based on assumption of  $\lambda = 500$  nm. Field of View is calculated as discussed earlier in the chapter. Brightness figures are all relative to the 20X 0.4NA objective; (H) stands for human-eye perceived brightness, (C) stands for brightness on a camera sampling at Nyquist.

advantages to the larger (if equally bright on each pixel) image afforded by a higher-NA objective in terms of reduced sensitivity to noise in a given pixel (and noise is an especially large consideration in a low-cost commercial camera). There is also the possibility of using a higher NA lens in conjunction with an optical low-pass-filter (sometimes called an OLPF) which increases the point-spread of the system resulting in poorer resolution. In this case, one could design to have, e.g., the CE of a 0.9NA objective with the resolution of a 0.4NA objective, thus requiring less magnification. Resultant brightness could then be substantially increased over a that afforded by a 0.4NA objective alone; however, the higher-NA objective would be more expensive, an additional element (the OLPF) would be required, and in the case of commercial objectives, the field of view of the objective would be substantially lower as well.

Since use of 0.4NA objectives is already standard for *tuberculosis* diagnosis, we settled on that resolution as a required specification. By so doing, we guaranteed that trained technicians would be able to interpret images taken with the device, allowing for diagnosis and also for creating training image data for an automated bacillus identification algorithm. Furthermore, we could leverage the fact that the medical community is more likely to accept a device that conforms to existing standards. TB care is a massive international undertaking, and working in conjunction with the existing knowledge base and infrastructure is critical if one is to contribute.

## Custom versus commercial optics

Use of a 0.4NA system does not require use of commercial off-the-shelf (COTS) optics, and we were initially inclined to pursue a custom solution in the belief that technology developments and mass manufacturing, e.g. of injection-molded custom plastic aspheric lenses, could reduce system costs.

Because this required a level of industry familiarity and commercial optical design tools

and experience beyond what is available in almost any university, we also pursued this topic with ORA during our trade study. The custom asphere proved impractical on its face: design work would be  $\geq$  \$10k, diamond-turned custom plastic lens prototypes would be  $\sim$  \$2k - \$5k per surface, tooling cost for the asphere mold would be in the neighborhood of \$20k, and substantial production runs would be required by the producing company in order to keep the per-lens cost low, not including the non-recurring engineering (NRE) costs of the design, prototyping, and mold tooling. In short, we were told such a lens would not be cost effective unless we were envisioning order quantities of  $> 100,000$  pieces. This is a common theme: the sensors in camera-phones only cost a few dollars [104], primarily because they are initially purchased in quantities of millions. The sensor we settled on, in part because it is also used in the Nokia N95 cellphone, cost \$750 for small-quantity board modules with comprehensive control software. Larger-volume manufacture would naturally reduce these costs toward the limiting value of a few dollars, which is one reason we chose to use that camera; however, quantities of 100,000 were too hypothetical for it to make sense for us to commit tens of thousands of dollars in prototyping costs to plastic aspheres.

Beyond that, there is a critical difference between theoretical and as-built (including tolerances) system performance. We had ORA explore this for two cases, a custom collection system using glass lenses, and a semi-custom system consisting of a COTS objective coupled to custom tube lens system. The results are informative, and also have bearing on the molded-plastic asphere concept: once tolerances are taken into account, performance degrades remarkably, as shown in Table 3.4:

Field position	Pre-tolerance, $\mu\text{m}$	As-built, $\mu\text{m}$
Axis	0.95 $\mu\text{m}$	11.8 $\mu\text{m}$
0.35 mm radius	0.85 $\mu\text{m}$	11.8 $\mu\text{m}$
0.5 mm radius	0.80 $\mu\text{m}$	11.6 $\mu\text{m}$

Table 3.4: **Custom collection optics.** Values are 65% encircled energy radius values. System involves 3 lens groups, total track length of 120mm,  $M = 3$ , and collection  $\text{NA} = 0.4$ . As-built numbers reflect worst of 100 Monte Carlo cases assuming typical industry manufacturing and construction tolerances, with refocus to best image assumed for each instance. Courtesy ORA / John Rogers and Tobias Schmid.

Based on this, we also investigated use of a doublet tube lens (in this case to shift the magnification of a finite-conjugate \$100 price-range COTS objective); the optical layout is shown in Figure 3.8. It is important to note that better correction can be done if one has the prescription data for the objective, since then the additional optics can be chosen to compensate for aberrations in the objective. Unfortunately, we have had no success getting

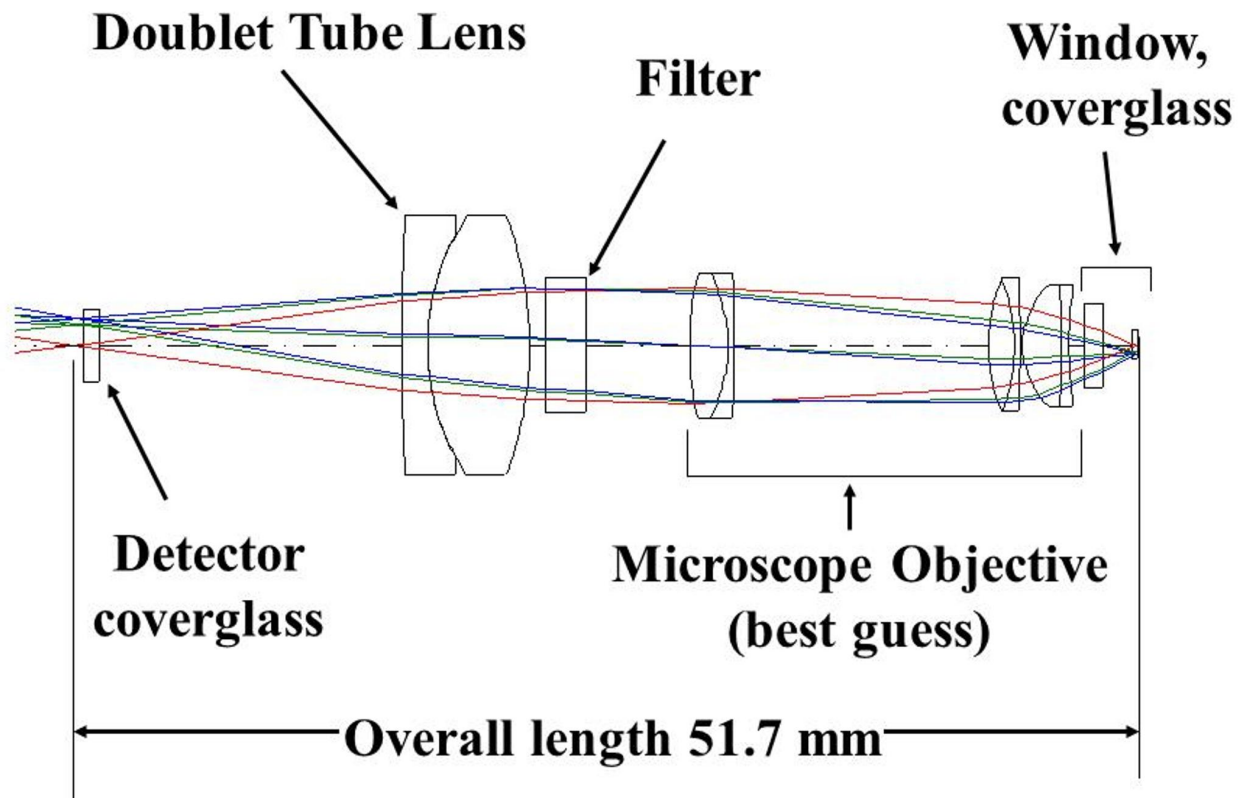


Figure 3.8: **COTS objective with doublet tube lens.** Objective is ORA design based on best-guess: for an objective similar to the Edmund Optics A30-047, a 0.4NA, FN 18 objective with 3.3 mm working distance. Tube lens is an Edmund A32-311; sample coverglass is 0.17 mm BK7, while camera coverglass is 0.7 mm BK7. Courtesy ORA / John Rogers and Tobias Schmid.

such prescription information from Edmund or other companies (quite likely because such low-cost objectives are probably made by yet other “original equipment manufacturing”, or OEM, companies, not the vendors themselves). As a result our subsequent design efforts could optimize only the tube lens component, essentially freezing any objective aberrations into the design. For this reason, Table 3.5 is a useful indicator of how performance can degrade. Notably, the 65% encircled energy (radius at the sample plane) falls at about half the radius of the first zero of the Airy disk, which is itself equivalent to 84% EE and to the Rayleigh resolution.

As a result of these studies, I decided to use a COTS objective, but to go with a slightly more expensive ( $\sim$  \$235) 20X 0.4NA 3.9 mm WD Nikon objective (the MRP00202) to reduce likely aberration issues, and to use a doublet tube lens. I built an initial prototype with this system, which displayed promising performance, and then began working with The Pilot Group in Monrovia, CA to have them produce a more sophisticated prototype based

Field position	Pre-tolerance, $\mu\text{m}$	As-built, $\mu\text{m}$
Axis	2.6 $\mu\text{m}$	4.1 $\mu\text{m}$
0.35 mm radius	0.95 $\mu\text{m}$	1.25 $\mu\text{m}$
0.5 mm radius	2.5 $\mu\text{m}$	3.8 $\mu\text{m}$

Table 3.5: **COTS objective with doublet tube lens.** Values are 65% encircled energy radius values. System is that of Figure 3.8. As-built numbers reflect worst of 100 Monte Carlo cases assuming typical industry manufacturing and construction tolerances, with refocus to best image assumed for each instance. Courtesy ORA / John Rogers and Tobias Schmid.

on my specifications and initial design. During this time a new 5 Mpixel camera became available which allowed a larger field of view but had tighter pixel spacing (2.2  $\mu\text{m}$  vs. 4.4  $\mu\text{m}$ ), requiring a reduction (by a factor of two; c.f. Equation 3.5 in magnification. This entailed a shift from a 150 mm to a 75 mm focal length tube lens, which, coupled with the increase in field of view, resulted in field curvature becoming an issue. Emilio Castaño-Graf, the project lead at The Pilot Group, noticed this and at our request used ZEMAX to design and position an additional singlet field flattening lens to compensate, which restored theoretical performance (not including objective aberrations) to the diffraction limit, as shown in Figure 3.9. This extra lens is required; the maximum field of view radius being a large enough fraction of the required tube lens focal length<sup>9</sup> to make field curvature non-negligible, and fixing this issue in that doublet would require a custom (and expensive) lens in place of the commercial doublet.

### Final optical train

With this addition, the final layout of the collection optics was fixed, and is shown in Figure 3.10; note shown are two folding mirrors used to pack the optical train into a smaller package, as shown in Figure 3.11. The glass slide between the condenser and collector lenses serves to pass the bulk ( $\gtrsim 90\%$ ) of the excitation light while reflecting  $\sim 8\%$  of the light from the green LED, which we use for brightfield illumination.

<sup>9</sup>This does not correspond to field angle, since in our design the system is close to doubly telecentric, making the chief ray angles at the image close to zero; however, it does make intuitive sense to think in terms of the field angle growing larger (and hence field curvature as well) as the focal length shortens and the field radius increases.

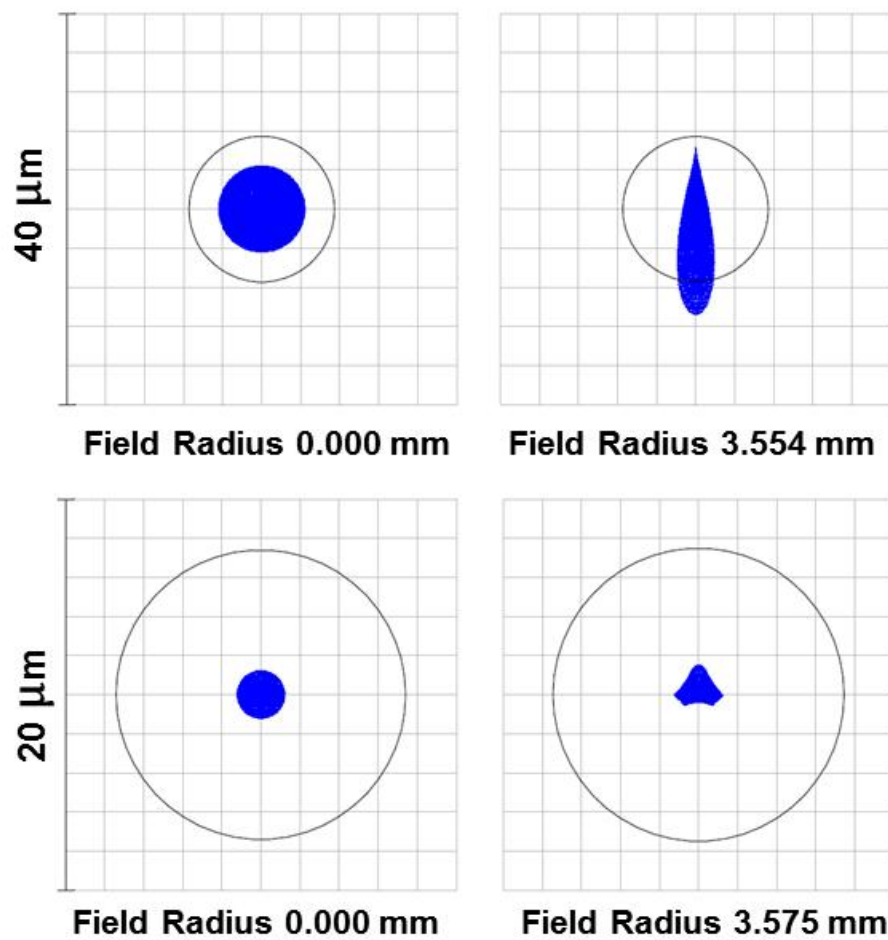


Figure 3.9: **RMS spot size improvement using field-flattening lens.** Spot size at center and edge of image field of view (scale on left of figures). Top: using  $f = 90$  mm doublet; Bottom: using  $f = 75$  mm doublet and singlet field flattener. Ray-trace spot size must be  $\ll$  than the indicated Airy disk radius in order to achieve diffraction-limited performance. Note change of scale from Top to Bottom. Courtesy The Pilot Group / Emilio Castaño-Graf.

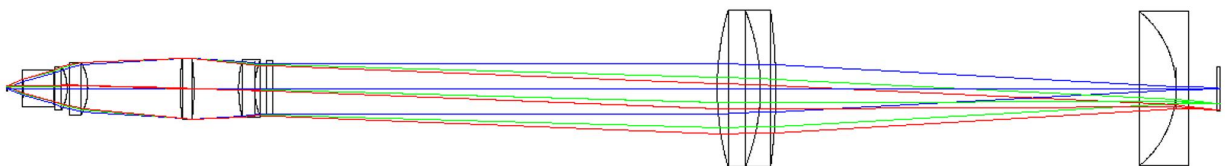


Figure 3.10: **Final optical layout.** Objective model is based on Nikon Patent US889618.

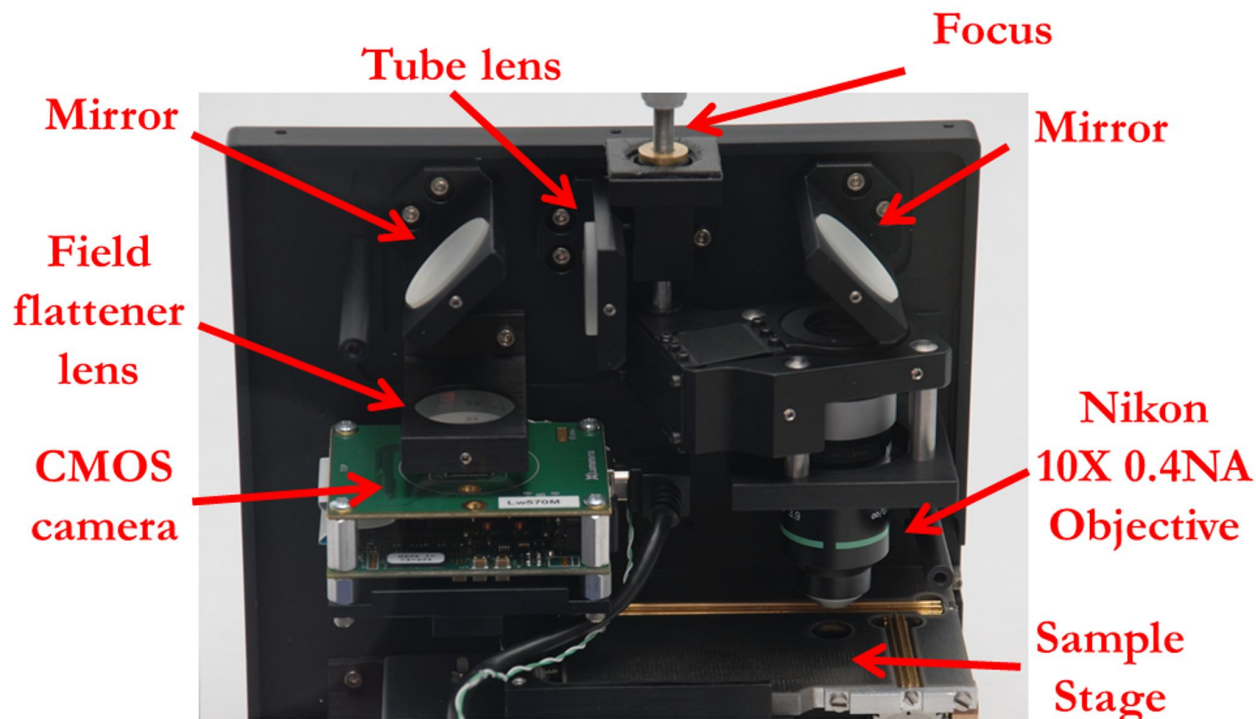


Figure 3.11: **As-built optical train.** Device collection optics as-built. Objective is a Nikon MRP00202 10X 0.4NA with 3.9mm WD. Tube lens is a Thorlabs AC254-075-A achromatic doublet; field flattener is a JAS 012-0133 singlet. Focus mechanism is a modified Thorlabs SM1Z. Folding mirrors are dielectric; Chroma ET545/150m emission filter fits behind objective mount. Camera sensor is an Aptina/ Micron MT9P031 in a Lumenera lw575m system. Not shown: Philips LumiLEDs Rebel Royal Blue LED, a pair of aspheric CVI / Melles Griot 01 LAG 01 005 collector / condenser lenses, and Chroma ET440/40x excitation filter are positioned below the sample stage. Image courtesy The Pilot Group / Emilio Castaño-Graf.

## Resolution

While the Rayleigh resolution for a 0.4NA objective is as stated in Table 3.1, data such as that in Tables 3.4 and 3.5 suggest that aberrations (for this objective cost class, primarily field curvature and astigmatism) and tolerancing issues are likely to reduce as-built performance significantly.

One aberration, field curvature, is typically minimized by focusing at  $\sim 70\%$  of the observable field radius, balancing the field-curvature-induced defocus at the center and edge of the field.<sup>10</sup> This choice of focus position can be seen to have been assumed in Table 3.5,

<sup>10</sup>For a simple lens, field curvature scales with the square of the field radius [103]; this can be understood as the approximation to a spherically curved field being a parabola, so defocus grows as the square of the field position. Consequently, if one focuses at  $1/\sqrt{2} = 0.7$  of the maximum field radius, the errors at the

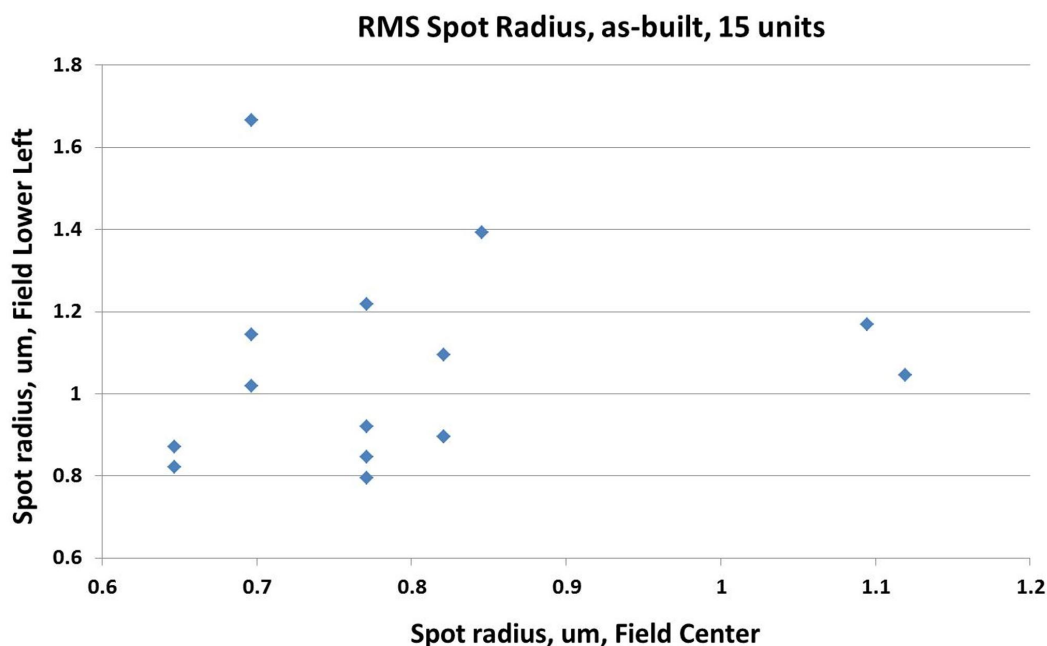


Figure 3.12: **RMS spot size of 15 units, as-built.** Spot size at center and lower left edge of field of view ( $\sim 3.5$  mm radius). RMS radii are overestimated by  $\approx 0.1 \mu\text{m}$  since the test bead radii were not deconvolved from the data.

where the data indicates that the smallest spot radius,  $\sim 0.95 \mu\text{m}$ , will be at the 70% field radius. Communicating this best-focus position to those using the device is important during training, about which I will say more later.

The root-mean-square (RMS, or  $1/e$ ) spotsize is roughly equivalent to half the radius of the Airy disk (which equals the Rayleigh resolution), and falls close to the 65% EE point as well. As a result, Table 3.5 suggests that the “Rayleigh-equivalent” resolution most low-cost microscopes actually achieve is no better than  $\sim 1.8 \mu\text{m}$ , and often 2-3X worse than the Rayleigh calculation would indicate (NB: remember that the table represents the worst-case of 100 Monte-Carlo trials, so most trials will be better than the table lists).

For comparison, Figure 3.12 shows the measured RMS spot sizes at the center and edge of the field when focused at 70% field for 15 of our devices. Notably these values,  $0.8 \pm 0.14 \mu\text{m}$  at the center and  $1.05 \pm 0.24 \mu\text{m}$  at the edge, fall close to what was expected from the modeling. These measurements were done by imaging subresolution beads (181 nm Polysciences Fluoresbrite YG) and the extracting the background-subtracted RMS spot sizes from the images using MATLAB.

This data (Figure 3.12) is easier to interpret using an optical CAD model for a standard low-cost objective (a Nikon 20X 0.4NA long working-distance objective with prescription

---

edge and center will be the same (though of opposite sign).

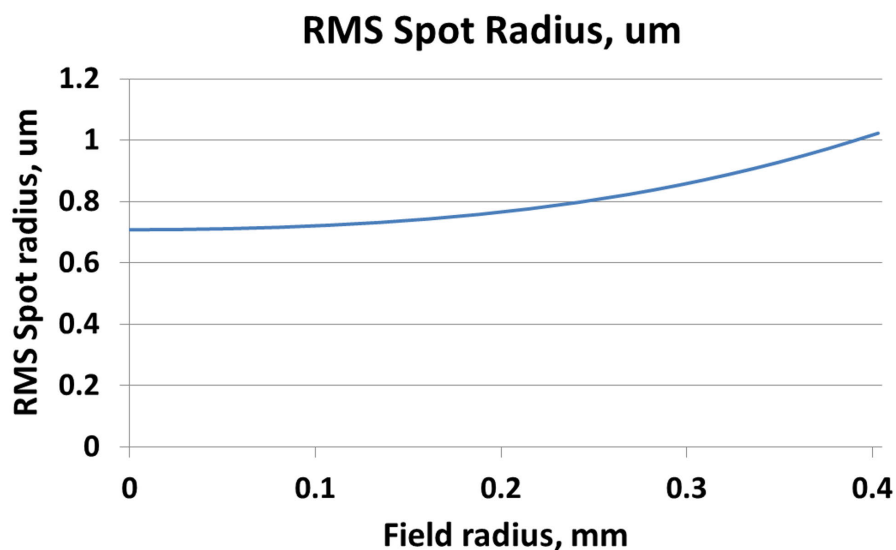


Figure 3.13: **RMS spot size vs. field radius.** ZEMAX calculation uses data from Nikon Patent US5,889,618, Embodiment 2, spectrally weighted for Auramine O emission windowed by the Chroma ET545/150m emission filter.

available in the patent literature [37]) in conjunction with the known prescriptions for the rest of the system optics. The RMS spot radius versus sample field position is shown in Figure 3.13; note the correspondence between the edge-of-field performance and that shown in Figure 3.12. Especially given that manufacturing tolerances would further impact the RMS spotsizes calculated, agreement is quite good and suggests that further effort to improve the optics, short of increasing the optics budget to allow for a higher-quality objective, will not be particularly effective. One implication of this modeling is that full-field-of-view performance for low-cost objective is typically up to several times worse than the diffraction limit would predict; in our case the saving grace is that human users have already been successfully using similar objectives for successful diagnosis for many years.

Especially when images are being interpreted by human beings, care is indicated in discussing the system resolution. For instance, for an incoherently emitting (e.g. fluorescent) sample, the spatial frequency equal to the inverse of the Rayleigh resolution spacing falls where the modulation contrast function (MTF) is  $\approx 9\%$ , not too far from the limit of typical human contrast perception. Humans are most likely to notice larger contrast features, and so the spatial frequencies at which the MTF is larger (e.g.  $\sim 50\%$ ) is a useful indicator of system performance. Figure 3.14 shows the MTF as measured for one device, while Figure 3.15 shows the MTF as calculated using ZEMAX, assuming perfect manufacture (no tolerancing).

Figure 3.15 helps clarify the effect of aberrations in the low-cost objective, particularly

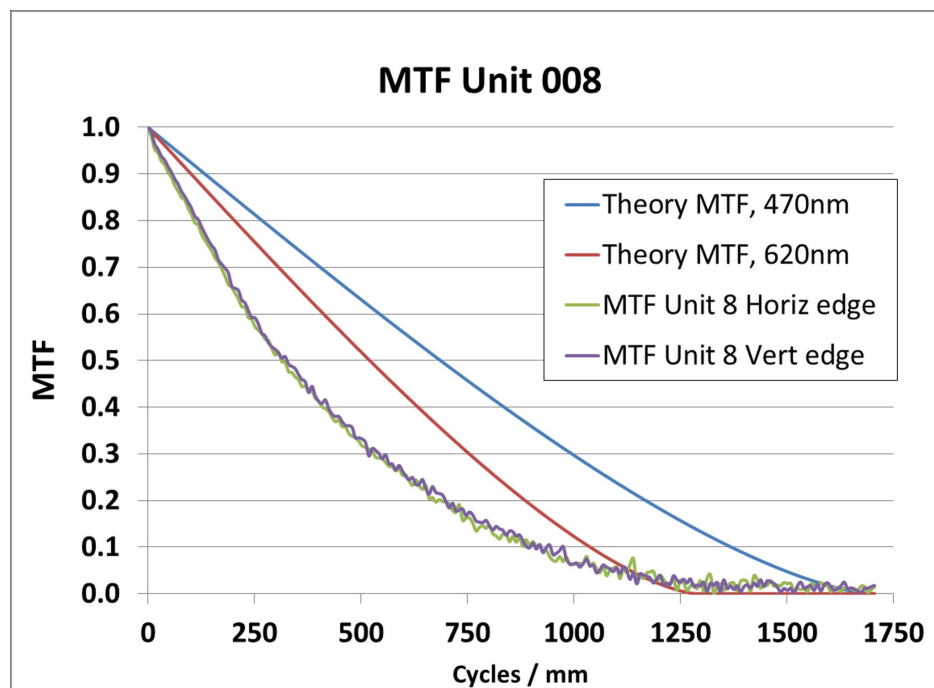


Figure 3.14: **Theoretical and measured MTF curves.** MTF as measured using a chrome edge backed by broadly fluorescent material, for a 512-pixel region near the center of the field, with focus at 70% field; device is Unit #8. Since the MTF is derived from the discrete Fourier transform along 256 pixels on either side of the edge, it is not representative of a single point; furthermore these values are derived from interpolations along a  $\sim 512$  pixel width parallel to the edge. Calculations using NIH ImageJ [95, 83]; see also [10, 96, 41] and references therein.

of chromatic aberration and astigmatism. The notable difference between the Sagittal and Tangential MTF behavior at increasing field radius is clear evidence of astigmatism, while the general decrease in the center-field MTF compared to the diffraction-limited MTF is indicative of chromatic aberrations (though possibly appearing somewhat worse than they actually are due to poor glass data in the patent prescription). These aberrations also serve to reduce the Strehl ratio; c.f. Figure 3.16. The red- and blue-theoretical MTF curves in Figure 3.14 underline the fact that naive calculation of the Rayleigh resolution based on a short wavelength will increase the apparent discrepancy with measured performance when a larger spread of wavelengths is used, e.g. in an effort to obtain brighter images by extending the emission filter transmission band. The Zemax MTF curve shows the correct emission-weighted MTF performance, which falls (as expected) between the red- and blue- theoretical limits. Table 3.6 summarizes this MTF data, and Table 3.7 makes clear that the performance of our devices is within 10%-20% of what would be theoretically expected, and is in fact does

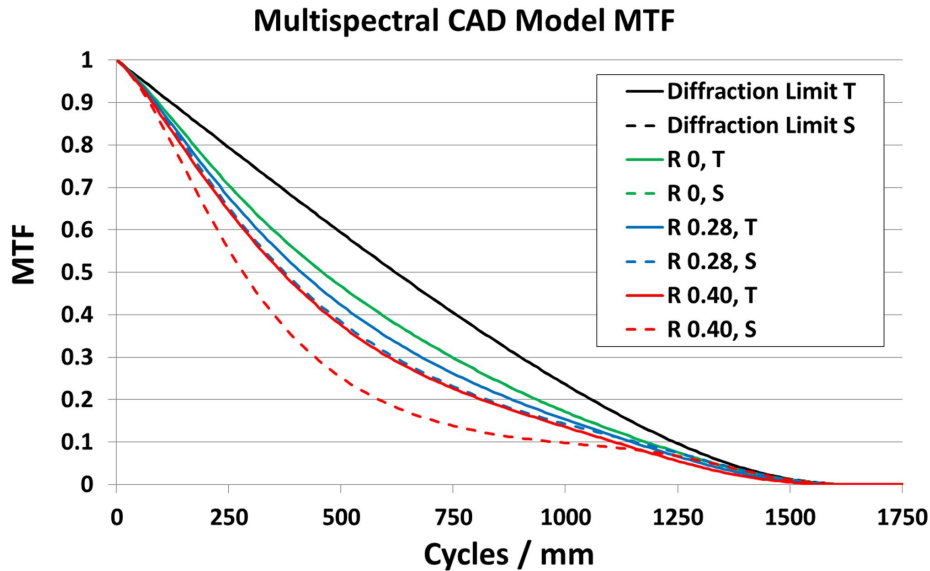


Figure 3.15: **ZEMAX modeled system MTF**. MTF as calculated using ZEMAX, assuming perfect manufacture (no tolerancing) for the device system prescription, referenced to the sample plane. Calculation uses data from Nikon Patent US5,889,618, Embodiment 2, spectrally weighted for Auramine O emission windowed by the Chroma ET545/150m emission filter, and optimized for focus at 70% of the field radius,  $R$ , in mm. S stands for Sagittal and T for Tangential MTF. Cycles / mm calculated using prescription system magnification of 8.707, slightly different than the  $M = 8.845$  of the actual system.

best in the mid-range spatial frequency values (where MTF is  $\sim 50\%$ ) that are expected to be most important for human users, a good result for devices designed for direct assembly (no adjustable components other than the focus).

### Strehl ratio and brightness uniformity.

The same aberrations which reduce resolution reduce peak brightness (the Strehl ratio) for point sources and other small objects such as *tuberculosis* bacilli. Because the bacilli tend to be dim, and the low-cost cameras necessary to keep the device affordable have low bit-depth, fall-off in apparent object brightness near the edges of the field is undesirable — this was, in fact, one reason for the effort put into obtaining good illumination uniformity.

The same ZEMAX model used to evaluate resolution can provide the Strehl ratio as a function of field position, and Figure 3.16 shows this for the critical multispectral (Auramine O emission - weighted) case. Even from the tolerance-free model, it is clear that at the edge of the field brightness will have decreased to  $2/3$  of the center-field value; adding another

		Theory		Multispectral ZEMAX	
MTF	Measured	$\lambda = 620\text{nm}$	$\lambda = 470\text{nm}$	70% Field, Sagittal	Diff. Limit
50%	322	519	692	366	609
9%	967	1061	1399	1175	1245

Table 3.6: **Theoretical and measured MTF.** MTF as calculated for 0.4NA and measured on Device # 8 at MTF values of 50% and 9% (the MTF at 1 / Rayleigh resolution), in cycles / mm at the sample. Zemax model as in Figure 3.15. Note that CAD diffraction-limited values fall intermediate to the blue and red theoretical limits, and the system predicted values are close to the actual system measurements.

		Ratio Meas. / Theory		ZEMAX
MTF		$\lambda = 620\text{nm}$	$\lambda = 470\text{nm}$	Multispectral
50%		0.62	0.47	0.88
9%		0.91	0.69	0.82

Table 3.7: **MTF ratios compared with theory.** MTF ratios to theoretical predictions at the extreme blue and red ends of the emission filter transmission band. Zemax ratios are of measured values to ZEMAX multispectral model 70% field, Sagittal MTF. Note close agreement with CAD, especially given lack of tolerancing in the model.

7% for illumination nonuniformity brings the expected edge-field value to 57%. This is in excellent agreement with the values obtained for 15 devices using the same images as used for the resolution estimates:  $0.54 \pm 0.08$  for the edge / center peak bead brightness.

## Final collection specifications

Overall as-built performance over a full 15 devices is thus quite close to theoretical expectations, and in fact significantly better than might be expected given worst-case tolerance modeling done for us by ORA. Because performance is close to prediction for objectives already used for TB diagnosis by the medical community, it is not surprising that users find the quality of properly focused and exposed images to be generally good; as is shown in Chapter 4, diagnostic quality is more than acceptable. Parameters of the system collection optics are summarized below in Table 3.8.

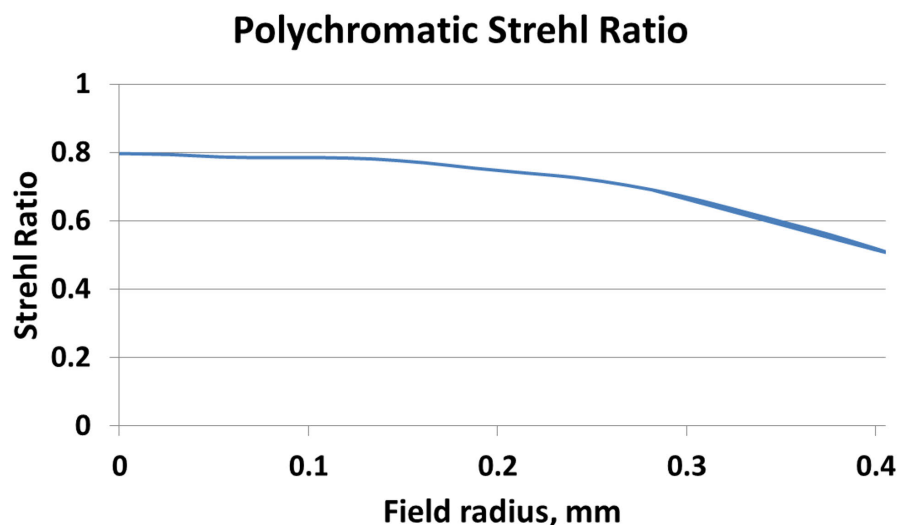


Figure 3.16: **Strehl ratio vs. field radius.** ZEMAX data for model described in text. Center-field value is 0.80; edge-of-field value is 0.51.

## 3.7 Acceptance testing

We had a total of 17 units made for us by The Pilot Group (Monrovia, CA), who (based on my early prototype and detailed specifications) did a beautiful job of the mechanical design, software, and electronics implementations. As with any manufactured devices, it is important to do acceptance testing to assure proper function. In our case, we did the following tests:

### Basic mechanical checks

These involved checking the sample translation stage for smooth function, assuring no loose parts, USB connectors firm, battery check button functional, etc.

### Basic electronics checks

Electronics function was essentially assured by our ability to do the other checks; if USB and camera electronics and communications were not functional, or the power or LED systems were problematic, then we would be unable to image.

### Brightfield imaging

Our first step was to image a chrome test target (typically a chrome square section of a USF 1951 target) which allowed us to take images of edges for use in MTF calculations, as

Calibration	0.249 $\mu\text{m}$ / pixel
Optical Magnification	8.845
Field of view	0.640 x 0.490 mm
Illumination nonuniformity	6.9% $\pm$ 2.4%
Strehl ratio, including Illum. nonuniform.	0.54 $\pm$ 0.08
RMS spot radius, center	0.80 $\pm$ 0.014 $\mu\text{m}$
RMS spot radius, edge	1.05 $\pm$ 0.024 $\mu\text{m}$
Rayleigh resolution	0.76 $\mu\text{m}$
Excitation band	420-460 nm
Emission band	470-620 nm

Table 3.8: Measured specifications for 15 devices.

well as to test the focus mechanism both for smooth function and to see that the middle of its travel range fell at the standard sample position. We also verified that brightfield illumination was sufficiently bright (a range of 10-20 ms exposures, short enough for video rate imaging at any zoom level where the camera permitted it, was considered appropriate). We also took images of a 200 lp / mm chrome Ronchi ruling for assessment of any gross distortion issues, though these were (as expected) always below the perceptible level; measurements by a colleague suggest  $< 1\%$  over the entire field of view.

### Camera tests

Using the chrome slide as a sample (thus blocking all light) we took images in brightfield at 4 ms and 500 ms. The former allowed estimation of read noise (average noise in the image, since there was effectively no illumination — the brightfield LED is too dim to register when blocked by a chrome sample, though we also tested the same sample using 1000 ms fluorescence exposures, which would be vastly worse in terms of leakage due to the much higher source powers ( $\sim 700$  mW vs.  $\sim 20$  mW for the 525 nm brightfield LED). The latter measurements allowed estimation of dark signal as well as leakage of fluorescence excitation around the optics (as opposed to through the filters). We could also check the images for numbers of “hot” pixels, showing abnormally high readings in both short and long exposures. After several units we ceased doing most of these tests for the sake of time. In larger scale manufacture, automated test and measurement systems might make this a worthwhile effort, but it would probably be more efficient to test the cameras in a fixture before assembly, and not to try to catch errors of this sort in the finally assembled units.

## Fluorescence imaging

This was the most critical to the intended device use, and so received the bulk of our attention. Tests included:

**Filter leakage** Using a blank glass slide as a sample, we took a 1000 ms fluorescence exposure, then measured average image pixel value. This averaged  $66 \pm 13$  counts over all 15 units tested, indicating leakage through the filters of approximately 10% of the FWC during a typical 200 ms exposure. While we could consider re-specifying the filters to reduce this, it was found during validation testing (Chapter 4, done before the subsequent 15 units were ordered) that some leakage was useful to provide minor sputum contrast during scanning of the smear. While we could have removed leakage and used low-level brightfield LED illumination synchronous with the fluorescence imaging to achieve the same effect, I judged that nominal decrease in background to not be worth the effort required.

**Excitation power** As it was not possible to introduce a commercial power meter of any kind into the small sample tray slot in the devices, we used leakage through the filters as a proxy for power level. This varied by  $\pm 20\%$ , which is within expectation for the LED variation given that we could not afford to order in quantities sufficient to enable binning by output power.

**Excitation uniformity** The same leakage images also allowed estimation of illumination uniformity, defined as  $[(\max - \min)/\text{center}]$  of 128 x 128 pixel boxes in the center and each corner of the image. Typical values, as stated earlier, were slightly less than 7%.

**Fluorescence MTF** We affixed to the bottom of the chrome slide a fluorescent object (a blue Post-It sticky label) broadly emitting in the transmission band of our emission filters. This allowed imaging in fluorescence of an edge, for calculation of the MTF (as in Figure 3.14). The fluorescence MTF involves different (and longer) wavelengths than the brightfield LED generates, and is more directly relevant to Auramine O imaging performance. We did this for vertical and horizontal edges, though we saw no difference in the MTF values. We did not calculate MTFs for the images from every unit, but used the figures as a check against performance on bead tests whenever a question arose.

**Sub-resolution bead imaging** We prepared samples as follows: 181 nm dia. Polysciences Fluoresbrite YG polystyrene beads were vortexed, 10  $\mu\text{l}$  dissolved 100:1 in reagent-grade ethanol (EtOH), with the EtOH pipetted in and out of the tube for mixing, vortexed, and sonicated for 5 min. This procedure was then repeated to achieve a 1:10<sup>4</sup> dilution. A 10  $\mu\text{l}$  aliquot was pipetted onto a glass slide which had been sonicated in reagent grade EtOH and dried previously. A black Sharpie-brand marker was used to draw a circle around the dried bead area for focusing during brightfield imaging (grease pencil works better, since it also tends to fluoresce).

We imaged these beads, with focus on at 70% of the field radius (i.e. 70% toward the corner along a diagonal from the center), optimizing exposure to fully use the camera dynamic range. Required exposure provided an additional check on excitation power levels; typical values were  $450 \text{ ms} \pm 110 \text{ ms}$ , in keeping (these measurements being coarser) with the leakage test. These bead images then provided two important measurements:

**Strehl ratio:** we measured (using ImageJ [95] the peak bead pixel value for representative beads (typically an “eyeball average” of 3 beads) in the center and each corner of the image. The Strehl ratio was then calculated as  $[(\text{max} - \text{min})/\text{center}]$ , and was  $0.54 \pm 0.08$  over 15 units, as previously stated.

**RMS spotsize:** I wrote a MATLAB script that allowed me to choose a region containing both a single bead and an area (ideally large) containing only background. This code then:

1. calculates the mean and standard deviation ( $\sigma$ ) of the region, then recalculates the mean and a new  $\sigma$  after *excluding* all pixels  $> 3\sigma$  above the previous mean, in order to reduce bias from the bead intensity.
2. subtracts off the new mean less  $1\sigma$  to prevent falsely lowering the wings of the bead.
3. calculates the mean (centroid) and RMS radius based on that mean location and the known pixel intensities in the region.
4. recalculates the average background from the entire region outside one RMS radius from the mean bead center position; this calculational area contains only background since the large nonzero background region has caused the RMS bead radius to be significantly overstated at this point.
5. subtracts this average value from the entire image, and sets any negative pixels to zero.
6. recalculates centroid and RMS radius.
7. repeats steps 4 through 6.
8. reports the RMS pixel size in pixels or (using the  $0.249 \mu\text{m} / \text{pixel}$  calibration, in *micrometers*).

I calculated RMS values for beads at the center and lower left corner of each image; these are plotted in Figure 3.12. Larger values in the corner are due to astigmatism apparent in the images. I did not deconvolve, or subtract off, the bead radius from these measurements, making them a slight overestimate. RMS spotsize corresponds theoretically to approximately half ( $0.304 \lambda / \text{NA}$ ) of the Rayleigh resolution figure, and this can be used during comparison to the measured values.

### Trained user assessment of sputum smear image quality

Of course, the most important test of a TB-diagnostic system is whether it images TB AFB well. For this we relied on our own experience and especially that of Clay Reber, one

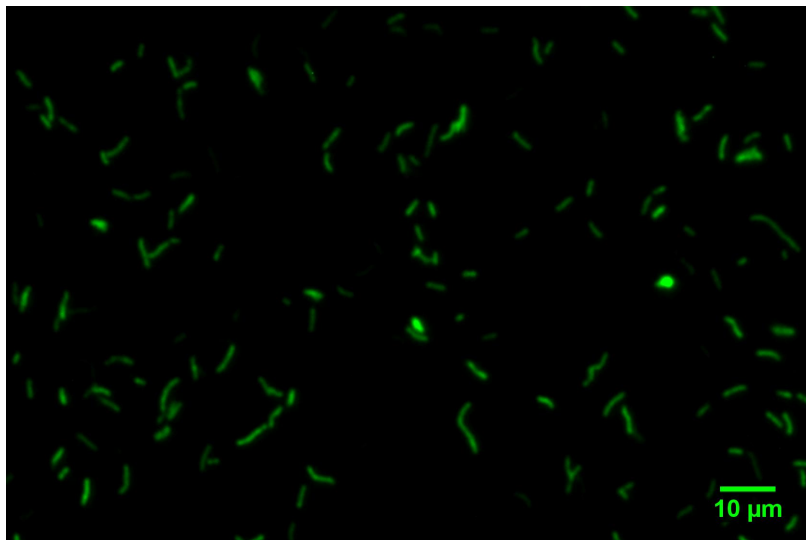


Figure 3.17: **TB imaged with the system.** AFB in a sputum smear (culture positive for TB) imaged using the system. Scale bar is 10  $\mu\text{m}$ ; background has been subtracted and contrast stretched for visibility in printing, however the same thing can be done in real time for the system user.

of the trained readers from the validation protocol (Chapter 4). A freshly-restrained, culture-confirmed TB-positive sputum smear was evaluated in each unit; an example of TB imaged using the system in this manner is shown in Figure 3.17. This test was the final and most important.

## 3.8 Software

The microscope unit is connected to a laptop via USB 2.0, and the laptop is used for all control functions regarding the camera, as well as the user interface, image storage and transmission, etc. There is some on-board control, including a battery-check indicator light; furthermore, the high-power fluorescence LED is toggled on and off by an output TTL signal from the camera synchronous with the camera exposure start and stop. The brightfield LED is similarly controlled on-board.

When a technician logs onto the system and chooses to start reading slides, they are prompted to enter the patient number (tracking this number is done by hand-written logs, or by a web-based software interface installed at the Hanoi site by UCSF personnel). Once this has been entered, any images taken will be labeled with the username, location, date, time, an patient number, as well as any diagnosis.



Figure 3.18: **Software interface: brightfield imaging.** Dark line is line drawn on the slide using a marker. The exposure (and thus the image brightness) can be adjusted using the value in the “Exposure” box on the left center of the screen, or by clicking “AutoExposure”. Images are presented at 6 fps for focusing; however, if the user drags a box on the screen using the mouse, the window will zoom to that region of interest (ROI) and the frame rate will increase to the maximum possible given this ROI, thus allowing smoother focusing and easier assessment of focus quality.

## Brightfield imaging

At this point the user inserts the slide in the device, and chooses via the software to begin acquiring images. The first images acquired are in brightfield, for ease of focusing and to prevent wasting power ( $\sim 5$  W) on the fluorescence LED before the sample is properly in focus. The interface looks as is Figure 3.18, and the users are trained to insert the slide and position it so that they can focus on the grease pencil line that is typically drawn on sputum smear slides circling the smear. Conveniently this grease is usually also fluorescent, so one can focus on the same line during fluorescence imaging if need be.

Once the slide is in good focus using brightfield, the user clicks on “Fluorescence” in the lower left to shift to fluorescence imaging.

## Fluorescence imaging

Once in fluorescence mode, exposure can be set separately for “Normal mode” which has gain = 1 for low-noise (but requiring longer exposure) imaging and “Scan mode”, which has high ( $\sim 12-15$ ) gain to allow video-rate imaging during focus and when scanning the slide

(moving the slide while imaging, watching for bright objects worth examining more closely). Typical values are 30 ms for Scan mode and 100-300 ms for Normal mode. Once an object of interest has been found and focused on, an image is taken in Normal mode for record keeping and transmission to the central district hospital for quality assurance checks. These features, as well as the zooming capacity, are shown in Figure 3.19.

## Image storage and transmission

Once the user has found and taken a high quality (in focus, properly exposed) of suspicious objects, they can decide whether they are TB or not; in either case, the images are automatically uploaded for diagnostic confirmation and quality assurance by the district hospital, to whom we have provided software for image review.

## 3.9 Use model

The use model for the system involves the fact that it is portable, simple to set up, and quick to use, coupled with the fact that images are auto-uploaded to a central facility for quality control and monitoring purposes.

A traveling medical technician, with relatively little training (the validation data in Chapter 4 were taken by individuals with only one week of training with the device) can easily carry both the diagnostic unit and the required sputum staining kit in a backpack. The staining procedure requires a sink and two minutes of time; setting up the device is equally fast: see Figure 3.20:

Once the slide has been stained and dried, it can be placed into the slide tray which is then slotted into the microscope unit. Focusing follows, first in brightfield, then in fluorescence, and scanning the slide take  $\sim 4$  minutes, in keeping with international standards. This is shown in Figure 3.21.

Once the slide is read and images of any potential bacilli have been taken, the technician makes a diagnostic decision and the images are automatically tagged with that information and uploaded via the 3G mobile phone network to the local district hospital for quality control and diagnostic confirmation, as shown in Figure 3.22.

The next step for system development will be to implement the automatic-ID algorithm at the district hospital level; its function is shown in Figure 3.23. Fine-tuning of the algorithm parameters for optimized diagnostic sensitivity and specificity for the local conditions will follow.

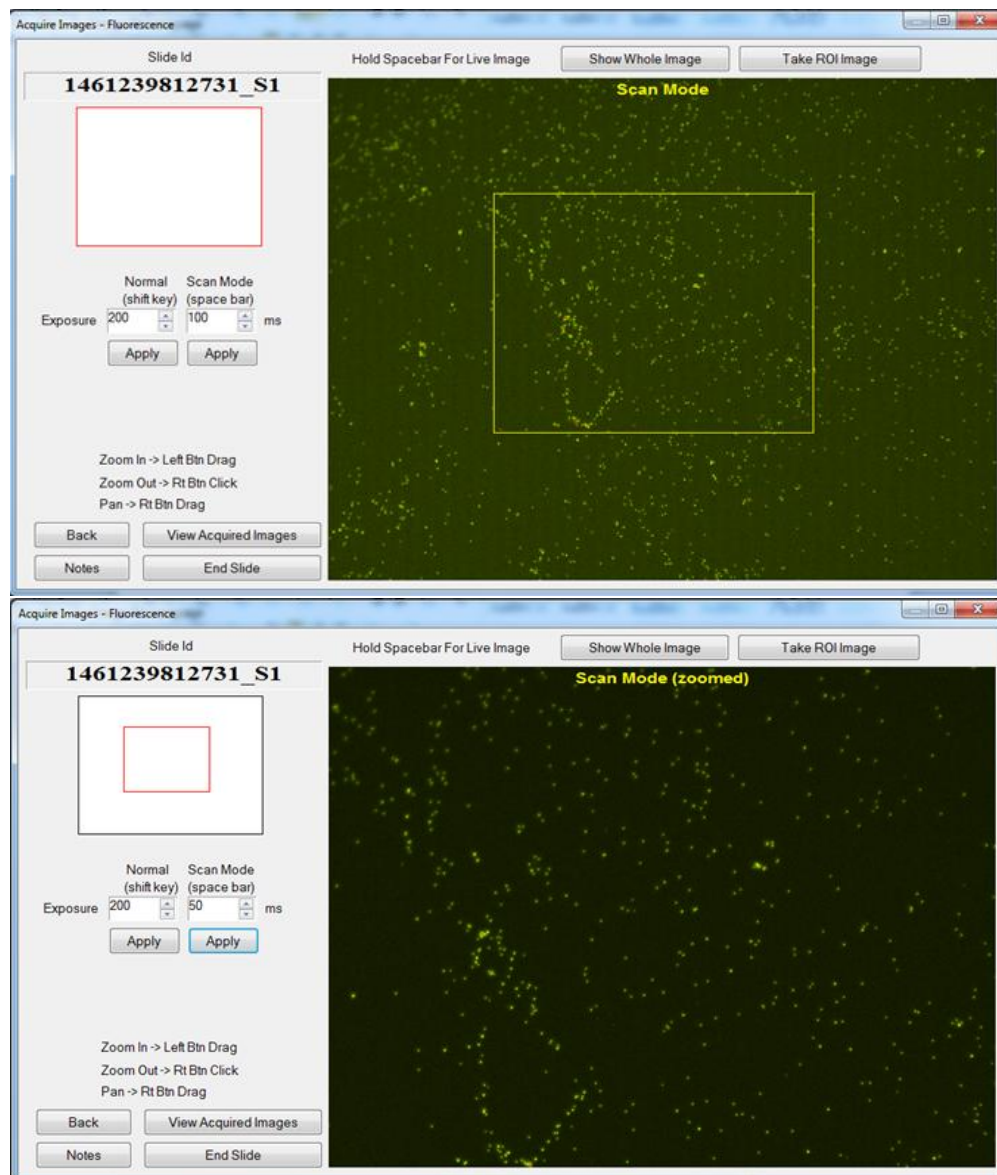


Figure 3.19: **Software interface: fluorescence imaging.** Top: fluorescence image, with “zoom” box dragged on it using mouse; Bottom: zoomed-in image; note red square inset in white rectangle in upper left showing zoom region. User can save images by clicking “Take ROI Image” on top bar. Images courtesy Anh-Thi Le.

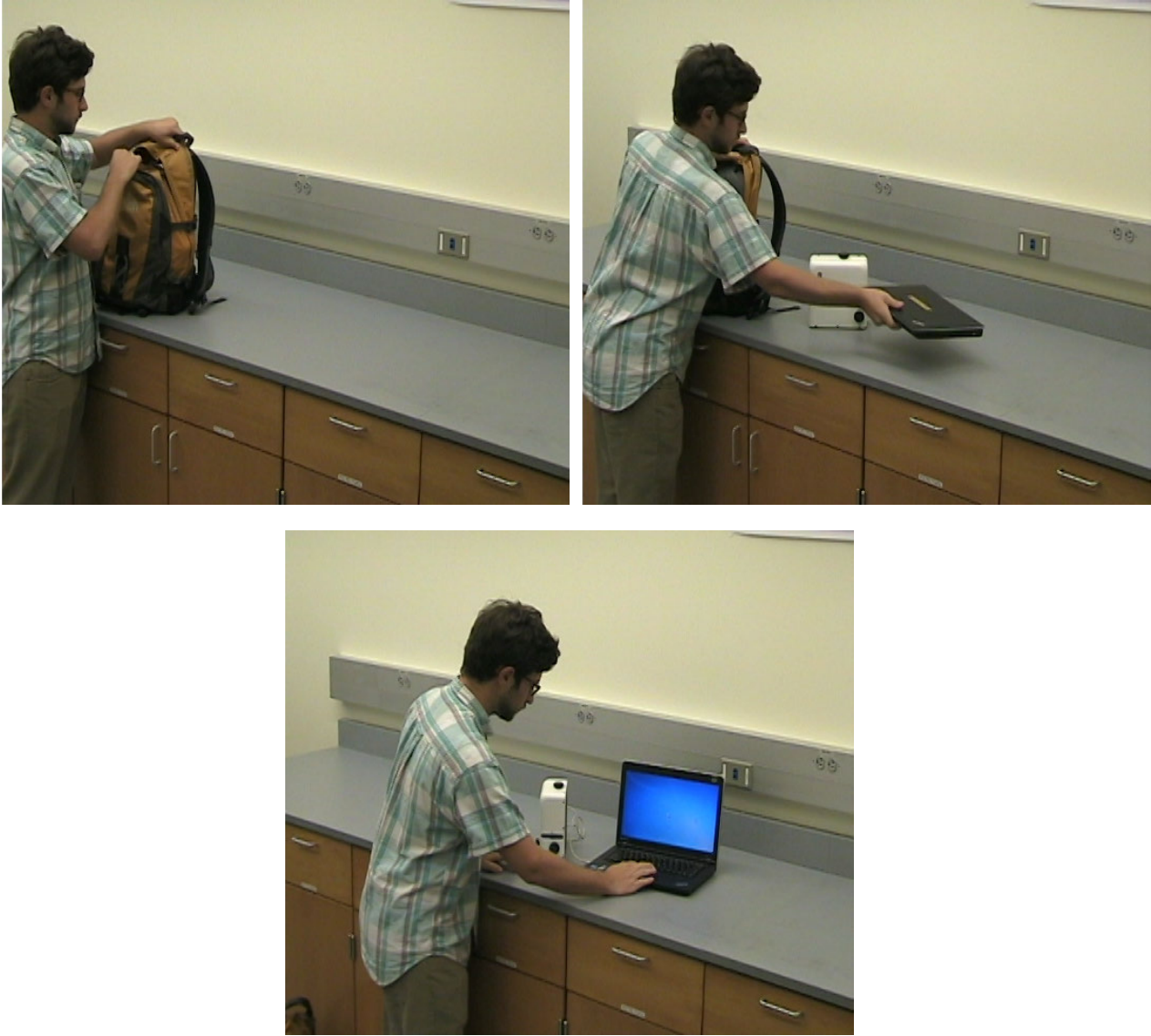


Figure 3.20: **Backpack portable diagnostic.** Unit can be carried in a backpack, removed, set up, and be ready to image in minutes.

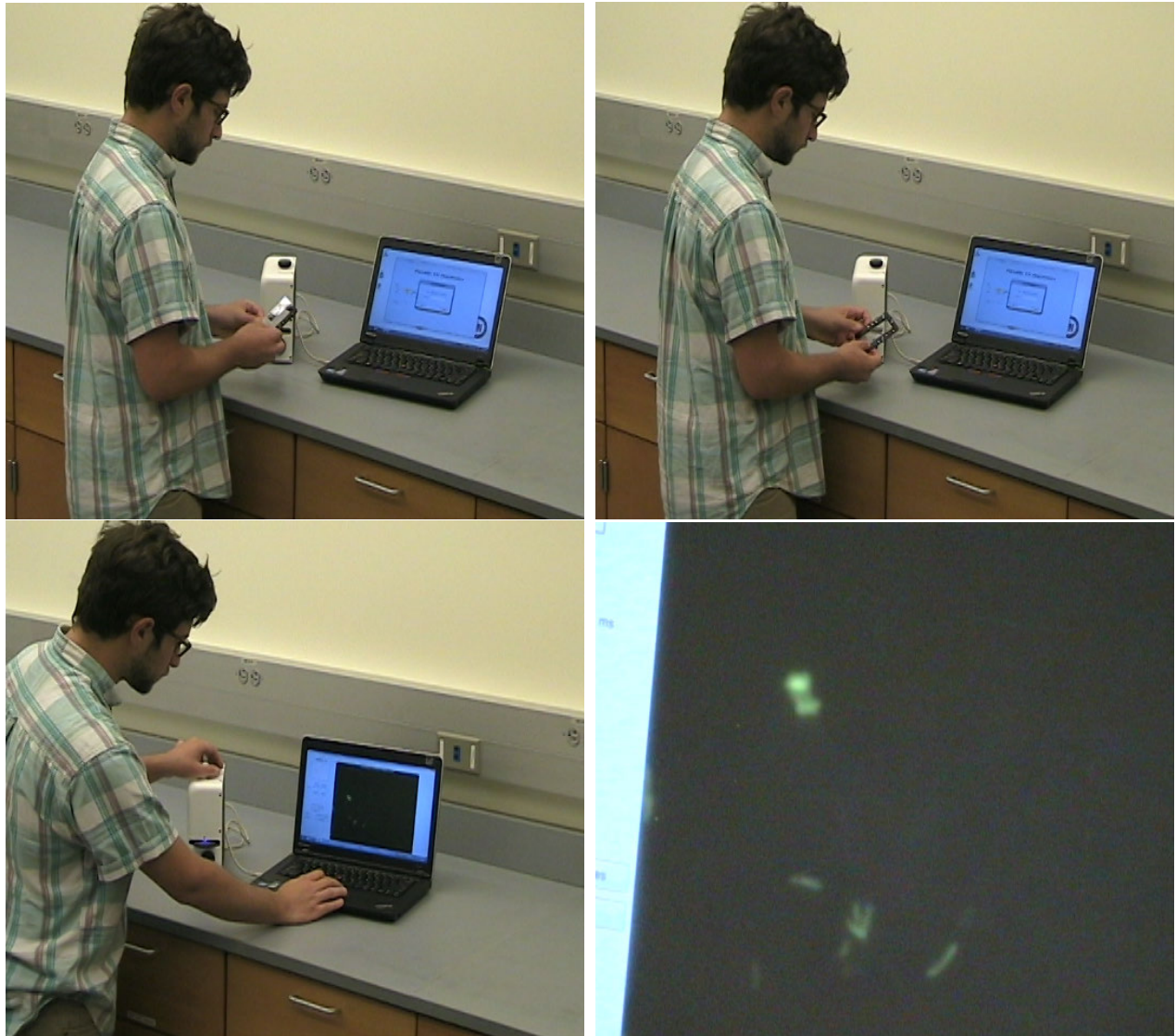


Figure 3.21: **Slide reading.** Slide reading takes 3-5 minutes. Clockwise from top left: placing slide in tray; placing tray in device; focusing image; visible TB bacilli on the laptop screen, imaged with room lights on.



Figure 3.22: **Image upload to central hospital.** Saved image automatically upload to the central district hospital for quality control and diagnostic review. Clockwise from top left: Image is saved; image automatically uploads to the next computer using the mobile phone network; when upload is complete the toolbar icon (blue box) features a checkmark; directory on district hospital laptop showing uploaded images.

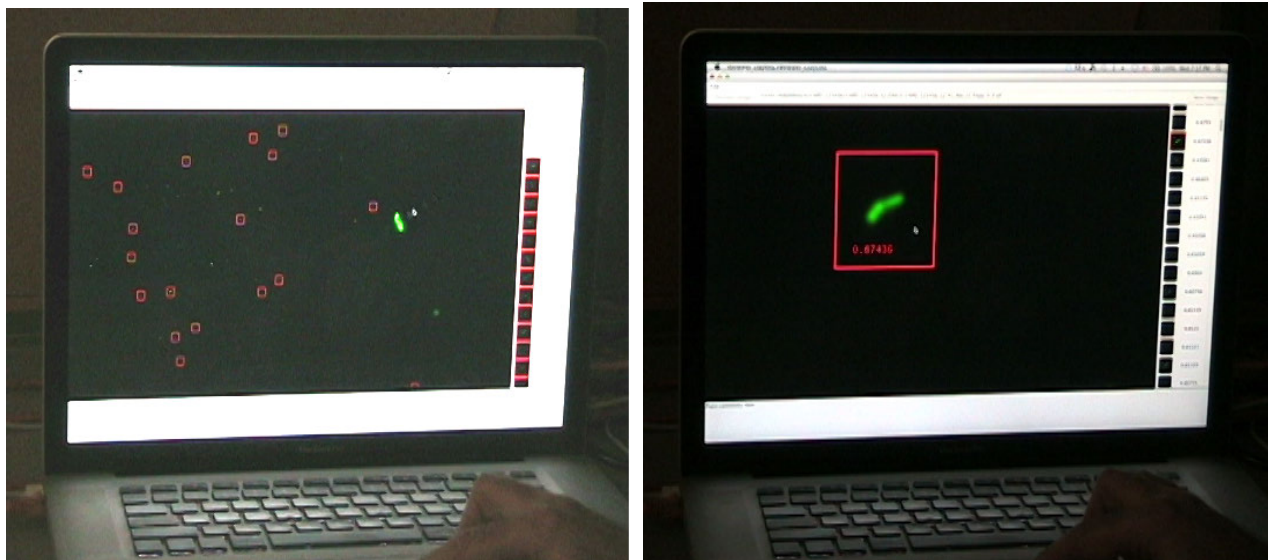


Figure 3.23: **Auto-ID diagnostic algorithm.** Left: bacilli are auto-identified in the uploaded image. Right: each bacilli can be zoomed in on for quality control checks. Note confidence score assigned to this bacillus by the auto-ID algorithm.

# Chapter 4

## Device Validation

### 4.1 Introduction

Having developed a portable microscopy system capable of good imaging, the obvious (and critical) next step was to do validation testing to verify whether it was, indeed, useful for TB diagnosis.

Although the initial concept had been of a device where the user would take several images which would then be processed off-line, perhaps by an automated algorithm (in fact the subject of the following chapter), it rapidly became clear as we began to engage more heavily with physicians Luke Davis and Adithya Cattamanchi at UCSF's Curry International Tuberculosis Center that the typical area of a smear that was examined was far larger than we had anticipated; for instance, the San Francisco Department of Public Health's Mycobacteriology section actually examine the entire  $\sim 2 \text{ cm}^2$  smear area. Since to a first approximation diagnosing TB by smear microscopy involves finding  $> 0$  bacilli in an area of smear, and in such situations the appropriate theoretical distribution is the Poisson, where the probability of finding  $n$  bacilli in an area  $a$  with mean value of  $\sigma$  bacilli per unit area (corresponding to some concentration of colony-forming-units, CFU, in the original sputum sample, possibly also including non-viable bacilli that still look like TB) is

$$P(n) = \frac{(a\sigma)^n e^{-a\sigma}}{n!}, \quad (4.1)$$

which indicates that the probability of a false-negative, i.e., of finding  $n = 0$  bacilli in some area  $a$  despite the patient having some  $\sigma > 0$  is

$$P(0) = e^{-a\sigma}. \quad (4.2)$$

Consequently, the probability of a false-negative diagnosis drops exponentially with increasing smear area examined. For this reason we readily shifted to accommodate the new information on the larger-than-anticipated scan areas. This required a major shift in the use-model for the device software; originally designed for the taking of discrete images, we

now decided to use the system to scan along a length of the smear, looking for bright objects at high camera gain (allowing for adequate image brightness at short exposures, necessary to avoid image “smearing” if the sample is being moved during exposure). Only once likely objects had been found would the user shift to more refined, longer-exposure, lower-gain imaging for the images on which diagnosis would depend.

While from the perspective of training unfamiliar users taking a few fixed images is certainly simpler than teaching the scanning technique, it is a testament to the software approach we took that it could be successfully repurposed on the fly in this way. With modifications based on the lessons we learned during the following work, that same software is now successfully deployed with the 15 devices in a study in Hanoi.

Of course, such deployment would not have occurred if the initial validation studies had not been successful. The details of that work comprise the current chapter.

## 4.2 Mobile digital fluorescence microscopy for diagnosis of tuberculosis

Asa Tapley<sup>1,#</sup>, Neil Switz<sup>2,#</sup>, Clay Reber<sup>3</sup>, J. Lucian Davis<sup>4,5,6</sup>, Cecily Miller<sup>4</sup>, Daniel A. Fletcher<sup>2,3</sup>, Adithya Cattamanchi<sup>4,5,6</sup>.

<sup>1</sup> School of Medicine, University of California San Francisco; <sup>2</sup> Biophysics Group, University of California Berkeley; <sup>3</sup> Bioengineering Department, University of California Berkeley; <sup>4</sup> Division of Pulmonary & Critical Care Medicine, University of California San Francisco; <sup>5</sup> Curry International Tuberculosis Center, San Francisco General Hospital, University of California San Francisco; <sup>6</sup> Makerere University-University of California San Francisco Research Collaboration, Kampala, Uganda.

# These authors contributed equally to this work.

As in preparation for submission to: *Journal of Clinical Microbiology*, 2012.  
Additional detail can be found in Asa Tapley’s Master’s Thesis [112, 28].

### Abstract

#### Background.

Increasing access to high-quality sputum smear microscopy services for diagnosis of tuberculosis (TB) is a priority for global TB control efforts. We evaluated the accuracy of CellScope — a novel, portable digital imaging system — in comparison to conventional LED fluorescence microscopy (FM).

## Methods.

The study involved stored smear microscopy slides prepared from sputum specimens submitted by consecutive adults with cough  $\geq 2$  weeks' duration admitted to Mulago Hospital (Kampala, Uganda). LED FM and mycobacterial culture were performed by technicians at the Uganda National Tuberculosis Reference Laboratory within 24 hours of sputum collection. Two postgraduate researchers in the U.S. with no prior microscopy experience re-stained stored microscopy slides, and imaged and interpreted the slides using CellScope. We assessed whether the sensitivity and specificity of CellScope-based LED FM was non-inferior to conventional LED FM, using a pre-selected margin of inferiority of 15%.

## Results.

Of 525 patients included, 72% were HIV-seropositive and 39% had culture-confirmed TB. The proportion of positive results was similar with CellScope-based and conventional LED FM (34% vs. 32%), and there was moderate correlation between techniques (weighted kappa 0.7). In a sub-analysis of 43 slides read twice by both CellScope users, inter-reader reliability was moderate (weighted kappa 0.6) and intra-reader reliability varied by user (weighted kappa 0.1 vs. 0.5). Both the sensitivity (62.8% vs. 69.6%, difference 6.8%, 95% CI 0.7%–12.9%) and specificity (85.2% vs. 92.5%, difference 7.2%, 95% CI 2.8%–11.7%) of CellScope-based LED FM were within the pre-specified non-inferiority margin.

## Conclusions.

CellScope offers promise for expanding microscopy services beyond traditional TB diagnostic centers. Further studies are underway to determine efficacy of use by field technicians in developing countries, and the accuracy and efficacy of remote diagnosis and quality control using images transmitted by the device to a central facility. An automated algorithm has been shown to have diagnostic accuracy equivalent to our human readers [18], offering the possibility of increased efficiency and decreased training requirements for users at peripheral levels of the healthcare system.

## Introduction

Tuberculosis (TB) continues to be responsible for more deaths than any other infectious disease besides HIV/AIDS [71]. An estimated one-third of individuals who develop TB annually fail to be diagnosed and treated according to international standards [107]. Sputum smear microscopy is capable of detecting the majority of infectious TB cases and mathematical models suggest that expanding access to high-quality smear microscopy could improve individual outcomes [64] and reduce TB prevalence and incidence [27]. Although recently developed molecular detection methods are becoming available in some diagnostic centers [5],

the costs and infrastructure requirements of current tests are prohibitive for most peripheral clinics in high-burden countries [29]. Therefore, efforts to improve the quality and expand the reach of microscopy continue to be a global priority [116].

In low-income countries, smear microscopy typically involves direct visualization of stained smears by trained technicians using conventional light microscopes. In contrast, in high-income countries, microscopy in the related discipline of pathology increasingly involves the use of digital images viewed on high-resolution monitors, an approach that maintains or improves diagnostic accuracy [88, 97]. Moreover, compact, long-lasting light-emitting diodes (LEDs) [44]; complementary metal-oxide semi-conductor (CMOS) image sensors with high sensitivity and large pixel counts [33]; and other recent technological advances provide an opportunity for expanding access to TB diagnostic services through portable, low-cost digital microscopes.

Here, we report the first diagnostic accuracy evaluation of CellScope, a novel digital microscopy device, in comparison to conventional LED fluorescence microscopy. We hypothesized that the capacity to enlarge and enhance objects of interest with CellScope-based digital LED FM would allow individuals with no prior smear microscopy experience to have similar accuracy compared to conventional LED FM performed by experienced microscopists.

## Materials and Methods

### Device description.

CellScope is a portable digital-imaging microscopy device which can upload images to a central facility via the mobile phone network. For this evaluation, we used a stand-alone, portable, battery-powered prototype platform that incorporates LEDs and a light sensor typical of commercial camera phones within an enclosed plastic case 4.1. The case included a slide loading tray and knobs for manual adjustment of slide position and focus. We connected the platform via a USB 2.0 cable to a low-cost laptop computer (Intel Classmate PC<sup>TM</sup> laptop, EliteGroup, Taiwan) featuring a 1024 x 600 pixel LCD display and custom software to enable visualization and interpretation of digital images.

### Sample selection.

This study included smear microscopy slides prepared from early-morning sputum specimens submitted by 585 consecutive adults (age  $\geq 18$  years) with cough  $\geq 2$  weeks' duration admitted to Mulago Hospital (Kampala, Uganda) between September 2007 and January 2008. Details of patient enrollment and evaluation for the parent study have been published previously [14, 13]. Briefly, enrolled patients submitted two sputum samples for mycobacterial smear and culture at the Uganda National Tuberculosis Reference Laboratory (NTRL). The NTRL has participated in a biannual external quality assurance program for smear microscopy administered by the World Health Organization since 2005. Experienced NTRL technicians prepared direct smears on glass slides, stained them using auramine-O, and in-

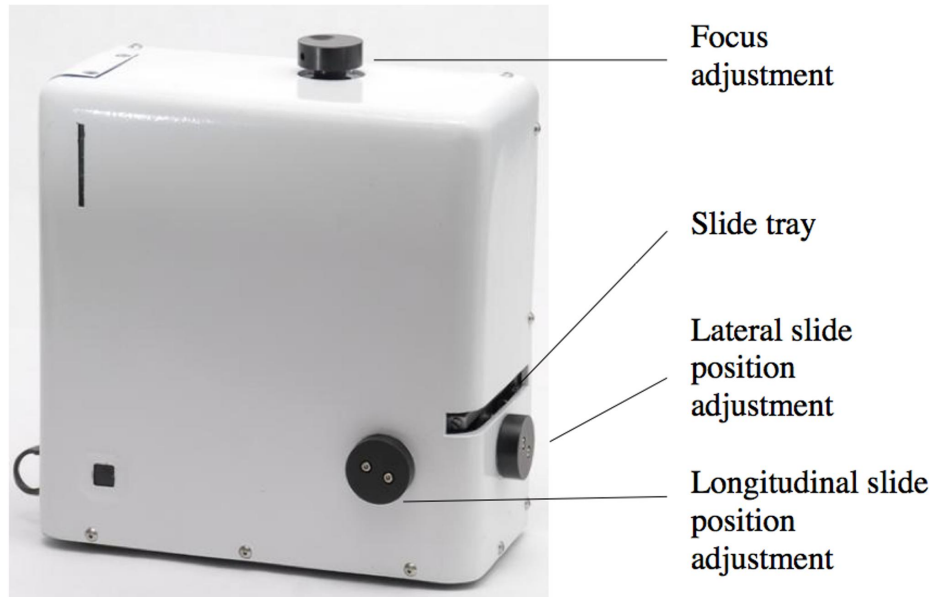


Figure 4.1: **CellScope for digital light and fluorescence microscopy.** Dimensions: 20 x 20 x 10 cm. Weight: 3 kg.

terpreted results using LED FM (Lumin; LW Scientific, Lawrenceville, GA) in accordance with standard algorithms [13, 65, 127]. The technicians also cultured sputum sediment on solid Löwenstein-Jensen media and/or liquid media [13, 127]. The slides were then transported in opaque boxes to a laboratory at the University of California Berkeley where all further aspects of the study were completed.

### Digital fluorescence microscopy.

Two postgraduate researchers (AT and CR) without prior microscopy experience and blinded to the original LED FM and culture results re-examined smears using identical CellScope devices. Each reader received 20 hours of training on device operation from CellScope engineers and on staining, slide reading, and acid-fast bacillus (AFB) identification from professional microscopists in the Mycobacteriology Section at the San Francisco Department of Public Health.

The readers re-stained slides in batches ( $\leq 20$  slides) [62] using the three-minute F.A.S.T. auramine-O stain kit (QBC Diagnostics, Port Matilda, PA) [47], and imaged and interpreted slides within 24 hours of staining according to a standardized protocol. We randomly divided the initial 535 consecutive slides equally between the readers, and each read their assigned slides once and scored them as positive or negative based on the detection of AFB within one smear length. The remaining 50 slides were read twice by each reader and scored using the IUATLD/WHO semi-quantitative grading system for LED FM [127]. For the purposes of

blinding, a study coordinator not involved in slide reading implemented a re-labeling system. We collected reading time for all slides. The CellScope digital images have  $0.76 \mu\text{m}$  nominal resolution (equivalent to a standard 0.4NA 20X objective), are digitally, sampled above the Nyquist criterion, and are presented to the user at magnifications of  $\geq 500\text{X}$ . The individual image field of view is  $0.644 \times 0.486 \text{ mm}$ , and the slides are read by scanning along a  $0.644 \text{ mm}$ -wide length of the smear. Further details on device design will be published elsewhere.

### **Statistical analysis.**

We sought to evaluate whether the diagnostic accuracy of LED FM performed by inexperienced readers using CellScope was non-inferior to that of LED FM performed by experienced technicians using a conventional LED fluorescence microscope. The sample size was determined by the number of patient slides available for the analysis. Assuming 60% sensitivity and 95% specificity of LED FM and 40% prevalence of culture-positive TB [109], we projected 80% power to determine if differences in sensitivity and specificity between CellScope and conventional LED FM were within a pre-specified non-inferiority margin of 15%, based on a one-sided test of correlated proportions at a 5% significance level (Power Analysis and Sample Size; NCSS, Kaysville, UT). We chose this margin of non-inferiority because CellScope was performed by users without prior microscopy experience, a situation intended to mimic clinics and communities that do not have access to conventional LED FM and/or experienced microscopists.

We calculated the sensitivity and specificity of microscopy techniques in reference to mycobacterial culture results (i.e., two cultures per patient), compared them using McNemar's paired test of proportions, and reported sensitivity and specificity differences with exact binomial 95% confidence intervals (CI). We evaluated correlation between techniques and within and between CellScope readers using custom-weighted kappa statistics [30]. We used IUATLD External Quality Assessment guideline definitions for slide reading errors to categorize results that were discordant within and between readers, and to develop the custom kappa weightings. [30]. We performed all data analysis using STATA 10.0 (Statacorp LP, College Station, TX).

### **Ethics statement.**

Institutional review boards at Makerere University, Mulago Hospital, the Uganda National Council for Science and Technology, and the University of California, San Francisco approved the human subjects aspects of the study protocol.

## **Results**

### **Study population.**

Of the 585 total patients in the study, 60 patients (10%) lacked associated culture results and were excluded from the analysis. Table 4.1 shows the characteristics of the remaining

525 patients who provided sputum. Two hundred forty-six (47%) were women. The median age of the patient population was 32 years (interquartile range [IQR] 27-39). Three hundred eighty (72%) were HIV-seropositive, with a median CD4<sup>+</sup> T-lymphocyte count of 55 cells/ $\mu$ l (IQR 19-175). *M. tuberculosis* was cultured from 227 (39%) patients.

### Inter- and intra-reader reliability of CellScope.

Slides from seven of the 60 patients excluded from the analysis were among the 50 semi-quantitatively scored slides, leaving slides from 43 patients for analysis of inter- and intra-reader reliability. Sex and age were similar in this subset compared to the full study population. HIV infection, however, was less prevalent (53% vs. 72%, difference 21%, 95% CI 7–34%), as was culture positivity (23% vs. 41%, difference 18%, 95% CI 2–33%).

We assessed inter-reader reliability using the first semi-quantitative score assigned by each reader. There were 7 minor quantification errors (scanty vs. negative, 2+ or 3+ score assigned) but only one major quantification error (negative vs. 1+, 2+ or 3+ score assigned), leading to moderate overall agreement (weighted kappa 0.65) between readers (Table 4.1).

#### Culture results:

Positive 207

Negative 318

	LED FM		Difference (95% CI)	P value
	CellScope	Conventional		
<b>Sensitivity</b>	63% (130/207)	70% (144/207)	7% (1 to 13%)	0.29
<b>Specificity</b>	85% (271/318)	92% (294/318)	7% (3 to 12%)	0.001

Table 4.1: **Diagnostic accuracy.** Diagnostic accuracy of conventional and CellScope-based LED FM (n = 525).

We assessed intra-reader reliability by comparing the two semi-quantitative scores assigned by each reader. Agreement between the two readings was moderate for Reader 1 (weighted kappa 0.48, Table 4.2, Top), with no major quantification errors and 13 minor quantification errors. Of the 13 minor quantification errors, 12 were discrepancies between scanty and negative scores. However, agreement between the two readings was poor for Reader 2 (weighted kappa 0.11), with 9 major and 6 minor quantification errors (Table 4.2, Bottom).

### Slide examination time with CellScope.

Median slide-examination time for LED FM with CellScope was 4.2 minutes (IQR 2.28–5.97). Median examination time was 1.33 minutes (IQR 0.53–3.23) for positive slides versus

		1 <sup>st</sup> reading of Reader 1 ( <i>n</i> = 43)					
		Neg.	Scanty	1+	2+	3+	Total
2 <sup>nd</sup> reading of Reader 1 ( <i>n</i> = 43)	Neg.	25	5				30
	Scanty	7	1		1		9
	1+			1			1
	2+			1			1
	3+					2	2
	Total	32	6	2	1	2	43

		1 <sup>st</sup> reading of Reader 2 ( <i>n</i> = 43)					
		Neg.	Scanty	1+	2+	3+	Total
2 <sup>nd</sup> reading of Reader 2 ( <i>n</i> = 43)	Neg.	24	1	2	1	2	30
	Scanty	6					6
	1+	1	1	1			3
	2+			1			1
	3+	2			1		3
	Total	34	2	3	2	2	43

- Major error = negative score vs. 1+, 2+ or 3+ score
- Minor error = scanty score vs. negative, 2+ or 3+ score
- No error = identical scores or scanty score vs. 1+ score

† LED FM = light-emitting diode fluorescence microscopy

Table 4.2: **Intra-reader comparisons.** Distribution of semi-quantitative scores for LED FM with CellScope. Top: Reader 1; Bottom: Reader 2.

4.95 minutes (IQR 3.75–6.41) for negative slides ( $p < 0.01$ ).

### Diagnostic accuracy of CellScope and conventional LED FM.

Among the 525 slides, the proportion of positive results was similar with CellScope and conventional LED FM (34% vs. 32%,  $p = 0.38$ ) and there was moderate agreement between the two techniques (unweighted kappa, 0.64). Using culture as a reference standard, the difference in sensitivity between conventional LED FM performed by experienced technicians and CellScope LED FM performed by inexperienced users was within the pre-specified 15% margin of non-inferiority (70% vs. 63%, difference 7%, 95% CI 1–13%) (Table 4.3). Similarly,

the difference in specificity was also within the pre-specified margin of non-inferiority (92% vs. 85%, difference 7%, 95% CI 3–12%). CellScope sensitivity was similar for Reader 1 and Reader 2 (61% vs. 65%, difference 5%, 95% CI -18% to +8%), whereas specificity was significantly higher for Reader 1 (90% vs. 80%, difference 10%, 95% CI 2.2–18%).

		Reader 1 ( $n = 43$ )					
		Neg.	Scanty	1+	2+	3+	Total
Reader 2 ( $n = 43$ )	Neg.	29	5				34
	Scanty	2					2
	1+		1	2			3
	2+	1			1		2
	3+					2	2
	Total	32	6	2	1	2	43

Major error = negative score vs. 1+, 2+ or 3+ score  
 Minor error = scanty score vs. negative, 2+ or 3+ score  
 No error = identical scores or scanty score vs. 1+ score  
<sup>†</sup> LED FM = light-emitting diode fluorescence microscopy

Table 4.3: **Inter-reader comparison.** Distribution of semi-quantitative scores for LED FM with Cellscope.

## Discussion

In this study, we confirmed that inexperienced users could obtain and correctly interpret diagnostic-quality images of stained sputum smears using CellScope, a novel, portable digital imaging device. CellScope readers achieved 63% sensitivity and 85% specificity. Both sensitivity and specificity were within our pre-specified margin of non-inferiority in comparison to conventional LED FM performed by expert technicians. Digital fluorescence microscopy should be further explored as a strategy to extend the reach of TB diagnostic services in high burden countries.

With the advent of low-cost, high-performance optical sensors, a number of novel designs for microscopy-based digital imaging devices have been reported [9, 39, 77, 81]. However, to date, these studies have been largely proof-of-concept in nature. To our knowledge, our study is the first to report the diagnostic accuracy of a portable digital imaging device as compared to conventional LED FM. Our data support the feasibility of smear preparation and imaging by users with no prior microscopy experience. CellScope readers also attained a level of diagnostic accuracy comparable to experienced microscopists performing

conventional LED FM. However, the moderate to poor measures of inter- and intra-reader reliability and sub-optimal sensitivity and specificity suggest that realization of CellScope's potential without adding additional training requirements may depend on further exploiting the device's capacity to transmit and analyze digital images [18].

The results of recent studies provide a roadmap for expanding access to microscopy services through mobile phone-based digital imaging solutions. Mobile phone coverage is extensive in most low-income countries where TB is endemic [4, 93, 115]. Digital images produced by CellScope can be transmitted via the mobile network to distant experts for evaluation, an approach we are currently using in another study with the device and successfully demonstrated in several other recent studies [36, 119, 134]. In addition, significant progress has been made in the development of reliable computer algorithms for the detection of AFB in digital images of sputum smears [18, 34, 123]. Automated image analysis could facilitate on-the-spot diagnosis, improve sensitivity by enabling analysis of a larger number of fields than typically evaluated by a human microscopist, and improve specificity through rigid and reliable criteria for AFB identification. With its use of an external laptop or smart phone for image visualization, CellScope is well positioned to integrate computationally intensive image analysis into its current platform.

Our study also has several potential limitations. First, comparing the performance of diagnostic techniques that involve significantly different technologies poses inherent challenges. Precise scaling of the IUATLD AFB scoring protocol, for example, requires consideration of how the digital imaging system of CellScope influences a variety of factors, from field of view and magnification to optical quality and image resolution. For practical purposes, our modification of the scoring system was based largely on estimated differences with standard LED FM in observed slide area per field of view. Second, the influence of restraining slides prior to reading them with CellScope is unclear. Recent studies have demonstrated that auramine-stained slides fade quickly over time [11, 82], which supports our decision to restrain, but this may have inadvertently increased background noise and reduced the efficiency of CellScope reading [133]. Third, to simulate potential use of CellScope by non-laboratory personnel, we chose two United States-based post-graduate researchers with no prior microscopy experience to re-stain, image, and interpret slides using CellScope. The significant difference in training and experience between the CellScope readers and the technicians who performed conventional LED FM may have complicated our ability to attribute differences in diagnostic performance to technique rather than proficiency.

In summary, our prospective, blinded study demonstrates that the diagnostic accuracy of LED FM with the portable digital imaging device CellScope is comparable to LED FM by conventional methods. The moderate to poor measures of inter- and intra-reader reliability highlight the importance of experience with microscopy and learning challenges associated with any new technology, but may be mitigated by future use of automated AFB identification algorithms. Future studies should evaluate the feasibility of smear preparation, staining and image capture by health workers from low-resource settings, the feasibility of image transmission and analysis by experienced microscopists, and the accuracy of automated image analysis algorithms when combined with portable digital imaging platforms.

Nonetheless, portable and low-cost digital imaging systems such as CellScope represent an important advance in guaranteeing universal access to high quality TB diagnostic testing.

## **Acknowledgements**

The authors thank the staff at the Uganda NTRL for performing conventional LED FM and mycobacterial culture for this study. We also thank the patients, administration, and staff of Mulago National Referral Hospital for making this research possible. The study was supported in part by grants from the National Institutes of Health (K23 AI080147 [JLD] and K23 HL094141 [AC] ), the Vodafone Americas Foundation (DAF), and the Blum Center for Developing Economies (DAF). This work was also supported by the National Center for Research Resources (KL2 RR024130).

## Chapter 5

# Automated Bacillus Identification

### 5.1 Introduction

One of the major limitations on providing diagnostic care in any country is the relative scarcity of trained people to do the diagnosis, and this problem is only exacerbated in low-resource areas. For this reason, despite the successful validation of the diagnostic capabilities of our instrument, finding a way to more fully automate the diagnostic procedure remained a major interest. When another student, Jeannette Chang, expressed interest in working jointly with us and EECS Prof. Malik whose research group specializes in computer vision, we seized the opportunity to pursue an algorithm that would allow reduction in the training necessary for making the delicate diagnostic decision once an image was acquired.

That work leveraged the images taken during the validation testing with the Uganda slide set described in the last chapter; a large number of these, carefully annotated by Clay Reber and Asa Tapley, were used to train the algorithm, which was then tested on a separate set of images as described later in this chapter. The results are extremely encouraging; algorithm performance rivals that inherent in the human-derived training set provided, and the algorithm could be tuned, probably more easily than a human operator, to advantage e.g. diagnostic specificity over sensitivity, especially important in areas where there are few treatment resources and a huge non-TB-positive population.

Because the technical details of the algorithm can be daunting to those not trained in image processing and computer science, a brief overview of the algorithm is in order. The flow of tasks is shown in Figure 5.4.

It is relatively straightforward to select bright objects from an image; NIH ImageJ [95] can do this in nearly real-time even on a low-powered laptop. There are other (even less computationally intensive) approaches, described below, but in principle one feeds the algorithm an image with some bright objects, and these objects are selected by the algorithm for further investigation.

That investigation boils down to so-called “feature extraction”, which can be as simple as making some quantitative judgments on how bright, or large, or oblong the bright object

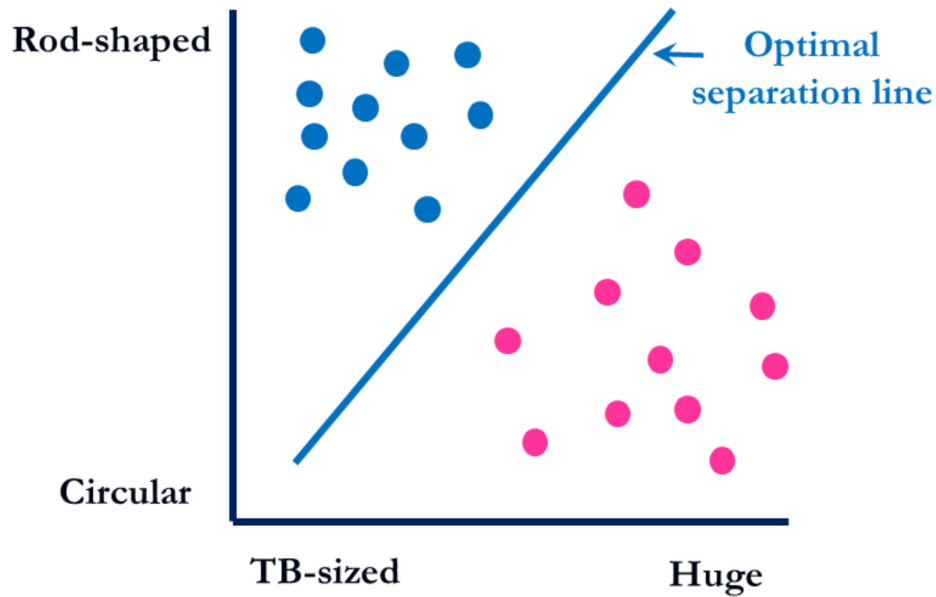


Figure 5.1: **Linear support vector machine operation.** A training set consisting of, e.g., two populations of objects each of which has two features (size and shape) extracted is plotted and a line of best separation chosen. A subsequent unknown object can be assigned a probability of falling into one class of objects or another depending on which side of the separation line it falls on, and how far it falls from the interface. This approach can be extended to  $n$  features per object, with the separation line then becoming an  $n - 1$  dimensional hyperplane.

is. For instance, perhaps there are two classes of objects: crud, of random and often large size and uniform shape, and TB bacilli which are small and rod-shaped. If these are plotted, they might look as in Figure 5.1:

Any new object can then be plotted on the same axes to see which group it might fall into, and a diagnostic decision can be made using this sort of information. The so-called “linear support vector machine” discussed later is simply the approach used to find the best dividing line/plane/hyperplane between the sets of “TB” and “not TB” objects, and we have already demonstrated that a good set of extractable features exists for the objects in TB smear images and that the diagnostic performance of the algorithm can rival that of the human operators.

## 5.2 Automated Tuberculosis Diagnosis Using Fluorescence Images from a Mobile Microscope

As published in:

Medical Image Computing and Computer-Assisted Intervention — MICCAI 2012  
15th International Conference, Nice, France, October 1-5, 2012, Proceedings, Part III  
Series: Lecture Notes in Computer Science, Vol. 7512

Subseries: Image Processing, Computer Vision, Pattern Recognition, and Graphics

Ayache, N.; Delingette, H.; Golland, P.; Mori, K. (Eds.)

2012, XXXII, 645 p. 285 illus., 255 in color., Softcover

ISBN 978-3-642-33453-5

Chapter “Automated Tuberculosis Diagnosis Using Fluorescence Images from a Mobile Microscope” by Chang, J., Arbeláez, P., Switz, N., Reber, C., Tapley, A., Davis, J.L., Cattamanchi, A., Fletcher, D., and Malik, J.

This paper is reproduced here with kind permission of Springer Science+Business Media.

Computer code and image dataset used for the algorithm described in this paper are available online at the following link:

<http://www.eecs.berkeley.edu/Research/Projects/CS/vision/bioimages/>

Additional detail can be found in Jeannette Chang’s Master’s Thesis [17], available at:  
<http://www.eecs.berkeley.edu/Pubs/TechRpts/2012/EECS-2012-100.html>

## 5.3 Automated Tuberculosis Diagnosis Using Fluorescence Images from a Mobile Microscope

Jeannette Chang<sup>1</sup>, Pablo Arbeláez<sup>1</sup>, Neil Switz<sup>2</sup>, Clay Reber<sup>3</sup>, Asa Tapley<sup>3,4</sup>, J. Lucian Davis<sup>4</sup>, Adithya Cattamanchi<sup>4</sup>, Daniel Fletcher<sup>2,3</sup>, Jitendra Malik<sup>1</sup>.

<sup>1</sup>UC Berkeley Department of Electrical Engineering and Computer Sciences; <sup>2</sup>UC Berkeley Biophysics Group; <sup>3</sup>UC Berkeley Department of Bioengineering; <sup>4</sup>UC San Francisco Medical School and San Francisco General Hospital.

### Abstract

In low-resource areas, the most common method of tuberculosis (TB) diagnosis is visual identification of rod-shaped TB bacilli in microscopic images of sputum smears. We present an algorithm for automated TB detection using images from digital microscopes such as CellScope [9], a novel, portable device capable of brightfield and fluorescence microscopy.

Automated processing on such platforms could save lives by bringing healthcare to rural areas with limited access to laboratory-based diagnostics. Our algorithm applies morphological operations and template matching with a Gaussian kernel to identify candidate TB-objects. We characterize these objects using Hu moments, geometric and photometric features, and histograms of oriented gradients and then perform support vector machine classification. We test our algorithm on a large set of CellScope images (594 images corresponding to 290 patients) from sputum smears collected at clinics in Uganda. Our object-level classification performance is highly accurate, with Average Precision of  $89.2\% \pm 2.1\%$ . For slide-level classification, our algorithm performs at the level of human readers, demonstrating the potential for making a significant impact on global healthcare.

## Introduction

Though tuberculosis (TB) receives relatively little attention in high-income countries, it remains the second leading cause of death from infectious disease worldwide (second only to HIV/AIDS) [107]. The majority of TB cases may be treated successfully with the appropriate course of antibiotics, but diagnosis remains a large obstacle to TB eradication. Presently, the most common method of diagnosing patients with TB is visually screening stained smears prepared from sputum. Technicians view the smears with microscopes, looking for rod-shaped objects (sometimes characterized by distinct beading or banding) that may be *Mycobacterium tuberculosis*, the bacteria responsible for TB disease. Apart from the costs of trained technicians, laboratory infrastructure, microscopes and other equipment, this process suffers from low recall rates, inefficiency, and inconsistency due to fatigue and inter-evaluator variability [34]. Hence, with the advent of low-cost digital microscopy, automated TB diagnosis presents a ready opportunity for the application of modern computer vision techniques to a real-world, high-impact problem.

We propose an algorithm for automated TB detection using images from digital microscopes such as CellScope [9] (Figure 5.2), a low-cost and portable alternative to standard laboratory-based microscopes. We present results from a large dataset of sputum smears collected under real-field conditions in Uganda. Our algorithm performs at the level of human readers when classifying slides, which opens exciting opportunities for deployment in large-scale clinical settings. Since our method is capable of processing direct-stained smears, only basic staining supplies are required for slide preparation. Rapid staining kits such as the QBC Diagnostics F.A.S.T. kit are viable in field settings and could thus be used with CellScope in remote areas that lack laboratory infrastructure.

**Previous Work.** The two main methods of screening sputum samples are fluorescence microscopy (FM) and brightfield microscopy, in which the sputum smears are stained with auramine-O and Ziehl-Neelsen respectively (see Figure 5.3). CellScope is capable of both types of microscopy, but we focus on FM here because studies indicate it is more sensitive and significantly faster [14, 68]. Several groups have explored automated TB detection for conventional FM microscopes. Veropoulos *et al.* [124] applied Canny edge detection, filtered objects based on size, and used boundary tracing to identify candidate objects. Fourier descriptors,

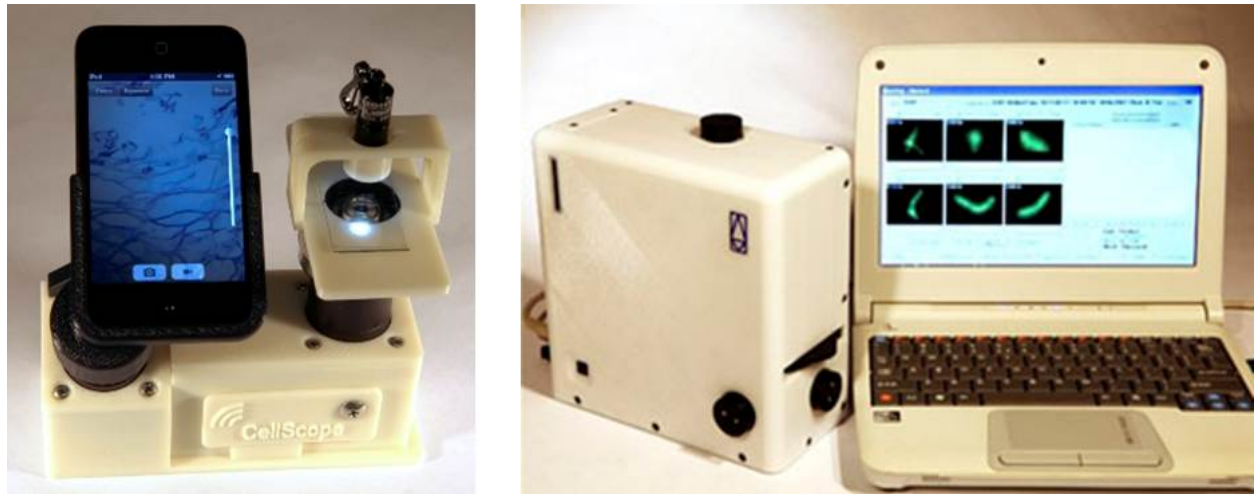


Figure 5.2: **Two versions of CellScope, a novel mobile microscope.** Various uses include point-of-care diagnostics or transmission of images from rural areas to medical experts.

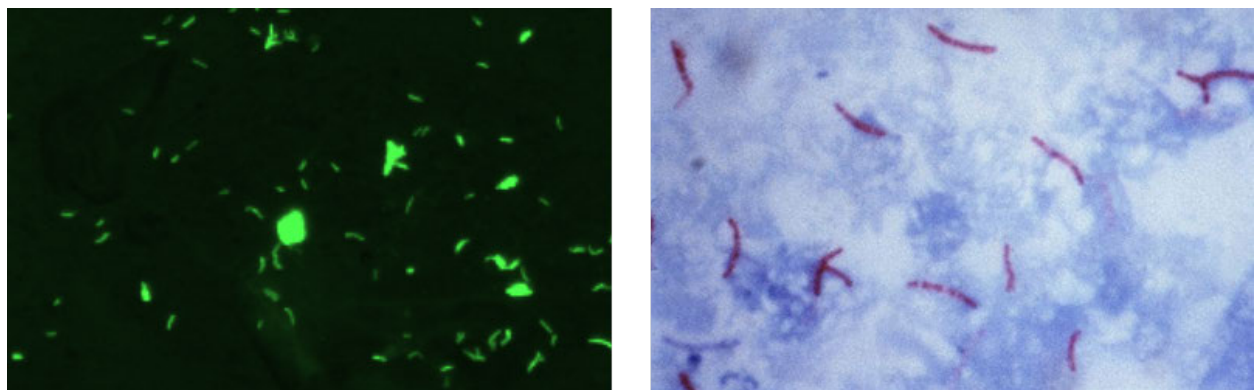


Figure 5.3: **Sample CellScope images.** *Left:* fluorescence. *Right:* brightfield [70].

intensity features, and compactness were then combined with various probabilistic classification methods, and a multilayer neural network achieved the best performance. Forero *et al.* [34] took a generative approach, representing the TB-bacilli class with a Gaussian mixture model (GMM) and using Bayesian classification techniques. Hu moment features were chosen for their invariance to rotation, scaling, and translation. Other groups have proposed algorithms for brightfield microscopy [22, 66], but these algorithms often rely on the distinct color characteristics of Ziehl-Neelsen staining.

Additional TB diagnostic procedures include culture and polymerase chain reaction (PCR)-based methods. Culture results are ideally used to verify smear screenings and are

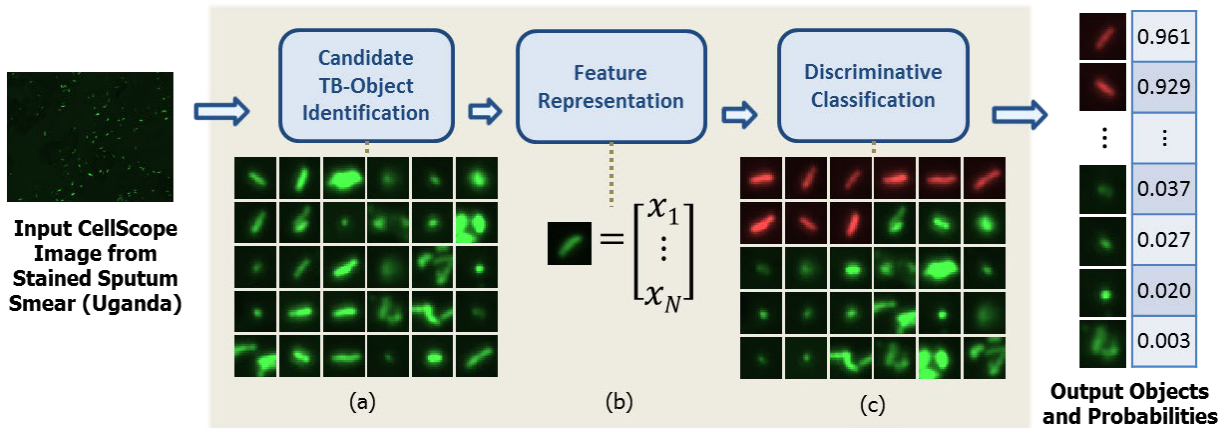


Figure 5.4: **Overview of algorithm.** (a) Array of candidate TB-objects. (b) Each candidate characterized by 102-dimensional feature vector. (c) Candidates sorted by decreasing probability of being a TB-bacillus (row-wise, top to bottom). Sample subset of candidate TB-objects with corresponding probabilities shown at the output. Object-level probabilities subsequently used to determine slide-level diagnosis.

the current gold-standard for diagnosis. However, culture assays are more expensive and technically challenging to perform than smear microscopy and require prolonged incubation: about 2-6 weeks to allow accurate evaluation of bacteria. PCR-based methods such as Cepheid’s GeneXpert assess the presence of TB bacterial DNA and are rapid, more sensitive than smear microscopy, and capable of testing resistance to a common anti-TB antibiotic [5]. However, PCR-based methods continue to lag in sensitivity compared to culture and rely on costly equipment that is poorly suited for low-resource, peripheral healthcare settings [29]. Sputum smear microscopy continues to be by far the most widely used method of TB diagnosis, suggesting that enhancements to microscopy-based screening methods could provide significant benefit to large numbers of TB-burdened communities across the globe.

## Methods and Materials

### Algorithm

We propose a TB detection algorithm for FM with three stages: (1) candidate TB-object identification, (2) feature representation, and (3) discriminative classification. A block diagram of the algorithm is shown in Figure 5.4.

#### Candidate TB-Object Identification.

In the first stage, our goal is to identify any bright object that is potentially a TB-bacillus. We perform a white top-hat transform and template matching with a Gaussian kernel. The

white top-hat transform reduces noise from fluctuations in the background staining, and the template matching picks out areas that resemble bright spots. The result is a binarized image, from which we extract the connected components as candidates. We consider a region of interest or patch from the input image centered around each candidate. The patch-size (24x24 pixels) is chosen based on the known size of the TB-bacilli (typically 2-4 $\mu\text{m}$  in length and 0.5 $\mu\text{m}$  in width) and CellScope’s sample-referenced pixel spacing of 0.25 $\mu\text{m}$ /pixel.

### Feature Representation.

We characterize each candidate TB-object using Hu moments [50]; geometric and photometric features; and histograms of oriented gradients (HOG) [24]. Hu moments, photometric features, and HOG are calculated from the grayscale patch, whereas geometric properties are determined from a binarized version of the image patch. Binarization is achieved using Otsu’s method [87], which minimizes the variance within each of the two resulting pixel classes. Eight Hu moment features provide a succinct object-level description that is invariant to rotation, translation, and scaling (similar to [34]). In addition, we calculate fourteen geometric and photometric descriptors: area, convex area, eccentricity, equivalent diameter, extent, filled area, major/minor axis length, max/min/mean intensity, perimeter, solidity, and Euler number. Finally, we extract HOG features from each 24x24 patch using two scales and 8 orientations, giving eighty HOG feature values. We thus obtain a 102-dimensional feature vector representing the appearance of each candidate TB-object.

### Candidate TB-Object Classification.

We consider three object-level classifiers in our experiments (in order of increasing discriminative power and computational cost): logistic regression, linear support vector machines (SVMs) and intersection kernel (IK) SVMs [16, 21, 31]. Intuitively, SVMs find the hyperplane that maximizes the margin between the TB-positive and TB-negative classes in the feature space. IK SVMs achieve nonlinear decision boundaries via the intersection kernel, defined as  $K(\mathbf{u}, \mathbf{v}) = \sum_i \min(\mathbf{u}_i, \mathbf{v}_i)$ . We normalize the input feature vectors using maximum-minimum standardization and apply logistic regression to the SVM outputs to obtain probabilities [91], which indicate the likelihood of each object being a TB-bacillus.

### Performance Metrics.

We present our experimental results using two sets of performance metrics: Recall/Precision and Sensitivity/Specificity, which are widely used in the computer vision and medical communities respectively. Recall refers to the fraction of true positive objects correctly classified as positives, while Precision refers to the fraction of objects classified as positive that are true positives. Sensitivity is the same as Recall, and Specificity is Recall for the negative class. Recall/Precision are more appropriate for gauging object-level performance in this study because our negative class is much larger than our positive class. At the slide level, however, our data has balanced class sizes and thus both Recall/Precision and Sensitivity/Specificity

are suitable. In this study, we optimize over Average Precision (AP) at the slide level, which places equal weight on Recall and Precision. Often in practice it is more useful to have *either* very high Precision *or* very high Recall (rule-in or rule-out value, respectively) rather than moderately high values for both. In these cases, one may instead optimize over the maximum  $F_\beta$ -measure, defined as  $F_\beta = (1 + \beta^2) \frac{\text{Precision} \cdot \text{Recall}}{(\beta^2 \cdot \text{Precision}) + \text{Recall}}$ , where  $\beta < 1$  gives more weight to Precision than Recall ( $\beta = 1$  gives equal weight).

### Dataset and Ground Truth

Our dataset consists of sputum smear slides collected at clinics in Uganda. Fluorescence images of these smears were taken using CellScope, which has a 0.4NA objective and an 8-bit monochrome CMOS camera. CellScope gives a Rayleigh resolution of  $0.76\mu\text{m}$  and is capable of effective magnifications of 2000-3000x. The CellScope images are 1944x2592 pixels and cover a  $640 \times 490\mu\text{m}$  field of view at the smear-referenced plane. We use 594 CellScope images (296 TB-positive, 298 TB-negative), which correspond to 290 patients (143 TB-positive, 147 TB-negative). We have slide-level human reader and culture classification results for all 290 slides. In addition, a human annotator labeled TB-objects in a subset of the positive images (92 of 296 images), resulting in 1597 positive TB-objects. The human readers in this study received guidance from experts, and their performance has been shown to be statistically comparable to that of trained microscopists. Our dataset and human annotations will be publicly available.

## Experimental Results and Discussion

**Object-Level Evaluation.** For the object-level classification task, we use the subset of TB-positive images for which we have human annotations and all TB-negative images. Applying our object identification procedure, we retain 98.8% of the positive TB-objects in the dataset after the first step. All objects identified in TB-negative images are considered negative objects. This results in 1597 positive and 34948 negative objects, which correspond to 390 images (92 positive and 298 negative).

We generate five random training-test splits with our object-level data: one for model parameter selection and four to assess robustness of results. We train various object-level classifiers, using slide-level performance as the optimizing criterion for parameter selection. We then perform systematic ablation studies as summarized in Figure 5.5. We find that the best performance is achieved when using the whole feature set with an IKSVM: Average Precision of  $89.2\% \pm 2.1\%$  over the four remaining test sets. When relying solely on HOG features, logistic regression and linear SVM methods perform poorly. This is expected because the HOG features are not rotation invariant. [124] also evaluated their algorithm performance at the object-level, but their data and implementation code are not publicly available for direct comparison.

**Slide-Level Evaluation.** We also consider algorithm performance at the slide level, which is more relevant for practical diagnosis. Because slide-level culture results are available,

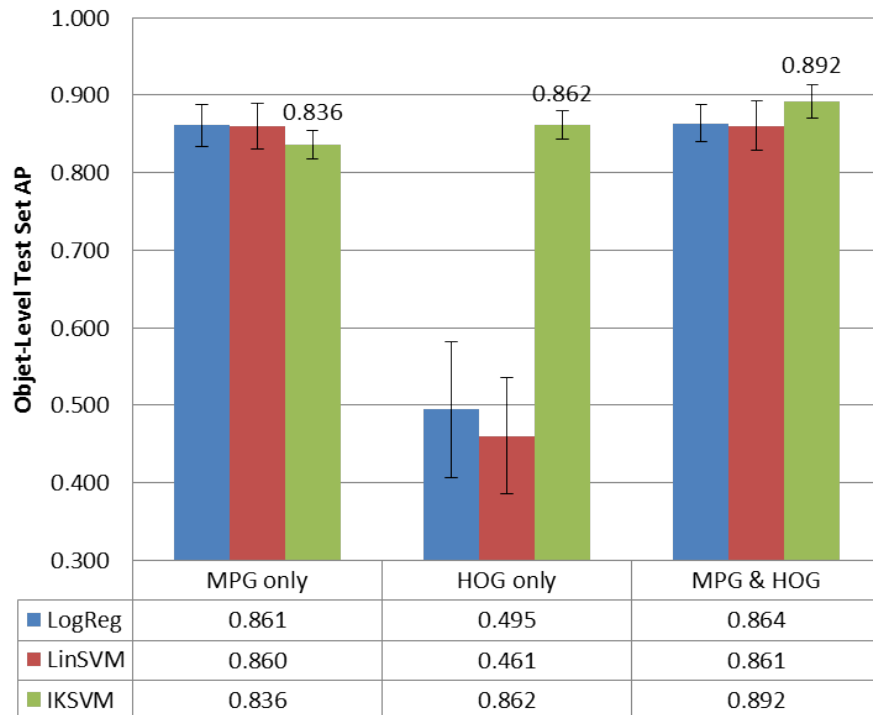


Figure 5.5: **Object-level test set AP across different classifiers** (logistic regression, linear SVM, and IKSVM) and feature subsets. Two categories of features: Hu moments/photometric/geometric (MPG) and histograms of oriented gradients (HOG).

evaluating our algorithm at the slide level frees us from human-labeled ground truth. To determine slide-level decisions from object-level scores, we refer to how experts manually classify slides. For each slide, we gather the output SVM scores of all the objects and average the top  $K$  scores, where  $K = 3$  is chosen via validation experiments. We classify the *slide* as positive if the averaged score falls above a given threshold. By varying this threshold, we obtain a Recall-Precision curve (see plot in Figure 5.6). As shown in Figure 5.6, we consider the three object-level classifiers (logistic regression, linear SVMs, and IKSVMs) in terms of their slide-level performance. We adopt the IKSVM because it achieves slightly better slide-level performance than the other two methods. On the four remaining test sets, the IKSVM achieves slide-level Average Precision of  $92.3\% \pm 0.9\%$  and Average Specificity of  $88.0\% \pm 1.3\%$ .

**Slide-Level Comparison with Baseline and Human Readers.** We compare our algorithm’s slide-level performance to that of human readers and Forero’s GMM-based approach [34]. We train Forero’s algorithm using our data, where color filtering is reduced to intensity filtering because CellScope images are monochromatic. The GMM method achieves Average Precision of  $79.7\% \pm 3.3\%$  and maximum  $F_1$ -measure of  $78.8\% \pm 1.8\%$  (see Figure 5.6).

Method	AP(%)	Max $F_1$ -meas(%)
Humans	-	85.9±1.3
Our SVM	92.3±0.9	84.9±2.4
Baseline	79.7±3.3	78.8±1.8

Classifier	AP(%)	AS(%)
LogReg	91.4±0.5	87.1±1.2
LinSVM	91.1±1.2	86.4±1.3
IKSVM	92.3±0.9	88.0±1.3

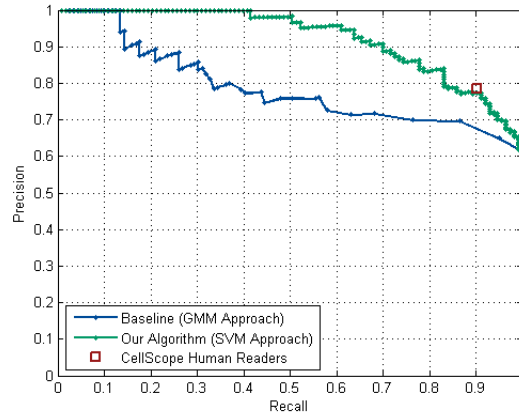


Figure 5.6: **Slide-Level Performance.** *Left top:* Comparison of our IKSVM-based algorithm’s performance to that of humans and the baseline method (GMM approach). Average Precision (AP) and maximum  $F_1$ -measure across four test sets. *Right:* Slide-level Recall-Precision curves across different methods for one test set. *Left bottom:* Our algorithm’s slide-level performance for different object-level classifiers. Average Precision (AP) and Average Specificity (AS), where we average over four test sets.

Human readers also inspected the same CellScope images and classified each slide, resulting in an  $F_1$ -measure of 85.9%±1.3% across the four test sets. The plot in Figure 5.6 shows Recall/Precision curves across different methods for a sample training-test split. For that split, we see that our algorithm’s slide-level performance is comparable to that of human readers and achieves a higher fraction of true positives than the GMM approach for most Recall values.

## Summary and Conclusions

We propose an accurate and robust automated TB detection algorithm for low-cost, portable digital microscopes such as the CellScope. Applying modern computer vision techniques to images from mobile microscopes could save lives in low-resource communities burdened by TB and suffering poor access to high-quality TB diagnostics. The sputum smears used in our study were collected in Uganda and provide a realistic dataset for algorithm training and evaluation. Our algorithm first identifies potential TB-objects and characterizes each candidate object using Hu moments, geometric and photometric features, and histograms of oriented gradients. We then classify each of the candidate objects using an IKSVM, achieving Average Precision of 89.2% ± 2.1% for object classification. At the slide level, our algorithm performs as well as human readers, showing promise for making a tremendous impact on global TB healthcare. We will release our dataset, annotations, and code, which we hope will provide helpful insights for future approaches to quantitative TB diagnosis.

### **Acknowledgment.**

We would like to thank our collaborators at the Mulago Hospital of Kampala, Uganda, who provided the sputum smears used in this study.

# Chapter 6

## Conclusions

I, along with a number of excellent teammates, have taken the concept of mobile-phone based diagnostic microscopy from the original idea through proof-of-concept to a set of 15 fully deployed units as part of a World Health Organization study in Hanoi involving an effort to move tuberculosis diagnosis from the district hospitals out to a peripheral level of the local healthcare system. The devices not only were successful in validation studies, but are now in use in the field. The automatic bacillus-ID algorithm is ready for further integration into the system software and use model, and offers exciting possibilities not only for quality control and assurance, based on its demonstrated ability to match human users' accuracy levels, but also for fine tuning sensitivity and specificity to best match local diagnostic needs.

In any development project of this scope there are many things which could be improved. The remarkable march of consumer technology offerings is already providing remedies for several of these, particularly ones affecting the achievable frame-rate and field of view of the system.

The advent of USB 3.0 camera systems (e.g. the Lumenera Lt425m [78]) has enabled fast (90 fps at full-frame readout), high-pixel-count (4 Mpixel) cameras with 64% QE and larger pixels and FWC. Though this frame-rate will drop for higher-pixel counts (since the USB 3.0 bandwidth is fixed), this allows for video-rate imaging even for a 16 Mpixel sensor, sufficient to allow imaging with the entire field of view of a COTS 20X 0.4NA objective. Hence USB 3.0 will allow for increasing the field of view and thus decreasing the number of images which need be taken, or increasing diagnostic sensitivity, or a combination of both. Furthermore, the pixels in the camera mentioned are much larger ( $5\ \mu\text{m}$  vs.  $2.2\ \mu\text{m}$  for our current camera) and have twice the FWC. If these specifications hold as more such cameras become available both dynamic range and required magnification will increase. The former is universally helpful, while the latter may require longer optical paths (or additional lenses) to achieve the higher required magnification. Unfortunately this seems unlikely to reduce the field curvature issue, since that stems from the ratio of image field position to focal length, both of which will scale identically if one is imaging the entire objective field of view.

The increased QE of the new Lumenera camera is part of a trend; back-thinned CMOS sensors, already present in the iPhone 4s, promise to increase camera QE yet further in the

near-term (year or two) future [104]. Higher QE is uniformly advantageous, allowing either detection of dimmer objects, reduction in required illumination power, or faster frame-rates at the same power. In addition, higher QE, since it results in detection of more of the photons emitted from the sample, allows for more images to be taken before significant photobleaching occurs. An additional benefit of the higher available QEs is that use of color sensors becomes more tractable in a fluorescence system. Such sensors are never optimal for fluorescence — depending on wavelength, anywhere from  $\frac{1}{2}$  to  $\frac{3}{4}$  of the light is lost to the color filters in the sensor color filter array — but if QE hits 90%, then imaging the green emission of Auramine O would still take place at an effective QE of 45%, exactly what our current sensor provides. The advantage would then be in the ability to use the same camera for both fluorescence and color imaging, e.g. in brightfield, allowing for other diagnostic tests using the same hardware platform.

Efforts to increase image acquisition frame-rate will also benefit from advances in LED output powers. Already over the course of this project these have roughly doubled which the emitting die size has shrunk by more than a factor of two, effectively increasing output brightness, the critical parameter as discussed in Chapter 3 by more than 4X, and increasing potential imaging speed by the same factor. Any further advances will be similarly beneficial. The limit to this process may come in the form of the 445nm laser diodes are now becoming commercially available at low cost ( $\lesssim$  \$150 for a 1 W laser). The inherently tiny Etendue provided by a laser beam allows enormous latitude in coupling it to a sample. While care must be taken over safety, sample photobleaching, and interference effects which can create inhomogeneities in the illumination system, it is distinctly possible that by using such lasers electrical power requirements will drop at the same time useable illumination intensity rises by an order of magnitude, reducing required exposure times and enabling full use of the fast camera frame-rates enabled by USB 3.0. Use of a laser offers other advantages as well: lasers typically also have much narrower emission bandwidths than LEDs or other sources; this may obviate the need for the excitation filter in the optical system, reducing cost and optical complexity. Separately, laser illumination is quite advantageous for darkfield microscopy, discussed below.

From the design perspective, there are several places it would be interesting to pursue cost reductions, starting with filter placement in the illumination path, though use of a laser would immediately obviate the need for that filter. In addition, one of the more expensive mechanical components is the mechanism for moving the slide tray. My initial prototype used a “finger-stage” which provided a guide edge and flat surface along which the user pushed the slide with their finger. This is mechanically robust, having no moving parts, and as low-cost as can be had; however, technicians used to benchtop microscope-style fine translation stages did not like it. A hybrid approach, where some actuator (perhaps spring loaded to reduce mechanical backlash) is provided to allow fine translation of a slide along a single axis might go far to providing a path to easier manufacture and lower eventual cost.

Turning to mechanical design, we placed heavy emphasis on eventual low-cost manufacturability and on robustness in the face of transport and vibration, e.g. in a backpack or during transport in a jeep on a rutted road. As a result there are no adjustable elements

in the optical train, which makes the system perhaps overly vulnerable to uncontrollable manufacturing tolerances, which can show up as, e.g., focus gradients across an image. Fluorescence imaging of flat samples is especially sensitive to this, since the depth of field at 0.4NA is only  $\sim 3 \mu\text{m}$ , and the Strehl ratio (and thus object brightness) drops rapidly as focus changes. In a subsequent redesign, adding some small number of adjustments for use during assembly, designed so they can be adequately locked down once set, would significantly ease manufacturing.

Darkfield illumination would be nice to implement as well, and should not be complicated (especially if laser illumination is used). Darkfield is especially useful in diagnosing cholera, and so would spread the possible uses of the device at very little increase in the cost of manufacture.

Lastly, it would be nice to move the overall system back toward something that can be built around a phone, though the prototyping issues surrounding that, among other things, remain very real. As phones grow ever more powerful (and with ever larger screens), there may be a nice convergence where one of the limiting factors — sufficient screen real estate to focus adequately — ceases to matter as much and an additional size reduction from the laptop becomes possible.

I would like to end this thesis with thanks to all of the teammates and collaborators (in several countries) whose efforts have led to such progress in deploying a new diagnostic.



Figure 6.1: **Deployed systems.** Commune Health Post workers in training during deployment of 15 units as part of a WHO study in Hanoi. Courtesy Dr. Lina Nilsson.

# Bibliography

- [1] M. Akhtar, International Union against Tuberculosis, and Lung Disease. *Technical guide: sputum examination for tuberculosis by direct microscopy in low income countries, 5th ed.* 2000.
- [2] R. M. Anthony et al. “Light emitting diodes for auramine O fluorescence microscopic screening of Mycobacterium tuberculosis”. In: *Int J Tuberc Lung Dis* 10 (2006), pp. 1060–2.
- [3] Yanina Balabanova et al. “An integrated approach to rapid diagnosis of tuberculosis and multidrug resistance using liquid culture and molecular methods in Russia.” In: *PLoS ONE* 4.9 (2009), e7129. DOI: 10.1371/journal.pone.0007129.
- [4] Livia Bellina and Eduardo Missoni. “Mobile cell-phones (M-phones) in telemicroscopy: increasing connectivity of isolated laboratories”. In: *Diagnostic Pathology* 4.19 (2009), p. 19. DOI: 10.1186/1746-1596-4-19.
- [5] Catharina C. Boehme et al. “Rapid Molecular Detection of Tuberculosis and Rifampin Resistance”. In: *New England Journal of Medicine* 363.11 (2010), pp. 1005–1015. DOI: 10.1056/NEJMoa0907847.
- [6] Glenn Boreman. *Modulation Transfer Function in Optical and ElectroOptical Systems*. Vol. TT52. SPIE Tutorial Texts in Optical Engineering, 2001.
- [7] Max Born and Emil Wolf. *Principles of Optics: Electromagnetic Theory of Propagation, Interference and Diffraction of Light*. Cambridge University Press, 1999.
- [8] R. P. Braun et al. “Telemedical wound care using a new generation of mobile telephones: a feasibility study”. In: *Arch Dermatol* 141 (2005), pp. 254–8. DOI: 10.1001/archderm.141.2.254.
- [9] David N Breslauer et al. “Mobile Phone Based Clinical Microscopy for Global Health Applications”. In: *PLoS ONE* 4.7 (2009), e6320. DOI: 10.1371/journal.pone.0006320.g003.
- [10] Peter Burns. “Slanted-Edge MTF for Digital Camera and Scanner Analysis”. In: *Proc. IS&T 2000 PICS Conference* (2000), pp. 135–138.
- [11] T Buzingo et al. “Systematic restaining of sputum smears for quality control is useful in Burundi”. In: *International Journal of Tuberculosis and Lung Disease* 7 (2003), pp. 439–444.

- [12] “Calculating Output Power”. In: *Oriel Newport Corp.* (2012). URL: [www.newport.com/Calculating-Output-Power/383396/1033/content.aspx](http://www.newport.com/Calculating-Output-Power/383396/1033/content.aspx).
- [13] A. Cattamanchi et al. “Integrated Strategies to Optimize Sputum Smear Microscopy: A Prospective Observational Study”. In: *Am. J. Respir. Crit. Care Med.* 183.4 (2011), pp. 547–551. DOI: 10.1164/rccm.201008-12070C.
- [14] A Cattamanchi et al. “Sensitivity and specificity of fluorescence microscopy for diagnosing pulmonary tuberculosis in a high HIV prevalence setting.” In: *Int. J. Tuberc. Lung Dis.* 13.9 (2009), pp. 1130–1136.
- [15] “Cepheid pricing of GeneXpert”. In: *Treatment Action Group* (2011), pp. 1–2. URL: [www.treatmentactiongroup.org/sites/tagone.drupalgardens.com/files/cepheidletter.pdf](http://www.treatmentactiongroup.org/sites/tagone.drupalgardens.com/files/cepheidletter.pdf).
- [16] Chih-Chung Chang and Chih-Jen Lin. “LIBSVM: A Library for Support Vector Machines”. In: *ACM Transactions on Intelligent Systems and Technology* 2.3 (2011), pp. 27.1–27.27. DOI: 10.1145/1961189.1961199.
- [17] Jeannette Chang. *Automated Tuberculosis Diagnosis Using Fluorescence Images from a Mobile Microscope*. Master’s Thesis, University of California Berkeley, 2012, pp. 1–54. URL: <http://www.eecs.berkeley.edu/Pubs/TechRpts/2012/EECS-2012-100.html>.
- [18] Jeannette Chang et al. “Automated Tuberculosis Diagnosis Using Fluorescence Images from a Mobile Microscope”. In: *MICCAI 2012, Part III. LNCS, vol. 7512. Springer-Verlag, Berlin Heidelberg* (2012), pp. 345–352.
- [19] David H. Chui and Martin H. Steinberg. *Laboratory Diagnosis of Hemoglobinopathies and Thalassemias, in Hematology: Basic Principles and Practice, 4th ed.* Churchill Livingstone, 2004.
- [20] Lynn E Connolly, Paul H Edelstein, and Lalita Ramakrishnan. “Why is long-term therapy required to cure tuberculosis?” In: *PLoS Med.* 4.3 (2007), e120. DOI: 10.1371/journal.pmed.0040120.
- [21] C Cortes and V Vapnik. “Support-vector networks”. In: *Machine Learning* 20.3 (1995), pp. 273–297.
- [22] Marly G Costa et al. “Automatic identification of mycobacterium tuberculosis with conventional light microscopy”. In: *Proceedings : Annual International Conference of the IEEE Engineering in Medicine and Biology Society* 2008 (2008), pp. 382–5. DOI: 10.1109/IEMBS.2008.4649170.
- [23] Luis Eduardo Cuevas et al. “LED fluorescence microscopy for the diagnosis of pulmonary tuberculosis: a multi-country cross-sectional evaluation.” In: *PLoS Med.* 8.7 (2011), e1001057. DOI: 10.1371/journal.pmed.1001057.

- [24] N Dalal and B Triggs. “Histograms of oriented gradients for human detection”. In: *Proceedings 2005 IEEE Computer Society Conference on Computer Vision and Pattern Recognition* (2005), pp. 886–893.
- [25] J Lucian Davis et al. “Clinical and Radiographic Factors Do Not Accurately Diagnose Smear-Negative Tuberculosis in HIV-infected Inpatients in Uganda: A Cross-Sectional Study”. In: *PLoS ONE* 5.3 (2010), e9859. DOI: 10.1371/journal.pone.0009859.t003.
- [26] *Digital Imaging and Communications in Medicine (DICOM) Standard*. National Electrical Manufacturers Association (NEMA), 2008.
- [27] David W Dowdy et al. “The potential impact of enhanced diagnostic techniques for tuberculosis driven by HIV: a mathematical model.” In: *AIDS* 20.5 (2006), pp. 751–62. DOI: 10.1097/01.aids.0000216376.07185.cc.
- [28] Jean Dubos and Rene Dubos. *The White Plague: Tuberculosis, Man and Society*. Rutgers University Press, 1987.
- [29] Carlton A Evans. “GeneXpert—a game-changer for tuberculosis control?” In: *PLoS Med.* 8.7 (2011), e1001064. DOI: 10.1371/journal.pmed.1001064.
- [30] “External Quality Assessment for AFB Smear Microscopy”. In: *World Health Organization, Laboratories Association of Public Health, Centers for Disease Control and Prevention, IUATLD, KNCV Tuberculosis Foundation, Research Institute of Tuberculosis; World Health Organization* (2002), pp. 1–104.
- [31] RE Fan et al. “LIBLINEAR: A library for large linear classification”. In: *The Journal of Machine Learning Research* 9 (2008), pp. 1871–1874.
- [32] “FIND negotiated prices for Xpert MTB/RIF and country list”. In: *FIND Diagnostics* (2012), pp. 1–6. URL: [http://www.finddiagnostics.org/about/what\\_we\\_do/successes/find-negotiated-prices/xpert\\_mtb\\_rif.html](http://www.finddiagnostics.org/about/what_we_do/successes/find-negotiated-prices/xpert_mtb_rif.html).
- [33] Ray Fontaine. “Recent Innovations in CMOS Image Sensors”. In: *Advanced Semiconductor Manufacturing Conference (ASMC), 2011 22nd Annual IEEE/SEMI* (2011), pp. 1–5.
- [34] M G Forero, G Christobal, and M Desco. “Automatic identification of Mycobacterium tuberculosis by Gaussian mixture models”. In: *J Microsc* 223.Pt 2 (2006), pp. 120–132. DOI: 10.1111/j.1365-2818.2006.01610.x.
- [35] J. Frean. “Microscopic images transmitted by mobile cameraphone”. In: *Trans R Soc Trop Med Hyg* 101 (2007), p. 1053. DOI: 10.1016/j.trstmh.2007.06.008.
- [36] John Frean. “Microscopic images transmitted by mobile cameraphone”. In: *Trans. R. Soc. Trop. Med. Hyg.* 101.10 (2007), p. 1053. DOI: 10.1016/j.trstmh.2007.06.008.
- [37] Naoki Fukutake. *US 5,889,618 Object lens for microscope*. 1999.

- [38] Haileyesus Getahun et al. “Diagnosis of smear-negative pulmonary tuberculosis in people with HIV infection or AIDS in resource-constrained settings: informing urgent policy changes”. In: *The Lancet* 369.9578 (2007), pp. 2042–2049. DOI: 10.1016/S0140-6736(07)60284-0.
- [39] Kunal K Ghosh et al. “Miniaturized integration of a fluorescence microscope”. In: *Nat Meth* 8.10 (2011), pp. 871–878. DOI: 10.1038/nmeth.1694.
- [40] Mary J Gilchrist et al. “The Potential Role Of Concentrated Animal Feeding Operations In Infectious Disease Epidemics And Antibiotic Resistance”. In: *Environmental health perspectives* 115.2 (2007), pp. 313–6. DOI: 10.1289/ehp.8837.
- [41] Joseph Goodman. *Introduction to Fourier Optics*. Roberts and Company Publishers, 2004.
- [42] Y. Granot, A. Ivorra, and B. Rubinsky. “A new concept for medical imaging centered on cellular phone technology”. In: *PLoS ONE* 3 (2008), e2075. DOI: 10.1371/journal.pone.0002075.
- [43] T. Hanscheid et al. “Fluorescence microscopy for tuberculosis diagnosis”. In: *Lancet Infect Dis* 7 (2007), pp. 236–7. DOI: 10.1016/S1473-3099(07)70058-0.
- [44] Thomas Hänscheid. “The future looks bright: low-cost fluorescent microscopes for detection of Mycobacterium tuberculosis and Coccidia”. In: *Trans. R. Soc. Trop. Med. Hyg.* 102.6 (2008), pp. 520–521. DOI: 10.1016/j.trstmh.2008.02.020.
- [45] Thomas Hänscheid et al. “Fluorescence microscopy for tuberculosis diagnosis.” In: *Lancet Infect Dis* 7.4 (2007), pp. 236–237. DOI: 10.1016/S1473-3099(07)70058-0.
- [46] C. Hendry et al. “Evaluation of a rapid, fluorescent stain for the detection of mycobacteria in clinical specimens”. In: *J Clin Microbiol* 47 (2009), pp. 1206–1208. DOI: 10.1128/JCM.02097-08.
- [47] C Hendry et al. “Evaluation of a Rapid Fluorescent Staining Method for Detection of Mycobacteria in Clinical Specimens”. In: *J. Clin. Microbiol.* 47.4 (2009), pp. 1206–1208. DOI: 10.1128/JCM.02097-08.
- [48] Philip C. Hobbs. *Building Electro-Optical Systems*. Wiley-Interscience Series in Pure and Applied Optics, 2000.
- [49] Gerald C. Holst and Terrence S. Lomheim. *CMOS/CCD Sensors and Camera Systems*. SPIE Press, 2011. URL: 978-0819486530.
- [50] Ming-Kuei Hu. “Visual pattern recognition by moment invariants”. In: *IRE Transactions on Information Theory* 8.2 (1962), pp. 179–187. URL: [http://ieeexplore.ieee.org/xpls/abs\\_all.jsp?arnumber=1057692](http://ieeexplore.ieee.org/xpls/abs_all.jsp?arnumber=1057692).
- [51] N. V. Hung et al. “Fluorescence microscopy for tuberculosis diagnosis”. In: *Lancet Infect Dis* 7 (2007), 238–9; author reply 239–40. DOI: 10.1016/S1473-3099(07)70059-2.

- [52] *Informal consultation on quality control of malaria microscopy*. World Health Organization, 2006.
- [53] Shinya Inoue. *Video Microscopy*. Plenum, 1986.
- [54] *International Standards for Tuberculosis Care (ISTC)*. Tuberculosis Coalition for Technical Assistance. 2009. URL: [www.istcweb.org/documents/ISTC\\_Report\\_2ndEd\\_Nov2009.pdf](http://www.istcweb.org/documents/ISTC_Report_2ndEd_Nov2009.pdf).
- [55] J Janesick et al. *Fundamental performance differences between CMOS and CCD imagers: Part II (Invited Paper)[6690-02]*. Vol. Vol. 6690. Proc. of SPIE, 2007, p. 669003.
- [56] J Janesick et al. “Fundamental performance differences between CMOS and CCD imagers: part III”. In: *Proc. of SPIE* 7439 (2009), pp. 743907–1–26.
- [57] J. R. Janesick. *Photon transfer*. Vol. PM170. SPIE-International Society for Optical Engineering, 2007.
- [58] James R. Janesick, James T. Andrews, and Tom Elliott. “Fundamental Performance Differences Between CMOS and CCD Imagers; Part I”. In: *Proc. SPIE* Vol. 6276 (2008), pp. 62760M–1–19.
- [59] D. Jones et al. “McArthur revisited: fluorescence microscopes for field diagnostics”. In: *Trends Parasitol* 23 (2007), pp. 468–9. DOI: 10.1016/j.pt.2007.08.003.
- [60] Donald G. Mcneil Jr. “Five Years In, Gauging Impact Of Gates Grants”. In: *The New York Times* (2010), p. 1.
- [61] “Judge Orders FDA to Restrict Antibiotic Use in Animals”. In: *Food Product Design* (2012), pp. 1–1. URL: <http://www.foodproductdesign.com/news/2012/03/judge-orders-fda-to-restrict-antibiotic-use-in-an.aspx>.
- [62] K M Kam et al. “Bulk acid-fast staining of sputum smears: time to end a taboo”. In: *The International Journal of Tuberculosis and Lung Disease* 13.9 (2009), pp. 1119–23.
- [63] Emmett Keeler et al. “Reducing the global burden of tuberculosis: the contribution of improved diagnostics.” In: *Nature* 444 Suppl 1 (2006), pp. 49–57. DOI: 10.1038/nature05446.
- [64] Emmett Keeler et al. “Reducing the global burden of tuberculosis: the contribution of improved diagnostics.” In: *Nature* 444 Suppl 1 (2006), pp. 49–57. DOI: 10.1038/nature05446.
- [65] P Kent and G Kubica. *Public health mycobacteriology - a guide for the level III laboratory*. U.S. Centers for Disease Control and Prevention, 1985.
- [66] Rethabile Khutlang et al. “Classification of Mycobacterium tuberculosis in images of ZN-stained sputum smears.” In: *IEEE Trans Inf Technol Biomed* 14.4 (2010), pp. 949–957. DOI: 10.1109/TITB.2009.2028339.
- [67] Jean-Marie Kindermans. “Changing national malaria treatment protocols in Africa: What is the cost and who will pay?” In: *Médecins Sans Frontières* (2002), pp. 1–7.

- [68] L E Kivihya-Ndugga et al. “A comprehensive comparison of Ziehl-Neelsen and fluorescence microscopy for the diagnosis of tuberculosis in a resource-poor urban setting.” In: *Int. J. Tuberc. Lung Dis.* 7.12 (2003), pp. 1163–1171.
- [69] Paul de Kruif. *Microbe Hunters*. Mariner Books, 1926.
- [70] G. P. Kubica. *Mycobacterium Tuberculosis Bacteria Using Acid-Fast Ziehl-Neelsen Stain; magnified 1000x*. 1979.
- [71] SD Lawn and AI Zumla. “Tuberculosis”. In: *Lancet* 378 (2011), pp. 57–72.
- [72] Marc Levoy. “Experimental Platforms for Computational Photography”. In: *IEEE Computer Graphics and Applications* 30.5 (2010), pp. 81–87.
- [73] *Light collection and system throughput*. 2004. URL: [www.newport.com/Tutorial-Light-Collection-and-Systems-Throughput/381845/1033/content.aspx](http://www.newport.com/Tutorial-Light-Collection-and-Systems-Throughput/381845/1033/content.aspx).
- [74] Philips Lumileds. “Luxeon Rebel Technical Datasheet DS56”. In: *Philips LumiLEDs* (2009), pp. 1–34.
- [75] *Luxeon III Star Technical Datasheet DS46*. 2006.
- [76] *Malaria light microscopy: creating a culture of quality*. WHO SEARO/WPRO Workshop on Quality Assurance for Malaria Microscopy, 2005.
- [77] Brian McCall et al. “Toward a low-cost compact array microscopy platform for detection of tuberculosis”. In: *Tuberculosis* 91 (2011), S54–S60. DOI: 10.1016/j.tube.2011.10.011.
- [78] T McDonald. *Lumenera Lt425 USB 3.0 Preliminary Datasheet*. 2012.
- [79] Jerome Mertz. *Introduction to Optical Microscopy*. Roberts and Company Publishers, 2009.
- [80] G B Migliori et al. “First tuberculosis cases in Italy resistant to all tested drugs”. In: *Euro surveillance : European communicable disease bulletin* 12.5 (2007), E070517.1.
- [81] Andrew R Miller et al. “Portable, Battery-Operated, Low-Cost, Bright Field and Fluorescence Microscope”. In: *PLoS ONE* 5.8 (2010), e11890. DOI: 10.1371/journal.pone.0011890.g002.
- [82] Jessica Minion et al. “Fading of auramine-stained mycobacterial smears and implications for external quality assurance.” In: *J. Clin. Microbiol.* 49.5 (2011), pp. 2024–6. DOI: 10.1128/JCM.00507-11.
- [83] C Mitja et al. *Slanted Edge MTF*. URL: <http://rsbweb.nih.gov/ij/plugins/se-mtf/index.html>.
- [84] C. K. Murray et al. “The remote diagnosis of malaria using telemedicine or e-mailed images”. In: *Military Medicine* 171 (2006), pp. 1167–1171.
- [85] *Natural Resources Defense Council v. US Food and Drug Administration. Memorandum Opinion and Order; US Mag. Judge T.H. Katz*. 2012.

- [86] World Health Organization. *Anti-tuberculosis drug resistance in the world, fourth global report: the WHO/IUATLD Global Project on Anti-Tuberculosis Drug Resistance Surveillance*. 2008.
- [87] Nobuyuki Otsu. “A threshold selection method from gray-level histograms”. In: *IEEE Transactions on Systems, Man, and Cybernetics* SMC-9.1 (1979), pp. 62–66.
- [88] Yasemin Ozluk et al. “Superiority of virtual microscopy versus light microscopy in transplantation pathology”. In: *Clinical Transplantation* 26.2 (2012), pp. 336–344. DOI: 10.1111/j.1399-0012.2011.01506.x.
- [89] *Package Insert: Rapid Modified Auramine O Fluorescent Stain Set*. Scientific Device Laboratories I, 2007.
- [90] Cathy A Petti et al. “Laboratory medicine in Africa: a barrier to effective health care”. In: *Clin. Infect. Dis.* 42.3 (2006), pp. 377–82. DOI: 10.1086/499363.
- [91] John C Platt. “Probabilistic outputs for support vector machines and comparisons to regularized likelihood methods”. In: *Advances in large margin classifiers* (1999), pp. 61–74.
- [92] Scott Prahl. “Auramine O”. In: *Oregon Medical Laser Center* (2012). URL: <http://omlc.ogi.edu/spectra/PhotochemCAD/html/027.html>.
- [93] M Priftis et al. *The Little Data Book on Information and Communication Technology 2012*. World Bank, 2012.
- [94] *Quality assurance of sputum microscopy in DOTS programmes*. World Health Organization-Regional Office for the Western Pacific, 2003.
- [95] W. S. Rasband. *ImageJ (1997-2008)*. U. S. National Institutes of Health. URL: <http://rsb.info.nih.gov/ij/>.
- [96] SE Reichenbach, SK Park, and R Narayanswamy. “Characterizing digital image acquisition devices”. In: *OPT ENG* 30.2 (1991), pp. 170–177.
- [97] Rafael Rocha et al. “Digital slides: Present status of a tool for consultation, teaching, and quality control in pathology”. In: *Pathology - Research and Practice* 205.11 (2009), pp. 735–741. DOI: 10.1016/j.prp.2009.05.004.
- [98] K Rowland. “Totally drug-resistant TB emerges in India”. In: *Nature: News & Comment* (2012), pp. 1–8. DOI: doi:10.1038/nature.2012.9797.
- [99] *Running out of breath? TB care in the 21st century*. Médecins Sans Frontières Campaign for Access to Essential Medicines, 2004.
- [100] Frank Ryan. *The Forgotten Plague: How the Battle Against Tuberculosis Was Won - And Lost*. Back Bay Books, 1994.
- [101] M Schlacks et al. *Evaluation of four commercially available auramine O stain sets*. 2006.

- [102] K Singh et al. “Molar extinction coefficients in aqueous solutions of some amino acids”. In: *J. Radioanalytical and Nuclear Chemistry* 253.3 (2002), pp. 369–373.
- [103] Warren J. Smith. *Modern Optical Engineering*. McGraw-Hill, 2000.
- [104] *Sony commercializes world’s first 16.41 Megapixel ”Exmor R” back-illuminated CMOS image sensors for mobile phones*. 2010. URL: [www.sony.net/SonyInfo/News/Press/201010/10-137E/index.html](http://www.sony.net/SonyInfo/News/Press/201010/10-137E/index.html).
- [105] Kenneth Spring and Michael Davidson. “The Microscope Optical Train”. In: *Nikon MicroscopyU* (2012). URL: [www.microscopyu.com/articles/optics/components.html](http://www.microscopyu.com/articles/optics/components.html).
- [106] *Sputum Examination for Tuberculosis by Direct Microscopy in Low Income Countries, Fifth edition*. International Union Against Tuberculosis and Lung Disease (IUATLD), 2000.
- [107] WHO Staff. *Global Tuberculosis Control: WHO Report 2011*. World Health Organization, 2011.
- [108] K. R. Steingart et al. “Commercial serological antibody detection tests for the diagnosis of pulmonary tuberculosis: a systematic review”. In: *PLoS Med* 4 (2007), e202. DOI: 10.1371/journal.pmed.0040202.
- [109] Karen R Steingart et al. “Fluorescence versus conventional sputum smear microscopy for tuberculosis: a systematic review.” In: *Lancet Infectious Disease* 6.9 (2006), pp. 570–581. DOI: 10.1016/S1473-3099(06)70578-3.
- [110] A. Streetly et al. “Implementation of the newborn screening programme for sickle cell disease in England: results for 2003-2005”. In: *J Med Screen* 15 (2008), pp. 9–13. DOI: 10.1258/jms.2008.007063.
- [111] S. Tachakra et al. “Mobile e-health: the unwired evolution of telemedicine”. In: *Telemed J E Health* 9 (2003), pp. 247–57. DOI: 10.1089/153056203322502632.
- [112] Asa Tapley. *Mobile Digital Imaging-based Microscopy for Tuberculosis Diagnosis*. Master’s Thesis, University of California Berkeley, 2012, pp. 1–59.
- [113] *TB diagnostics and laboratory strengthening - WHO policy*. 2012. URL: [www.who.int/tb/laboratory/policy\\_liquid\\_medium\\_for\\_culture\\_dst/en/index.html](http://www.who.int/tb/laboratory/policy_liquid_medium_for_culture_dst/en/index.html).
- [114] Micron Technology. *MT9P031 5Mp 1/2.5-inch CMOS digital image sensor*. 2011. URL: [www.aptna.com/products/image\\_sensors/mt9p031i12stm/](http://www.aptna.com/products/image_sensors/mt9p031i12stm/).
- [115] S Teltscher et al. *Measuring the Information Society: The ICT Development Index*. Telecommunication Development Bureau, International Telecommunications Union, 2009.
- [116] *The Global Plan to Stop TB 2011-2015*. 2011, pp. 1–101.
- [117] J Truant, W Brett, and W Thomas. “Fluorescence microscopy of tubercle bacilli stained with auramine and rhodamine.” In: *Henry Ford Hospital Medical Bulletin* 10 (1962), pp. 287–296.

- [118] L. Tshilolo et al. “Neonatal screening and clinical care programmes for sickle cell disorders in sub-Saharan Africa: Lessons from pilot studies”. In: *Public Health* 122 (2008), pp. 933–41. DOI: 10.1016/j.puhe.2007.12.005.
- [119] Coosje J. Tuijn et al. “Data and Image Transfer Using Mobile Phones to Strengthen Microscopy-Based Diagnostic Services in Low and Middle Income Country Laboratories”. In: *PLoS ONE* 6.12 (2011), e28348 1–8. DOI: 10.1371/journal.pone.0028348.
- [120] Z F Udwadia et al. “Totally Drug-Resistant Tuberculosis in India”. In: *Clinical Infectious Diseases* 54.4 (2012), pp. 579–581. DOI: 10.1093/cid/cir889.
- [121] “US Preventive Services Task Force. Screening for sickle cell disease in newborns: recommendation statement”. In: *Am Fam Physician* 77 (2008), pp. 1300–2.
- [122] Pieter W Uys, Robin M Warren, and Paul D van Helden. “A threshold value for the time delay to TB diagnosis.” In: *PLoS ONE* 2.8 (2007), e757. DOI: 10.1371/journal.pone.0000757.
- [123] K Veropoulos et al. “Automated identification of tubercle bacilli in sputum - a preliminary investigation”. In: *Analytical and quantitative cytology and histology* 21.4 (1999), pp. 277–282.
- [124] Konstantinos Veropoulos. “Machine learning approaches to medical decision making”. In: *Thesis, University of Bristol* (2001), pp. 1–292.
- [125] J M Wales et al. “Tuberculosis in a primary school: the Uppingham outbreak.” In: *Br Med J (Clin Res Ed)* 291.6501 (1985), pp. 1039–40.
- [126] Welford. *Useful Optics*. University of Chicago Press, 1991, pp. 1–14.
- [127] Karin Weyer and World Health Organisation Staff. *Laboratory Services in Tuberculosis Control, Part II: Microscopy*. World Health Organization, 1999, p. 95.
- [128] “WHO Drug Information”. In: *World Health Organization* 17.3 (2003), pp. 143–277. URL: <http://apps.who.int/medicinedocs/documents/s14243e/s14243e.pdf>.
- [129] G. Williams et al. *Best practice for the care of patients with tuberculosis*. A guide for low-income countries. Paris: International Union Against Tuberculosis and Lung Disease, 2007, pp. 1–85.
- [130] W Witte. “Selective pressure by antibiotic use in livestock”. In: *International journal of antimicrobial agents* 16 Suppl 1 (2000), S19–24.
- [131] B. Woodward, R. S. Istepanian, and C. I. Richards. “Design of a telemedicine system using a mobile telephone”. In: *IEEE Transactions on Information Technology in Biomedicine* 5 (2001), pp. 13–15.
- [132] P. Yager, G. J. Domingo, and J. Gerdes. “Point-of-care diagnostics for global health”. In: *Annu Rev Biomed Eng* 10 (2008), pp. 107–44. DOI: 10.1146/annurev.bioeng.10.061807.160524.

- [133] C. W. Yip et al. “Random blinded rechecking of sputum acid-fast bacilli smear using fluorescence microscopy: 8 years’ experience”. In: *The International Journal of Tuberculosis and Lung Disease* 16.3 (2012), pp. 398–401. DOI: 10.5588/ijtld.11.0330.
- [134] M. Zimic et al. “Can the power of mobile phones be used to improve tuberculosis diagnosis in developing countries?” In: *Trans R Soc Trop Med Hyg* 103 (2009), pp. 638–40. DOI: 10.1016/j.trstmh.2008.10.015.